Aldehyde deformylation by nonheme metal complexes – a mechanistic study

A thesis submitted in partial fulfillment of the requirements for the degree of

DOCTOR OF PHILOSOPHY

Submitted by

SAYANTA SEKHAR NAG
(Roll No 146122024)

Department of Chemistry
Indian Institute of Technology Guwahati
Guwahati – 781039
Assam, India

05 July 2021

Dedication

To

My uncle Mr. Ashish Bhunia

For his constant support throughout my life.

Statement

I, with this, declare that the matter discussed in this dissertation is the result of research carried out by me in the Department of Chemistry, Indian Institute of Technology Guwahati, India, under the guidance of Prof. Chivukula V. Sastri. In keeping with the general practice of reporting scientific observations, due acknowledgments have been given wherever the work described is based on other investigators' findings.

Sayanta Sekhar Nag

Certificate

It is to certify that Sayanta Sekhar Nag has been working under my supervision since July 2014 as a regular registered Ph.D. student. The work described in the thesis entitled "**Aldehyde deformylation by nonheme metal complexes – a mechanistic study**" has been carried out under my supervision and has not been submitted elsewhere for the Ph.D. (Science) degree. I certify that he has fulfilled all the requirements according to the rule of the institute.

05 July 2021

Prof. Chivukula V. Sastri
Thesis Supervisor
Department of Chemistry
Indian Institute of Technology Guwahati
Guwahati – 781039
Assam, India

Acknowledgment

I would like to express my gratitude and appreciation to all those who helped me during my journey as a Ph.D. student at the Indian Institue of Technology Guwahati. I want to express my deepest gratitude to Prof. Chivukula V. Sastri for his excellent guidance, patience, relevant suggestions and for providing me with a unique atmosphere for my research work.

I am also very thankful to my doctoral committee members, Prof. Ashish K Gupta, Prof. M. Qureshi, and Prof. Gopal Das, for giving their valuable time to evaluate my work and providing me helpful suggestions. I want to thank the head of the department and other faculty members for carrying out this research. I want to thank all the chemistry department staff without whose support it would be difficult to carry out the research work.

I am thankful to the department of chemistry and central instrument facility IIT Guwahati for providing me various instruments necessary for the characterization and detection of multiple compounds for my research. I would like to thank Mr. K. K. Singh for his help in understanding the LC-MS instrument.

I would like to extend my heartiest gratitude to my undergraduate professor Dr. Anup Pathak and Dr. Banshidhar Mondal, who has sparked my interest in chemistry. Their guidance, support, and love blessed me with an insight into the chemical world.

This work would not be possible without the student's contribution who worked before me in the CVS group. So I would like to thank Dr. Prasenjit Barman for his contribution

to the research related to the deformylaion reaction. The ethos of the CVS research group is we work together. All the research work I have done wouldn't be possible without the constant support, criticism, and the entertaining environment created by my labmates; in earlier days by Gourab, and later Umesh and Jagnyesh joined to that list. I feel fortunate to have such an encouraging work environment.

I am thankful to all of my friends who have helped me during my days at IIT Guwahati. It is tough to single out individuals, and I hate to do it because I am fortunate to know such beautiful persons and privileged to call them my friends. Though few stand apart from the crowd, I would like to thank Rana and Subhankar for being there for me whenever I needed them. I would also like to thank my friend Baishaki, Sampa, Ankhi, Pallabita, Soumi, and Sujit. I will always cherish the moments I have shared with you, and it is these memories, which give me strength in difficult times.

I am grateful to the Ministry of Human Resource Development for granting me financial support with the scholarship.

Finally, I wish to thank my Mother, my family and my wife Swagata for being there for me whenever I needed mental support. Without their constant encouragement, I won't be able to complete my thesis.

Table of Contents

List of Figures

List of Schemes

Abbreviation

AD	Aldehyde decarbonylase
cADO	Cyanobacterial aldehyde deformylating oxygenase
NADPH	Nicotinamide adenine dinucleotide phosphate
$NADP^+$	Nicotinamide adenine dinucleotide
2-PPA	2-Phenylpropionaldehyde
CCA	Cyclohexanecarbaxaldehyde
THF	Tetrahydrofuran
KIE	Kinetic isotope effect
DFT	Density functional theory
EPR	Electron Paramagnetic Resonance
ESI-MS	Electrospray ionization mass spectrometry
NMR	Nuclear magnetic resonance
LMCT	Ligand to metal charge transfer

TMC	Tetramethylcyclam
N4Py	N-bis(2-pyridylmethyl)-N-bis(2-pyridyl)methylamine
BL1	Dimethyl 3,7-dimethyl-9-oxo-2,4-di(pyridin-2-yl)-3,7-diazabicyclo[3.3.1]nonane-1,5-dicarboxylate
BL2	Dimethyl 3,7-dibenzyl-9-oxo-2,4-di(pyridin-2-yl)-3,7-diazabicyclo[3.3.1]nonane-1,5-dicarboxylate
BL3	Dimethyl 9-oxo-3,7-bis(pyridin-2-ylmethyl)-3,7-diazabicyclo[3.3.1]nonane-1,5-dicarboxylate
OAT	Oxygen atom transfer
Otf	Triflate
PPh_3	Triphenylphosphine

Synopsis

Introduction

The emission of greenhouse gases and particulate matter has profoundly impacted climate change by unsettling the earth's radiation balance. The earth's atmosphere is in an equilibrium condition; the incoming flux of solar energy is balanced with the outgoing flux of energy as long-wave radiation. Over time, several radiatively active gases increase concentrations because of various human activities, disrupting the delicate balance of existing energy transfer equilibria in our atmosphere. Human activity has also increased aerosol particles' levels either by direct emission or by emitting the gases responsible. This increasing aerosol particle concentration also disturbs the radiation equilibria and affects human health by creating various lung diseases. Among all the greenhouse gases, CO_2 is the main contributor to anthropogenic radiative forcing.

Fossil fuel burning is the primary reason for increasing the concentration of greenhouse gases and aerosol particles. Apart from their help in changing the earth's climate, there are other problems in using fossil feedstocks in large amounts, and the primary one is that its resources are finite. Scientists are trying to find suitable alternatives for the last few decades, and they came up with various technologies like solar power, nuclear power, biofuels, etc., as alternative energy sources. Many of the so-called first-world countries are reducing their fossil fuel consumption substantially. In economically progressing countries like India, there is a lot of complexity depending on those alternatives. The crude oil refinery industry also produced a wide variety of

commodity products for everyday uses. Biomass has particular interest among scientists because it can reduce the dependencies on fossil feedstock by generating both fuels and the necessary chemicals in a net carbon neutral biosynthetic pathway.

Biosynthesis of long-chain alkanes or, for that matter, hydrocarbons, in general, can be tremendously helpful in solving the issue. In a petroleum refinery industry, apart from the extensive use of fuels, hydrocarbons are the primary raw material for producing various commodity products. The prospect of using the biosynthesis of hydrocarbon as an alternative to the crude oil refinery systems accelerated the fascination towards mechanistic enzymology.

Hydrocarbon biosynthesis in nature has evolved several times. There are three types of mechanisms for forming unfunctionalized alkanes utilizing fatty aldehydes as a precursor. The aldehyde is an intermediate product in the process of long-chain-alkane formation from fatty acids. Aldehyde decarbonylases (AD) are the only known class of enzymes to convert aldehyde to alkanes with one less carbon via carbon-carbon bond cleavage. There are three different kinds of aldehyde decarbonylases known for three different types of organisms, plants, insects, and cyanobacteria. All of them are also structurally different from each other. The most recently discovered pathway for alkane biosynthesis is the cyanobacterial pathway. Cyanobacterial aldehyde decarbonylase is also known as cyanobacterial aldehyde deformylating oxygenase (cADO). The end product for cADO is entirely different than the other two mechanisms. In this case, the aldehyde carbon transformed into formate instead of any gaseous

product, unlike the other two mechanisms. The reactivity of cADO was tested with some model aldehyde substrates having relatively smaller carbon chains than natural fatty aldehydes like nonanal and decanal. In these cases, alcohols and aldehydes with one less carbon atom formed as a product and alkane and formate.

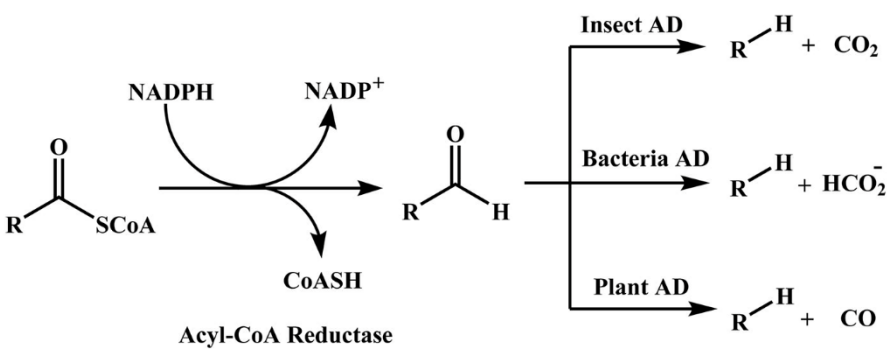

Figure I. Various steps for the biosynthesis of alkanes in nature.

The kinetics study of natural enzymes has always been a complicated task for many reasons likes solubility, purity, etc. There might be some other cofactors in vivo, which helps the catalyst perform their activity, which is difficult to replicate in vitro. Among the three different natural decarbonylases, only for the cADO successful kinetics study has been achieved. Kinetic analysis of cADO reveals that the reaction is extremely slow. Various research groups have tried to use different reaction conditions, but the reactivity does not improve much. This slow reactivity of the natural enzymes in vitro makes them challenging to use as a catalyst for biofuel biosynthesis on an industrial scale.

As a result, scientists have put more emphasis on synthetically generated systems.

The synthetic model compounds have been used in mimicking different types of biological reactions and study their mechanism. They are relatively easy to synthesize and purify to be used successfully on an industrial-scale provided other parameters are in favor. There are two major genres of synthetic model systems – heme and nonheme enzymes, and both classes of compounds are used extensively to understand the details of deformylation reaction. The dinuclear and mononuclear types of synthetic models containing iron are generated to mimic natural enzymes' reactivity and adequately understand their mechanism. Among all the various kinds of artificial models available, the mononuclear nonheme transition metal-peroxo systems got more attention recently, as handling them takes relatively less effort. Though the natural AD enzymes contain mainly Fe at the active site, synthetic models have been generated using different transition metals. A detailed understanding of the deformylation mechanism by nonheme mononuclear systems would help produce a more efficient catalyst for hydrocarbon biosynthesis.

Many of the studies used 2-PPA and CCA as model substrates for aldehyde deformylation. Those studies unveiled the carton from many unknown facts about the reaction, e.g., the fate of the peroxo oxygen, effect of the electron-donating group at the axial position of the peroxo group, the effect of solvent on the product formation, the effect of structural conformation of the substrate on the reactivity. However, most of those studies convey that the reaction

occurs via nucleophilic attack of the peroxo oxygen at the aldehyde's carbonyl carbon. In our earlier studies, the unveiling of a new mechanical way for the deformylation of 2-PPA by an Mn peroxo system provides an alternate viewpoint in contrast to the popular opinions. We now know that the H atom's availability at the α-position of the aldehyde group controls aldehyde's reactivity. So aldehydes with readily available H atom converts to an alkane faster, provided other conditions remain the same. This information will help enormously in selecting suitable substrates for a well-planned outcome.

Apart from the substrate, many different factors influence a reaction, and catalyst is crucial among them. The ligand architecture has a stimulating effect on the reactivity of the metal-oxygen intermediates. Our detailed literature study found that there is little or sometimes no information available on the isotope substitution experiments in the previous reports. Our vision is to study the mechanism of the reactions earlier declared as nucleophilic reactions in the light of the newly developed mechanistic pathway with or without modification in ligand architecture.

This thesis tried to determine the deformylation reaction of 2-PPA by Cu(II)-alkylperoxo intermediates and how ligand architecture affects that. It also revisits CCA's deformylation mechanism by Fe(III) and Mn(III)-peroxo intermediates.

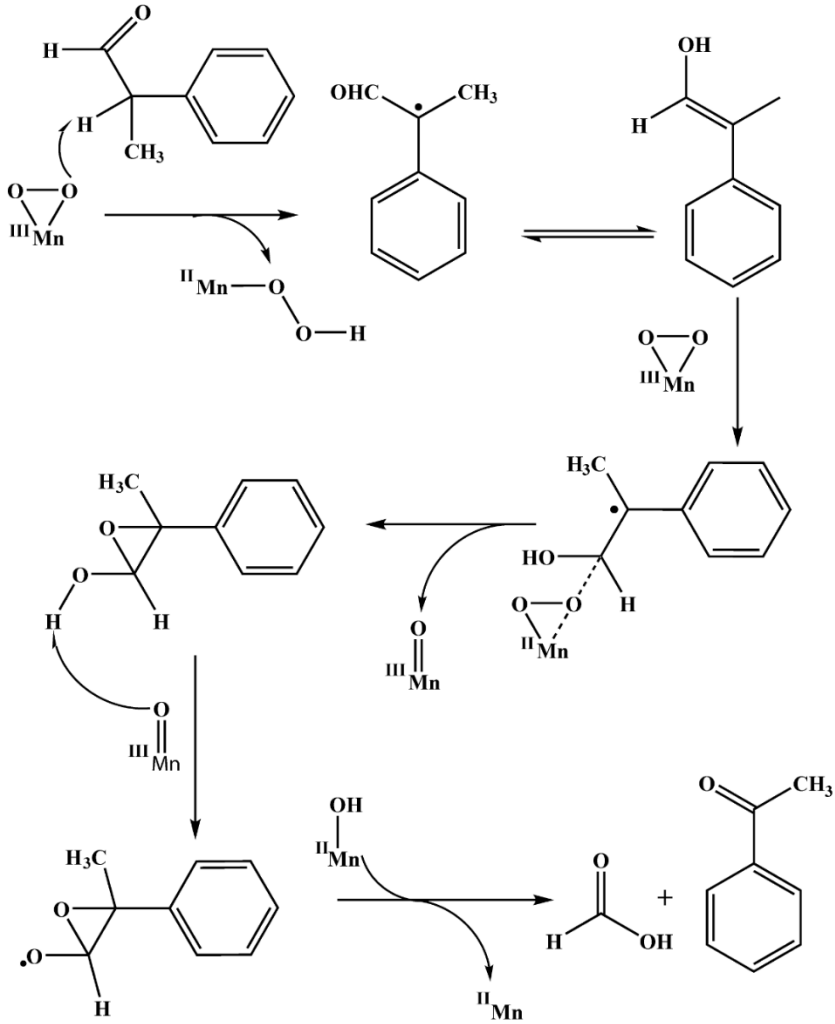

Figure II. H-atom abstraction mechanism by Mn(III)-peroxo intermediate.

Influence of induced steric on the deformylation of aldehyde by Cu(II)-alkylperoxo intermediates

This chapter has studied the mechanism of aldehyde deformylation by the Cu(II)-alkylperoxo species and the effect of ligand architecture on its reactivity. A few reports are available on aldehydes' deformylation by Cu(II)-alkylperoxo intermediate, but detail mechanistic studies have not been performed in most cases. In most cases, Cu(II)-alkylperoxo complexes behave as an electrophilic species, though believed to act differently in aldehyde deformylation. Recent developments in the deformylation reaction mechanism of Mn(III)-peroxo systems suggest an initial H-atom abstraction mechanism. That study inspires us to perform isotope labeling experiments for the deformylation by Cu(II)-alkylperoxo species to get more details about the mechanism. We have synthesized two isomeric bispidine based Cu(II)-alkylperoxo complex Alkylperoxo complexes $[Cu(BL1)(OO^tBu)]^+$ (**1**) and $[Cu(BL2)(OO^tBu)]^+$ (**2**) were generated from their Cu(II) precursors, using ^{t}BuOOH and Et_3N in CH_3CN at 298 K.

We have used 2-Phenylpropionaldehyde (2-PPA) as a model substrate for the aldehyde deformylation reaction. The pseudo-first-order rate constant (k_{obs}) for the reaction increases proportionally with an increase of the 2-PPA concentration, allowing us to measure the second-order rate constant(k_2) for deformylation with **1** and **2** as oxidants of 0.027 M^{-1} s^{-1} and 0.0093 M^{-1} s^{-1}, respectively. To investigate the mechanism, we have performed isotope labeling experiments. We have measured kinetic isotope effect (KIE) of 12 and

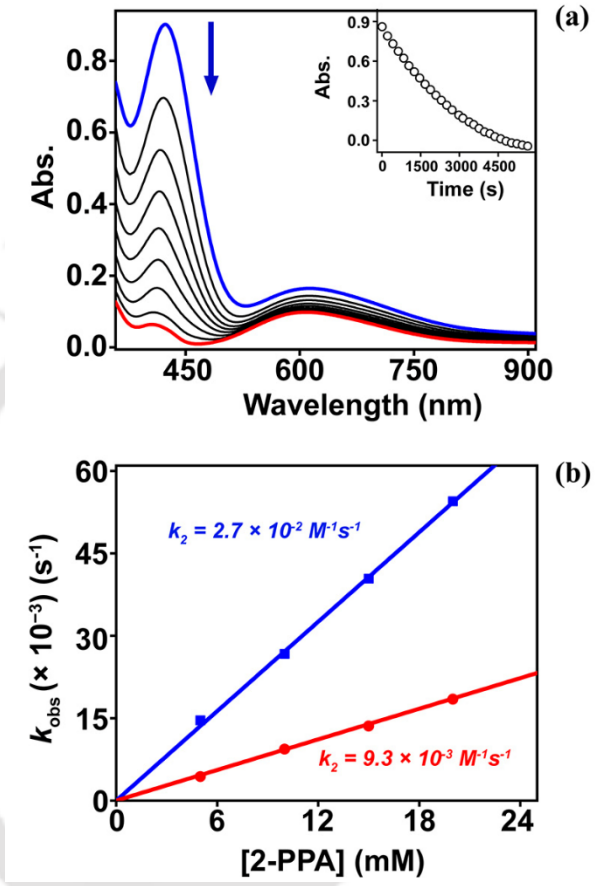

Figure III. *[a] Decay of 1 upon addition of 2-PPA (15 mM) in CH_3CN at 298 K [inset shows the time trace for the peak at 423 nm]. [b] Plot of k_{obs} against the concentration of 2-PPA and the second-order rate constant for the reaction of 2-PPA with **1**(■) and **2**(●).*

8 for the H-atom at α-position of aldehyde, for **1** and **2**, respectively. Therefore, our kinetics studies establish that complexes **1** and **2** react with 2-PPA via an electrophilic hydrogen atom abstraction. We have also found that complex **1** reacts at a higher rate than **2**. To investigate the ligand architecture effect, we

have decided to check the reactivity with other known electrophilic reactions like oxygen atom transfer to a heteroatom. In the oxidation of PPh_3, complex **2** reacts at a faster rate than **1**. The experimental results suggest a switchover of the reactivity order for the OAT.

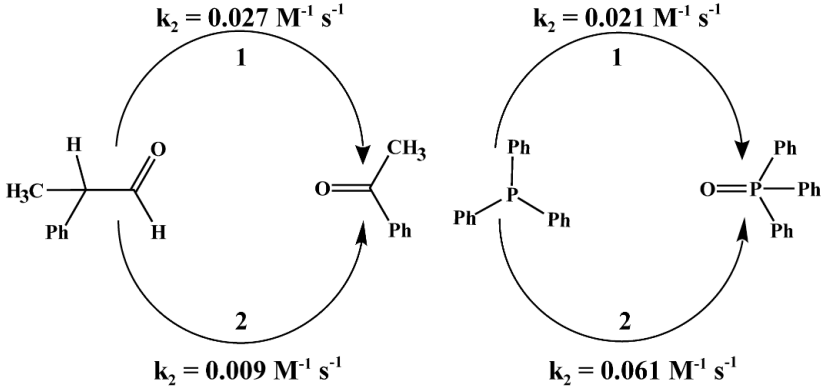

Scheme I. Reactivity of Cu(II)-alkylperoxo in different reactions

We have demonstrated the synthesis, characterization, and reactivity of two bispidine Cu(II)-alkylperoxo complexes. In contrast to the earlier report of nucleophilic carbonyl attack by Cu-alkylperoxo species, the species mentioned above exhibit C-H abstraction at the α-position of the aldehyde group. The high KIE value is imperative for rate-determining C-H bond cleavage. It has also been observed that these two complexes show an inverse trend in reactivity for two different types of reactions. The introduction of two benzyl groups instead of methyl groups at the N3 and N7 positions increases the steric bulk around the metal center, accelerating atom transfer to heteroatoms. Simultaneously, the

same phenomenon decreases reaction rates for aldehyde deformylation reactions by reducing the substrate approach feasibility.

Substrate triggered conversion of η^2 to η^1- Fe(III)-peroxo for the deformylation of CCA

The aldehyde deformylation by Fe(III)-peroxo has been considered to proceed via a nucleophilic attack by the peroxo group at the aldehyde's carbonyl carbon. Earlier developments, in our lab, on the deformylation by Mn(III)-peroxo and Cu(II)-alkylperoxo species suggest otherwise; and we have been very curious to know the details for Fe(III)-peroxo system. For this purpose, we use 2-PPA, CCA, and their isotopic derivative as the model substrate in this work. The H-atom abstraction mechanism has been postulated based on isotope labeling experiments. We have searched the literature at our best but unable to find out any isotope labeling experiment at α-position for the deformylation Fe(III)-peroxo intermediates. To find out more insight on the deformylation mechanism for Fe(III)-peroxo species, we have used α-D-2-PPA and α-D-CCA as mechanical probes.

We have used Fe(III)-peroxo species supported by N4Py and TMC ligand framework. These two peroxo species are well characterized previously by various research groups. The intermediates $[Fe(N4Py)(O_2)]^+$ (**3**) and $[Fe(TMC)(O_2)]^+$ (**4**) were generated according to the reported procedure in the literature.

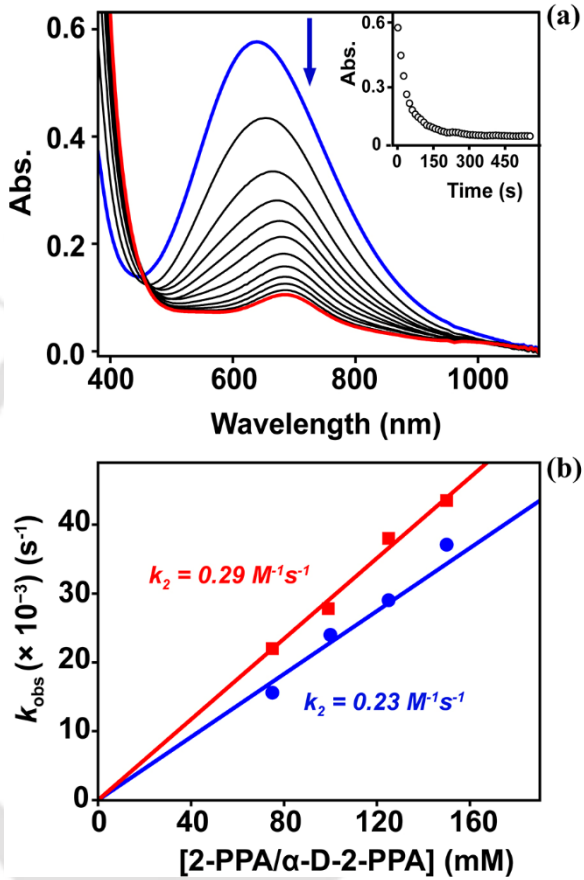

*Figure IV. (a) UV-Vis absorption spectra for the reaction of **3** with 2-PPA. (b) The plot of pseudo-first-order rate constant (k_{obs}) against the different concentrations of 2-PPA (■) and α-D-2-PPA (●).*

To understand the effect of the isotopic substitution, we have performed the reaction with 2-PPA and α-D-2-PPA. After the addition of the substrate, the intermediate started to decay immediately. We have not observed any kinetic isotope effect (KIE) for the H atom at α-position. So, the initial H atom

abstraction from the α-position of 2-PPA is not an option for Fe(III)-peroxo intermediates.

When we add CCA to 1 mM TFE solution of intermediate **3** at 243 K, the electronic absorption spectra of **3** give an immediate blue shift of 140 nm. Surprisingly, the solution changes from blue to purple, with a new absorption maximum at 540 nm. The purple solution's electronic absorption feature suggests a similarity with the previously reported Fe(III)-hydroperoxo species. To check whether this Fe(III)-OOH formation results from the H-atom abstraction from the α-positions, we have added α-D-CCA to **3**. The intermediate shows a similar spectral pattern to that of reaction with CCA with a color change from blue to purple. Since we do not found any Change in reactivity pattern for α-D-CCA and CCA, the question remains about the location of hydrogen plucked by the intermediate, which causes interconversion of peroxo to hydroperoxo intermediate. The peroxo intermediate leaves no other possibility but the aldehyde's H atom abstraction. To check our hypothesis, when we add 1-D-CCA to a solution of **3**, the absorption band decayed immediately with no blue shift, and the intermediate reverted to the iron(III) complex with an isosbestic point at 450 nm.

This result supported the role of the aldehyde H atom in the reaction of Fe-N4Py-peroxo with CCA and suggested that the Fe-N4Py-peroxo complex is not following a nucleophilic carbonyl attack mechanism for deformylation of CCA.

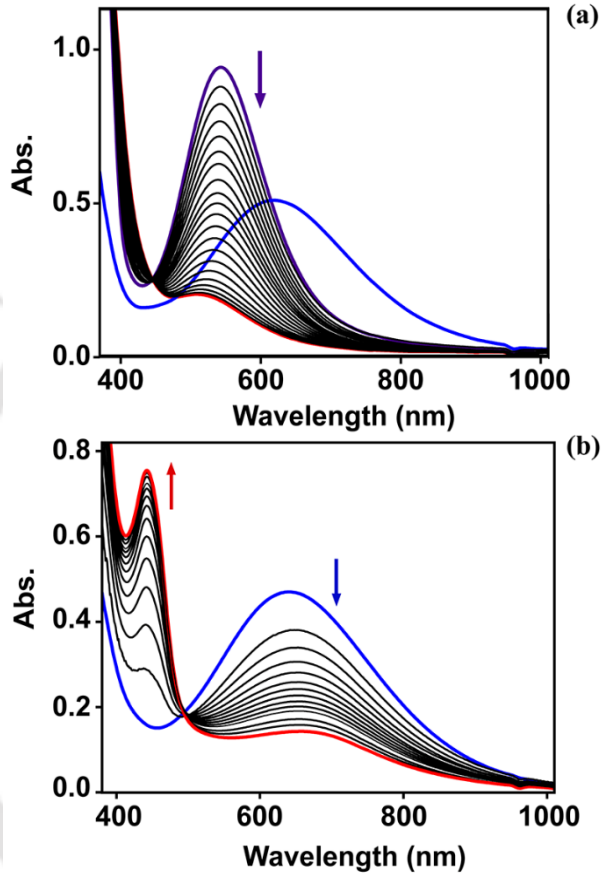

Figure V. UV-Vis spectra for the reaction of 3 with CCA (a) and 1-D-CCA (b).

The deformylation of CCA has been studied previously with intermediate **4**, and there was no report for such an anomaly. So, we have decided to explore the effect of isotopic substitution with **4**. The addition of CCA to **4** at 258 K started the absorption band's decay without any shift. When we investigated the

reaction of **4** with α-D-CCA, there was no significant change in rate. To further confirm the aldehyde's H atom abstraction, we have decided to check the reactivity of **4** with 1-D-CCA. The absence of KIE for both 2-PPA and CCA suggests α-H atom abstraction is not possible for **3** and **4**. The addition of 1-D-CCA makes the intermediate decays with its natural decay rate, making it impractical to get a second-order rate. However, a slower reactivity compared to CCA suggests the aldehyde's H atom involvement. Further study is required to get an accurate mechanistic pathway for CCA deformylation by **4**.

This chapter discussed the mechanism for the aldehyde deformylation reaction of Fe(III)-peroxo species with different commonly used model substrates. The careful research and analysis of the data prove that the most feasible mechanism is a nucleophilic carbonyl attack for the Fe(III)-peroxo species. Still, the reaction pathway can differ from substrate to substrate, and it proceeds via an initial H atom abstraction, especially for CCA.

Establishment of a pristine mechanistic pathway for aldehyde deformylation by Mn(III)-peroxo intermediates

This chapter dealt with the synthesis and characterization of a new tetradentate N-donor-based Mn(II)-complex. The aldehyde deformylation reaction was studied using CCA and their derivatives as the model substrates. The reactivity of Fe(III)-peroxo system with 2-PPA and CCA has proved the possibility of a different kind of mechanism for the later one. This experimental result inspires us to investigate the facts further to convey a more accurate reaction mechanism

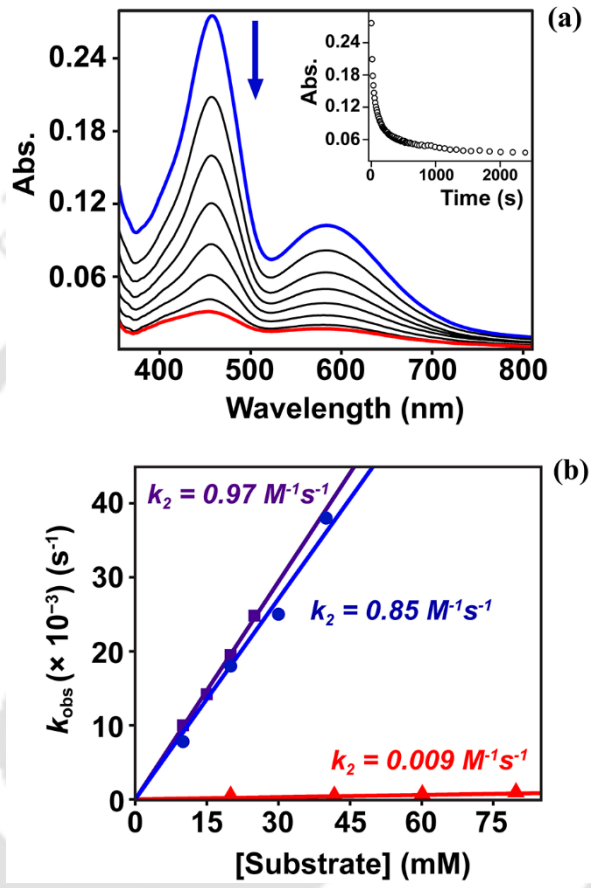

Figure VI. (a) UV-Vis spectra for the decay of 5 upon adding 20 mM CCA to an acetonitrile solution (1 mM) of ***5*** *at 278K. (b) A plot of pseudo-first-order rate constant (k_{obs}) against the different concentrations of CCA (●), 2-Me-CCA (■), and 1-d-CCA (▲).*

for aldehyde deformylation by Mn(III)-peroxo species. Upon adding CCA to $[Mn(L1)(O_2)]^+$ (**5**), the intermediate decayed down immediately. The reaction rate increases proportionally with increasing substrate concentration giving a

second-order rate constant of 0.85 $M^{-1}s^{-1}$. To establish whether an initial H-atom abstraction from the α-position of aldehyde has also happened here or not, we use 2-Me-CCA as a substrate. The addition of 2-Me-CCA to an acetonitrile solution of **5** at 278 K causes a fast decay of the absorption band, giving a second-order rate constant of 0.97 $M^{-1}s^{-1}$. The higher reactivity with 2-Me-CCA comes as a surprise considering the previously reported α-H abstraction by Mn(III)-peroxo intermediate. To find out the exact mechanism, we add 1-D-CCA as a mechanical probe. The reaction rate slows down upon the addition of 1-D-CCA to **5** at 278 K, giving a KIE of 90. This result suggests the involvement of aldehyde C-H bond dissociation in the rate-determining step (RDS).

To get more confirmation of the reactivity pattern, we tried to investigate CCA's deformylation with Mn(III)-peroxo intermediate bearing TMC ligand, $[Mn(TMC)(O)_2]^+$ (**6**). It is well characterized and has a similar electronic absorption pattern to that of the bispidine based system. Upon adding CCA to an acetonitrile solution, the intermediate, we have observed a second-order rate constant of 0.31 $M^{-1}s^{-1}$, similar to the previously reported value.

To check the mechanism more accurately, we use 1-D-CCA as a substrate. Upon the deuterated substrate's addition, the reaction becomes very slow, and the intermediate decays with its natural decay rate. This result suggests that TMC based Mn(III)-peroxo also reacts with CCA via aldehyde H-atom abstraction.

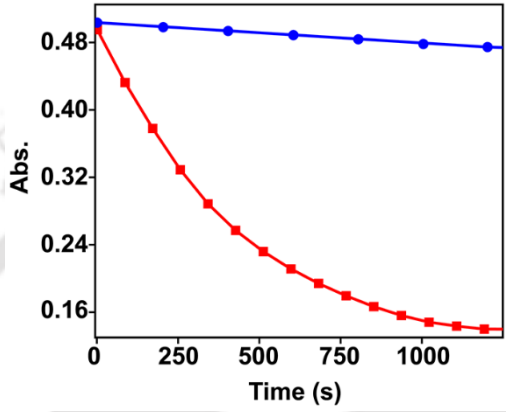

Figure VII. Change in absorption with time upon addition of 150 mM of CCA (■) and 1-d-CCA (●) to an acetonitrile solution (1 mM) of ***6****.*

Conclusions and future scope

Two types of mechanisms could achieve aldehyde biotransformation – one is the oxidation of the aldehyde to the carboxylic acid. The other is oxidative deformylation followed by conversion into one carbon reduced (n-1) product. The later process received much attention because of its similarity in reaction pathways with cholesterol and steroidogenesis's biosynthesis. The species responsible for the transformation of the carboxylic acid is considered to be an electrophilic metal-oxo. In contrast, the deformylation reaction proceeds via a nucleophilic attack of metal-bound peroxide to the aldehyde group's carbonyl carbon. Concomitant β-scission gives formate and less stable alkyl radical with

one less carbon than the parent compound as the product. The alkyl radical afterward transformed either into the final product. The physical and chemical properties of this alkyl radical control the nature of the product formed in the reaction. This research has explored the mechanism of aldehyde deformylation by nonheme transition metal-peroxo intermediates and the effect of ligand structure on their reactivity.

We have discovered for Cu and Mn systems, the deformylation reaction proceeds via an initial radical formation step, while for Fe systems, both types of possibilities are there. These results enlightened the vision about the aldehyde deformylation by metal(III)-peroxo with a new light. As discussed earlier, aldehyde's transformation to hydrocarbon in a single step by a biochemical process will help reduce greenhouse gases and be an efficient conversion step in synthesizing larger molecules essential for pharmaceutical application. The information obtained from this research will help manipulate the catalyst's efficiency and selectivity of the subject. The successful replacement for fossil fuel might not be possible at the moment on a large scale. Still, those catalysts can replace the use of fossil feedstock to generate other commodity products, and the findings from this research will lead to an essential step towards that direction.

Chapter 1: Introduction

1.1 Biorefinery

The emission of greenhouse gases and particulate matter has profoundly impacted climate change by unsettling the earth's radiation balance. The earth's atmosphere is in an equilibrium condition; the incoming flux of solar energy is balanced with the outgoing flux of energy as long-wave radiation. Over time, several radiatively active gases increase concentrations because of various human activities, disrupting the delicate balance of existing energy transfer equilibria in our atmosphere. Human activity has also increased aerosol particles' levels either by direct emission or by emitting the gases responsible. This increasing aerosol particle concentration also disturbs the radiation equilibria and affects human health by creating various lung diseases. Among all the greenhouse gases, CO_2 is the main contributor to anthropogenic radiative forcing.

Fossil fuel burning is the primary reason for increasing the concentration of greenhouse gases and aerosol particles. Apart from their help in changing the earth's climate, there are other problems in using fossil feedstocks in large amounts, and the primary one is that its resources are finite. Scientists are trying to find suitable alternatives for the last few decades, and they came up with various technologies like solar power, nuclear power, biofuels, etc., as alternative energy sources. Many of the so-called first-world countries are reducing their fossil fuel consumption substantially. In economically progressing countries like India, there is a lot of complexity for depending entirely on those alternatives. Apart from the fuel supply, the crude oil refinery

industry also produced various commodity products for everyday uses. Biomass has particular interest among scientists because it can reduce the dependencies on fossil feedstock by generating both fuels and the necessary chemicals in a net carbon neutral biosynthetic pathway.[1-7]

Currently, bioethanol accounts for the maximum shares of the total biofuels used for transportation.[8] Among various biomass types, lignocellulosic materials, e.g., bagasse stover from sugar, forest and crop residues, and short-rotation forest crops, are abundant raw material sources for producing biofuels on earth.[9,10] Its non-edible nature has no competition with the food supply, and its availability across the world helps keep the price fluctuation to a minimum.[11-14] Although significant progress has been effectuated at the laboratory level and various industries have adopted numerous technologies, the primary obstacle in successfully implementing large-scale production is the shortage of biomass. Biomass has less total carbon content than crude oil; even with full conversion, twice the biomass amount is necessary to get the equivalent amount of fuels. Another severe impediment is ethanol's hygroscopic nature, making it incompatible with most of the infrastructure currently used in automobiles. Apart from their hydrophobic nature, long-chain alkanes have very high energy-density, and they are the primary component of all fossil-based fuels. Acquiring highly pure ethanol is extremely energy-consuming, which makes biofuels a costlier option. The high energy density of fossil fuels and overall cost-effectiveness is one of the primary reasons for not utilizing biofuels entirely as an alternative to gasoline or other petroleum fuels in developing countries.[15]

Biosynthesis of long-chain alkanes or, for that matter, hydrocarbons, in general, can be tremendously helpful in solving the issue. In a petroleum refinery industry, apart from the extensive use of fuels, hydrocarbons are the primary raw material for producing various commodity products. In nature, many living organisms, including plants, insects, and microorganisms, can generate hydrocarbon using different types of metalloenzymes. The long-chain alkane waxes play an essential role in the survival of those organisms. The prospect of using the biosynthesis of hydrocarbon as an alternative to the crude oil refinery systems accelerated the fascination towards mechanistic enzymology.

1.2 Biosynthesis of alkanes

Alkanes are devoid of any functional group, and hence their synthesis is always challenging for a cell.[16] Despite that, many organisms synthesized saturated, unsaturated, and branched alkanes in their systems.[17-20] Insects are highly dependent on pheromones for several life functions like finding food, mate, and getting alert about possible predators; alkanes play a significant role in forming that pheromone. Water-birds use alkane-rich oil to keep their feathers waterproof, helping them fly and maintain body temperature. Plants also produce very-long-chain alkane wax, which accumulates on their leaves and stems and helps prevent water loss and desiccation. Algaes also synthesize long-chain-alkane in large amounts, almost 30% of their dry weight, and store them in the cell's inner and outer wall to utilize them later to supply energy when photosynthesis becomes impossible.[21]

Hydrocarbon biosynthesis has evolved several times; this is understandable because there are three types of mechanisms for forming unfunctionalized alkanes utilizing fatty aldehydes as a precursor. The aldehyde is an intermediate product in the process of long-chain-alkane formation from fatty acids. Aldehyde decarbonylases (AD) are the only known class of enzymes to convert aldehyde to alkanes with one less carbon via carbon-carbon bond cleavage. There are three different kinds of aldehyde decarbonylases known for three different types of organisms, plants, insects, and cyanobacteria. All of them are also structurally different from each other.

Insects like houseflies have aldehyde decarbonylases that contain cytochrome P450 at the active site.[22-27] In contrast, a nonheme dinuclear iron center structurally similar to ferritin is in the enzyme's active site for cyanobacteria.[28-36] Although the evidence for the formation of alkane was observed first in plants; the active site structure is not explicitly understandable. It is assumed to be a metalloenzyme because of its resemblance to the fatty acid hydroxylase superfamily and stearoyl-CoA desaturase.[37] The mechanism of decarbonylation and the final product changes depending on the nature of the active site. The only similarity between insect and bacteria AD systems is that they both contain iron in the active site. In insects, cyanobacteria, and plants, the aldehyde carbon converts to CO_2, HCO_2H, and CO, respectively (Figure 1.1).[21,23,29,30,38]

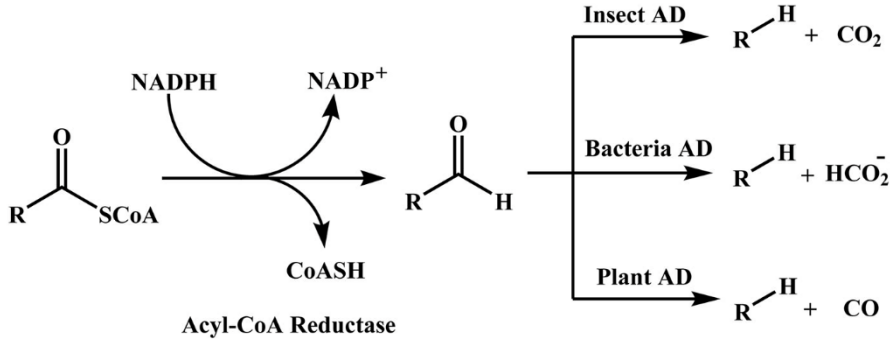

Figure 1.1 Various steps for the biosynthesis of alkanes in nature.

The P450 in insects AD reacts differently than other P450 catalyzed reactions where H atom abstraction of aldehyde followed by OH rebound gives carboxylic acid as the primary product. The proposed mechanism is shown in figure 1.2, in which the iron-oxo species at the active site, resulting from the O-O bond cleavage of the peroxyiron species, abstract an electron from the aldehyde group.

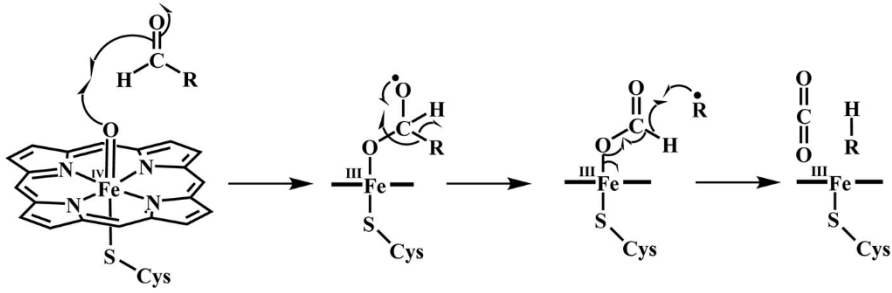

Figure 1.2 Proposed mechanism for the deformylation of aldehydes by insects AD.

The nucleophilic attack to the aldehyde carbon by the reduced iron-oxo species occurs, followed by the formation of an iron-bound formyl radical, and then the H atom abstraction from the iron-bound formyl radical forms CO_2. The most recently discovered pathway for alkane biosynthesis is the cyanobacterial pathway. Cyanobacterial aldehyde decarbonylase is also known as cyanobacterial aldehyde deformylating oxygenase (cADO). The name suggests this enzyme's mechanism; the end product for cADO is entirely different from the other two mechanisms. In this case, the aldehyde carbon transformed into formate instead of any gaseous product, unlike the other two mechanisms.

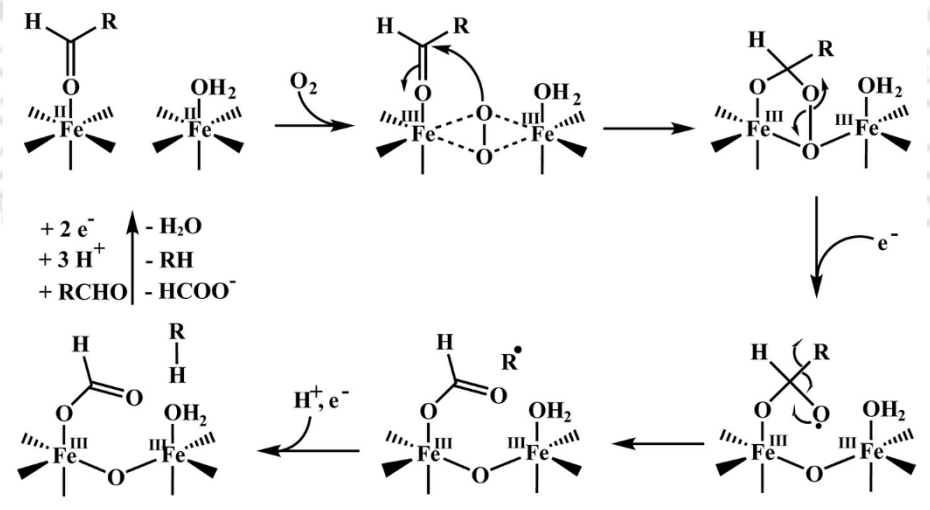

Figure 1.3 Proposed mechanism for cADO activity.

The crystal structure of cADO provides evidence for two nonheme iron centers at its active site, which makes it structurally similar to other nonheme dinuclear

iron enzymes like methane monooxygenase, class I ribonucleotide reductase, and fatty-acyl-ACP desaturase.[31,33,39] The proposed mechanism for the reactivity of the enzyme proceeds via the steps shown in figure 1.3.

In the first step, molecular oxygen binds to the diiron center forming a peroxo bridge. The next step includes a nucleophilic carbonyl attack from the peroxo iron species, followed by an O-O bond cleavage. The O-O bond cleavage requires an electron donation from an external source to support the activity. Biological oxidants like ferredoxin or NADH are suspected of acting as electron donors. Then the alkyl radical forms the alkane via most probably a proton-coupled electron transfer method. The reaction mechanism hypothesis was postulated based on spectroscopic characterization like EPR, UV-Vis, Stopped-flow measurement, and Mössbauer spectroscopy.

The reactivity of cADO has also been studied with some model aldehyde substrates having a relatively smaller carbon chain than natural fatty aldehydes like nonanal and decanal.[40] In these cases, alcohols and aldehydes with one less carbon atom formed as a product, along with alkane and formate. The experimental evidence suggests the possibility of an alternative reaction pathway (Figure 1.4).

In this mechanism, a C-C bond cleavage forms formate and a carbanion. The carbanion is then rapidly protonated to form an alkane. This alkane is further hydroxylated by the Fe(IV)-oxo species to generate alcohol and aldehyde in subsequent steps. This mechanism only occurs with the aldehydes having

medium chain lengths. The kinetics study of natural enzymes has always been a complicated task for many reasons likes solubility, purity, etc. Some other cofactors in vivo might help the catalyst perform their activity, which is difficult to replicate *in vitro*. Among the three different natural decarbonylases, only for the cADO successful kinetics study has been achieved. Kinetic analysis of cADO reveals that the reaction is extremely slow. Various research groups have tried to use different reaction conditions, but the reactivity does not improve much. This slow reactivity of the natural enzymes *in vitro* makes them challenging to use as a catalyst for biofuel biosynthesis on an industrial scale.[41,42]

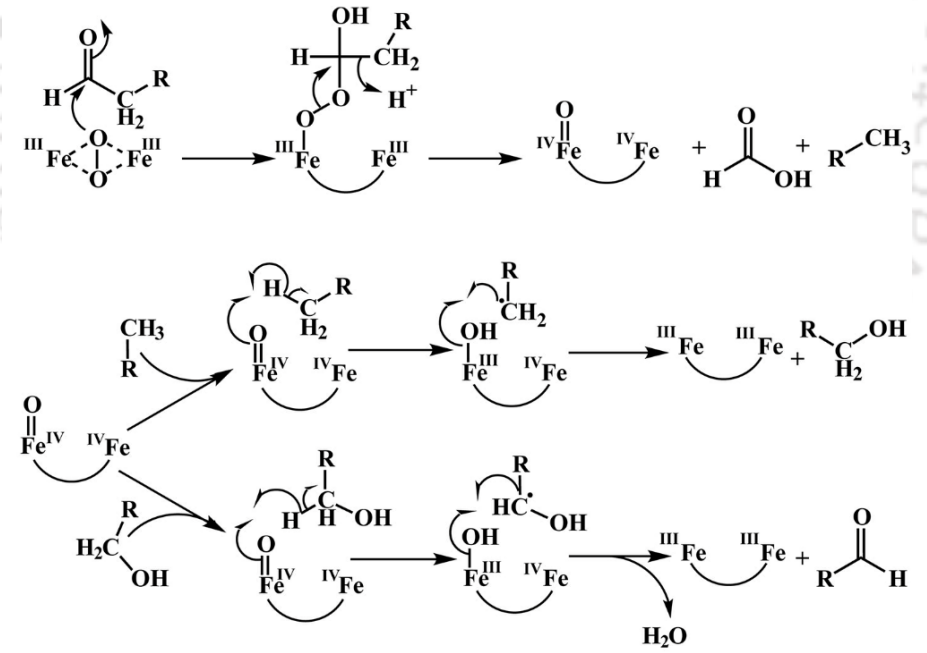

Figure 1.4 Alternate carbanion-based mechanism for cADO.

1.3 Synthetic models

The complicated process of separation of natural enzymes and their purification makes it more of academic interest for biofuel biosynthesis procedure. There was also no clear answer regarding the rate-determining step for the mechanism and the enzyme's slow reactivity despite containing relatively quicker reaction steps. Scientists have put more emphasis on synthetically generated systems to find those answers. The synthetic model compounds include the metal ion, surrounded by organic ligand molecules. They are relatively easy to synthesize and purify; thus, successful production on an industrial scale might be possible,

provided that other parameters are in favor. There are two major genres of synthetic model systems – heme and nonheme enzymes, and both classes of compounds are used extensively to understand the details of biological reactions.[43-52] Though there are dinuclear and mononuclear types of synthetic models, mononuclear models have gained more popularity because of their ease in handling.[53-57] The mononuclear nonheme transition metal-peroxo systems recently got more attention for deformylation reactions among all the various

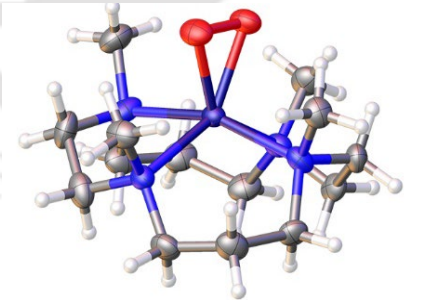

Figure 1.5 First crystal structure of a nonheme iron peroxo.

artificial models available.[56-64] Though the natural AD enzymes contain mainly Fe at the active site; synthetic models have been prepared using different transition metals. A detailed study of the deformylation mechanism by nonheme mononuclear systems using other transition metals would generate a more efficient hydrocarbon biosynthesis catalyst.

Nam and coworkers first reported the crystal structure of a mononuclear TMC ligated side-on Fe(III)-peroxo intermediate in 2011 (Figure 1.5).[64] This report has demonstrated the relative reactivity of a side-on (η^2) and end-on (η^1) Fe(III)-peroxo species in aldehyde deformylation. In earlier research, Nam and coworkers suggest that the side-on Fe(III)-peroxo performs aldehyde deformylation via a nucleophilic carbonyl attack pathway.[63] They have used 2-PPA as the model substrate, and the product analysis established acetophenone as the main product (Figure 1.6).

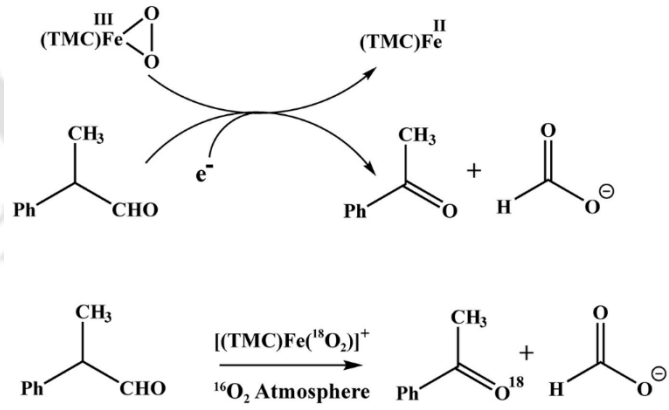

Figure 1.6 The reaction of Fe(III)-peroxo with 2-PPA with isotope labeling experiment.

The isotope labeling study on oxygen atom reveals that the oxygen atom in acetophenone comes from the peroxo group. According to their report, the end-on Fe(III)-peroxo also reacts via the same pathway but at a higher reaction rate. A reactivity order for primary, secondary, and tertiary aldehyde (1° >2° >3°) has also been reported to support the nucleophilic reactivity of end-on intermediate.[64] Que and coworkers also studied the aldehyde deformylation reaction by a side-on Fe(III)-peroxo intermediate.[56] This report has used an H-atom donating solvent THF to mimic the cADO model more accurately.

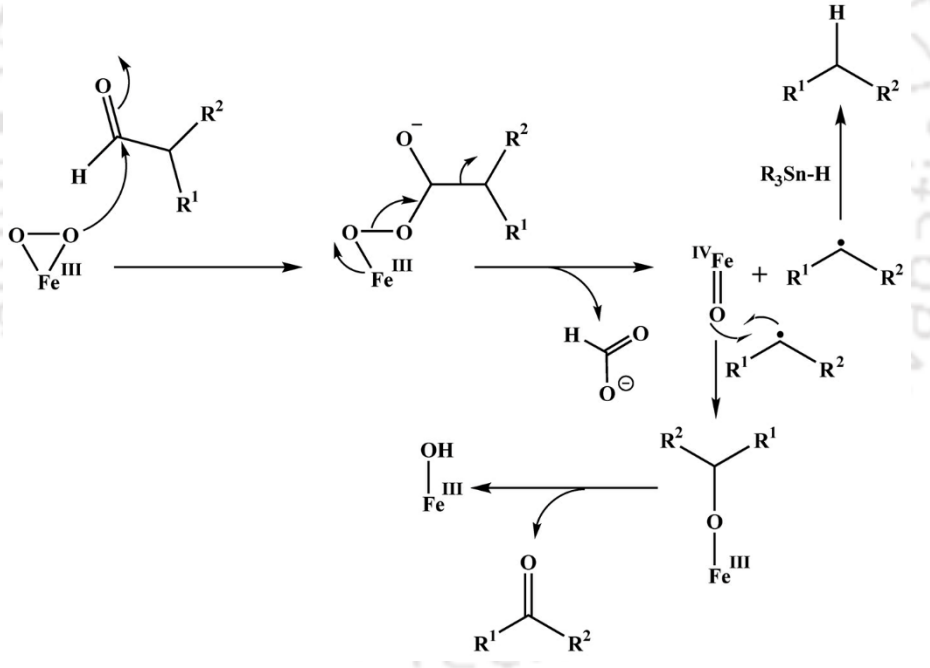

Figure 1.7 Deformylation of 2-PPA by Fe(III)-peroxo in THF.

They have investigated the deformylation of 2-PPA, and according to their studies, the deformylation reaction proceeds via two stages. Firstly, the side-on intermediate reacts with the aldehyde and converts to η^1-OO^- isomer and then converts to a peroxyhemiacetal adduct; in the next step, the O-O bond homolysis of that species generates alkyl radical and formate. In the presence of an H-atom donor, the alkyl radical quickly converts into an alkane instead of forming the hemiacetal with Fe (Figure1.7).

Since the cADO enzyme reacts with long-chain fatty aldehydes, undecanal has been used to replicate the mechanism. The isotope labeling experiment with THF-d8 suggests that the H-atom abstraction occurs from the solvent for long-chain substrates. The formation of an alkane occurs when less polar H-atom donor solvent THF is used. So, the alkane formation depends on the stability and reactivity of the alkyl radical formed. If the alkyl radical is not stabilized either by the substrate structure or by the solvent, it will immediately rebound to form the hemiacetal.

Kitajima and coworkers have first published the crystal structure of a mononuclear nonheme Mn(III)-peroxo species.[65] The mechanism of aldehyde deformylation by mononuclear nonheme Mn(III)-peroxo or, for that matter, any other third-row transition metal-peroxo has been studied extensively by different research groups.[59,61,66-69] Nam and coworkers have generated a TMC ligated mononuclear Mn(III)-peroxo species and investigated the aldehyde deformylation reaction of CCA.[58] The effect of electron donors in the trans-position of the peroxo ligand is also investigated. The presence of any group at

the trans-position affects the reaction in two ways – electronically and structurally.[69] The electron-donating group at the trans-position makes the peroxo complex more nucleophilic by increasing the electron density on the peroxo group. The axial group also pulls the central metal atom towards itself and facilitates the conversion of η^2 to η^1 species, which increases the reaction rate. They have experimented with different axial ligands, and the order of the reactivity is $N_3^- > CF_3CO_2^- > NCS^- > CN^- > NCCH_3$. There have been reports of many other Mn(III)-peroxo complex, but most of them have reported a similar mechanism (Figure 1.8).

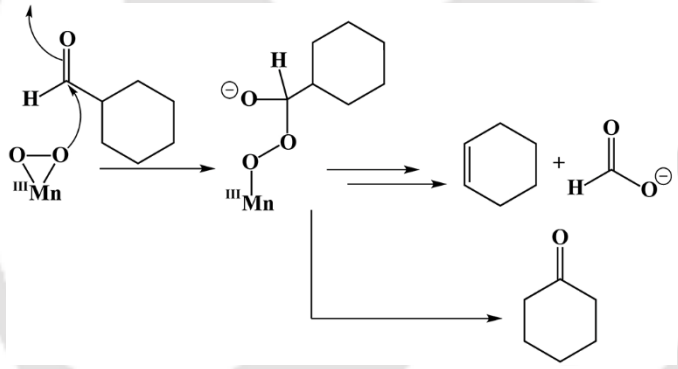

Figure 1.8 Deformylation of CCA by Mn(III)-peroxo complex.

The deformylation reaction of 2-PPA and CCA by TMC containing Co(III)-peroxo intermediate has also been explored.[70] The Co(III)-peroxo catalyzed mechanism is similar to the Fe and Mn systems. Among them, Mn(III)-peroxo has the fastest, and Fe(III)-peroxo has the slowest reactivity for the deformylation of 2-PPA. The metal-oxygen intermediates of other transition

metal ions, e.g., Ni, and Cu, have also been used to study the deformylation reaction mechanism.[71-75] All of them conclude a similar nucleophilic carbonyl attack on the aldehyde by the peroxo group (Figure 1.9).

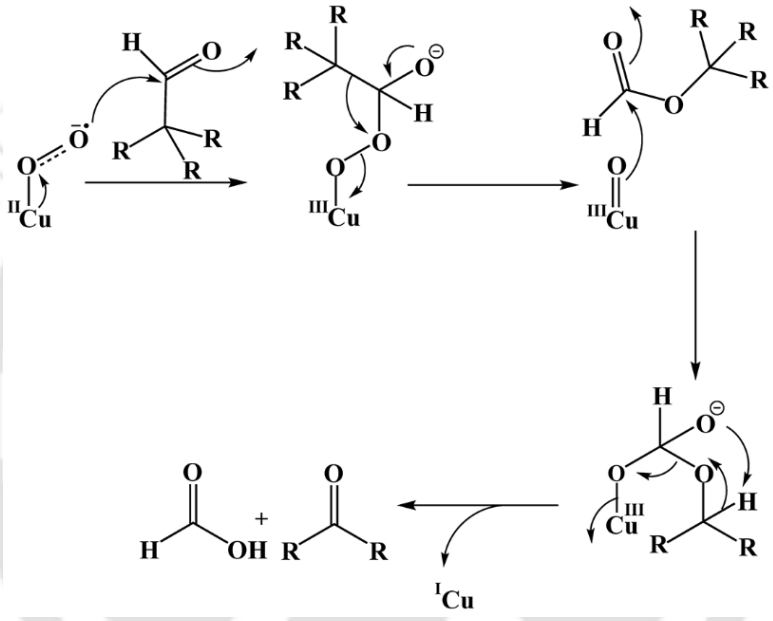

Figure 1.9 Deformylation by Cu(II)-superoxide complex.

In contrast to the conventional carbonyl attack mechanism, our group's previous report suggested a new mechanistic pathway for aldehyde deformylation.[76,77] The investigation of the deformylation reaction of 2-PPA with Mn(III)-peroxo suggests an alternate mechanism of initial H-atom abstraction from aldehyde's α-position (Figure 1.10). Isotope labeling at the α-position of aldehyde helped in establishing the new mechanistic way.

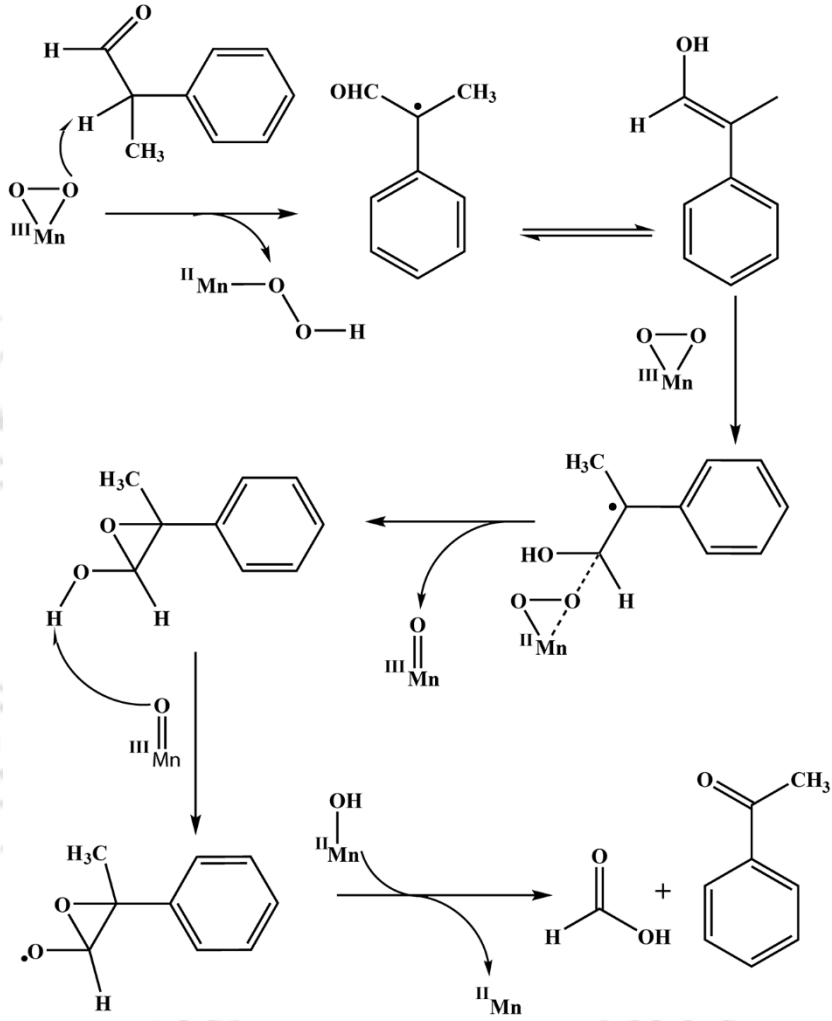

Figure 1.10 HAA mechanism for deformylation by Mn(III)-peroxo complex.

1.4 Aim of the thesis

Acetophenone and cyclohexene are the primary products in the deformylation of 2-PPA and CCA, respectively. Deformylation reaction by nonheme metal-peroxo intermediates also generates formic acid as another product. These are vital chemicals with immense application in various other industries. An accurate vision of the aldehyde deformylation mechanism can direct towards a new efficient way to generate effective catalysts for alkane formation and get other commodity chemicals. It is clear from the previous section that many of the earlier studies used 2-PPA and CCA as model substrates for aldehyde deformylation. However, most of those studies convey that the reaction occurs via nucleophilic attack of the peroxo oxygen at the aldehyde's carbonyl carbon. In our earlier studies, the unveiling of a new mechanical way for the deformylation of 2-PPA by an Mn peroxo system provides an alternate viewpoint in contrast to the popular opinions about its mechanism. We now know that the H atom's availability at the α-position of the aldehyde group controls aldehyde's reactivity. So aldehydes with readily available H atom converts to an alkane faster, provided other conditions remain the same. This information will help enormously in selecting suitable substrates for a well-planned outcome. Apart from the substrate, many different factors influence a reaction, and catalyst is crucial among them. The ligand architecture has a stimulating effect on the reactivity of the metal-oxygen intermediates. Fe, Mn, and Cu's intermediates with different ligand architecture are used to reveal the mechanism in earlier experiments. Our detailed literature study found that there

is little or sometimes no information available on the isotope substitution experiments in the previous reports. Our vision is to study the mechanism of the reactions earlier declared as nucleophilic reactions in the light of the newly developed mechanistic pathway with or without modification in ligand architecture.

This thesis tried to determine the deformylation reaction of 2-PPA by Cu(II)-alkylperoxo intermediates and how ligand architecture affects that. It also revisits CCA's deformylation mechanism by Fe(III) and Mn(III)-peroxo intermediates. Chapter 3 deals with two highly stable at room temperature Cu(II)-alkylperoxo complexes supported by bispidine ligand. The deformylation of 2-PPA by the Cu(II)-alkylperoxo complexes is studied. The induced steric effect of the ligand architecture on reactivity is also determined. In chapter 4, the deformylation of CCA by Fe(III)-peroxo intermediate supported by N4Py ligand is determined. Finally, in chapter 5, we tried to explore the detailed mechanism for deformylation of CCA by Mn(III)-peroxo intermediate supported by bispidine ligand.

1.5 References

1. Goldemberg, J.; Guardabassi, P. Are Biofuels a Feasible Option? Energy Policy 2009, 37 (1), 10–14. https://doi.org/10.1016/j.enpol.2008.08.031.
2. Rajkumar, R.; Yaakob, Z.; Takriff, M. S. Potential of the Micro and Macro Algae for Biofuel Production: A Brief Review. BioResources 2014, 9 (1), 1606–1633. https://doi.org/10.15376/biores.9.1.1606-1633.
3. Behera, S.; Singh, R.; Arora, R.; Sharma, N. K.; Shukla, M.; Kumar, S. Scope of Algae as Third Generation Biofuels. Front. Bioeng. Biotechnol. 2015, 2 (February), 1–13. https://doi.org/10.3389/fbioe.2014.00090.
4. Marques, A. E.; Barbosa, A. T.; Jotta, J.; Coelho, M. C.; Tamagnini, P.; Gouveia, L. Biohydrogen Production by Anabaena Sp. PCC 7120 Wild-Type and Mutants under Different Conditions: Light, Nickel, Propane, Carbon Dioxide and Nitrogen. Biomass and Bioenergy 2011, 35 (10), 4426–4434. https://doi.org/10.1016/j.biombioe.2011.08.014.
5. Hossain, A. B. M. S.; Salleh, A.; Boyce, A. N.; Chowdhury, P.; Naqiuddin, M. Biodiesel Fuel Production from Algae as Renewable Energy. Am. J. Biochem. Biotechnol. 2008, 4 (3 SE-Research Article). https://doi.org/10.3844/ajbbsp.2008.250.254.
6. Shuping, Z.; Yulong, W.; Mingde, Y.; Kaleem, I.; Chun, L.; Tong, J. Production and Characterization of Bio-Oil from Hydrothermal

Liquefaction of Microalgae Dunaliella Tertiolecta Cake. Energy 2010, 35 (12), 5406–5411. https://doi.org/https://doi.org/10.1016/j.energy.2010.07.013.

7. Hughes, A. D.; Kelly, M. S.; Black, K. D.; Stanley, M. S. Biogas from Macroalgae: Is It Time to Revisit the Idea? Biotechnol. Biofuels 2012, 5 (1), 86. https://doi.org/10.1186/1754-6834-5-86.
8. Goldemberg, J. Ethanol for a Sustainable Energy Future. Science. 2007, 315 (5813), 808 – 810. https://doi.org/10.1126/science.1137013.
9. Naik, S. N.; Goud, V. V.; Rout, P. K.; Dalai, A. K. Production of First and Second Generation Biofuels: A Comprehensive Review. Renewable and Sustainable Energy Reviews. Pergamon 1, 2010, 578–597. https://doi.org/10.1016/j.rser.2009.10.003.
10. Sims, R. E. H.; Mabee, W.; Saddler, J. N.; Taylor, M. An Overview of Second Generation Biofuel Technologies. Bioresource Technology. Elsevier Ltd 1, 2010, 1570–1580. https://doi.org/10.1016/j.biortech.2009.11.046.
11. Zabaniotou, A.; Ioannidou, O.; Skoulou, V. Rapeseed Residues Utilization for Energy and 2nd Generation Biofuels. Fuel 2008, 87 (8–9), 1492–1502. https://doi.org/10.1016/j.fuel.2007.09.003.
12. Egües, I.; Alriols, M. G.; Herseczki, Z.; Marton, G.; Labidi, J. Hemicelluloses Obtaining from Rapeseed Cake Residue Generated in the Biodiesel Production Process. J. Ind. Eng. Chem. 2010, 16 (2), 293–298. https://doi.org/10.1016/j.jiec.2010.01.036.

13. Gutiérrez, L. F.; Sánchez, Ó. J.; Cardona, C. A. Process Integration Possibilities for Biodiesel Production from Palm Oil Using Ethanol Obtained from Lignocellulosic Residues of Oil Palm Industry. Bioresour. Technol. 2009, 100 (3), 1227–1237. https://doi.org/10.1016/j.biortech.2008.09.001.

14. Gressel, J. Transgenics Are Imperative for Biofuel Crops. Plant Sci. 2008, 174 (3), 246–263. https://doi.org/https://doi.org/10.1016/j.plantsci.2007.11.009.

15. Ghim, C.-M.; Kim, T.; Mitchell, R. J.; Lee, S. K. Synthetic Biology for Biofuels: Building Designer Microbes from the Scratch. Biotechnol. Bioprocess Eng. 2010, 15 (1), 11–21. https://doi.org/10.1007/s12257-009-3065-5.

16. Buist, P. H. Exotic Biomodification of Fatty Acids. Nat. Prod. Rep. 2007, 24 (5), 1110–1127. https://doi.org/10.1039/B508584P.

17. Cheesbrough, T. M.; Kolattukudy, P. E. Microsomal Preparation from an Animal Tissue Catalyzes Release of Carbon Monoxide from a Fatty Aldehyde to Generate an Alkane. J. Biol. Chem. 1988, 263 (6), 2738–2743. https://doi.org/https://doi.org/10.1016/S0021-9258(18)69130-6.

18. Howard, R. W.; Blomquist, G. J. Ecological, Behavioral, and Biochemical Aspects of Insect Hydrocarbons. Annu. Rev. Entomol. 2004, 50 (1), 371–393. https://doi.org/10.1146/annurev.ento.50.071803.130359.

19. Bernard, A.; Joubès, J. Arabidopsis Cuticular Waxes: Advances in Synthesis, Export and Regulation. Prog. Lipid Res. 2013, 52 (1), 110–129. https://doi.org/https://doi.org/10.1016/j.plipres.2012.10.002.

20. Ladygina, N.; Dedyukhina, E. G.; Vainshtein, M. B. A Review on Microbial Synthesis of Hydrocarbons. Process Biochem. 2006, 41 (5), 1001–1014. https://doi.org/https://doi.org/10.1016/j.procbio.2005.12.007.

21. Dennis, M. W.; Kolattukudy, P. E. Alkane Biosynthesis by Decarbonylation of Aldehyde Catalyzed by a Microsomal Preparation from Botryococcus Braunii. Arch. Biochem. Biophys. 1991, 287 (2), 268–275. https://doi.org/10.1016/0003-9861(91)90478-2.

22. Qiu, Y.; Tittiger, C.; Wicker-Thomas, C.; Le Goff, G.; Young, S.; Wajnberg, E.; Fricaux, T.; Taquet, N.; Blomquist, G. J.; Feyereisen, R. An Insect-Specific P450 Oxidative Decarbonylase for Cuticular Hydrocarbon Biosynthesis. Proc. Natl. Acad. Sci. U. S. A. 2012, 109 (37), 14858–14863. https://doi.org/10.1073/pnas.1208650109.

23. Reed, J. R.; Vanderwel, D.; Choi, S.; George Pomonis, J.; Reitz, R. C.; Blomquist, G. J. Unusual Mechanism of Hydrocarbon Formation in the Housefly: Cytochrome P450 Converts Aldehyde to the Sex Pheromone Component (Z)-9-Tricosene and CO_2. Proc. Natl. Acad. Sci. U. S. A. 1994, 91 (21), 10000–10004. https://doi.org/10.1073/pnas.91.21.10000.

24. Souda, P.; Ryan, C. M.; Cramer, W. A.; Whitelegge, J. Profiling of Integral Membrane Proteins and Their Post Translational Modifications Using High-Resolution Mass Spectrometry. Methods 2011, 55 (4), 330–336. https://doi.org/https://doi.org/10.1016/j.ymeth.2011.09.019.

25. Jia, C.; Li, M.; Li, J.; Zhang, J.; Zhang, H.; Cao, P.; Pan, X.; Lu, X.; Chang, W. Structural Insights into the Catalytic Mechanism of Aldehyde-Deformylating Oxygenases. Protein Cell 2015, 6 (1), 55–67. https://doi.org/10.1007/s13238-014-0108-2.

26. Meunier, B.; de Visser, S. P.; Shaik, S. Mechanism of Oxidation Reactions Catalyzed by Cytochrome P450 Enzymes. Chem. Rev. 2004, 104 (9), 3947–3980. https://doi.org/10.1021/cr020443g.

27. Newcomb, M.; Hollenberg, P. F.; Coon, M. J. Multiple Mechanisms and Multiple Oxidants in P450-Catalyzed Hydroxylations. Arch. Biochem. Biophys. 2003, 409 (1), 72–79. https://doi.org/https://doi.org/10.1016/S0003-9861(02)00445-9.

28. Schirmer, A.; Rude, M. A.; Li, X.; Popova, E.; del Cardayre, S. B. Microbial Biosynthesis of Alkanes. Science 2010, 329 (5991), 559 – 562. https://doi.org/10.1126/science.1187936.

29. Warui, D. M.; Li, N.; Nørgaard, H.; Krebs, C.; Bollinger, J. M.; Booker, S. J. Detection of Formate, Rather than Carbon Monoxide, As the Stoichiometric Coproduct in Conversion of Fatty Aldehydes to Alkanes by a Cyanobacterial Aldehyde Decarbonylase. J. Am. Chem. Soc. 2011, 133 (10), 3316–3319. https://doi.org/10.1021/ja111607x.

30. Das, D.; Eser, B. E.; Han, J.; Sciore, A.; Marsh, E. N. G. Oxygen-Independent Decarbonylation of Aldehydes by Cyanobacterial Aldehyde Decarbonylase: A New Reaction of Diiron Enzymes. Angew. Chemie Int. Ed. 2011, 50 (31), 7148–7152. https://doi.org/https://doi.org/10.1002/anie.201101552.

31. Krebs, C.; Bollinger, J. M.; Booker, S. J. Cyanobacterial Alkane Biosynthesis Further Expands the Catalytic Repertoire of the Ferritin-like 'Di-Iron-Carboxylate' Proteins. Curr. Opin. Chem. Biol. 2011, 15 (2), 291–303. https://doi.org/https://doi.org/10.1016/j.cbpa.2011.02.019.

32. Li, N.; Chang, W.; Warui, D. M.; Booker, S. J.; Krebs, C.; Bollinger, J. M. Evidence for Only Oxygenative Cleavage of Aldehydes to Alk(a/e)nes and Formate by Cyanobacterial Aldehyde Decarbonylases. Biochemistry 2012, 51 (40), 7908–7916. https://doi.org/10.1021/bi300912n.

33. Wallar, B. J.; Lipscomb, J. D. Dioxygen Activation by Enzymes Containing Binuclear Non-Heme Iron Clusters. Chem. Rev. 1996, 96 (7), 2625–2657. https://doi.org/10.1021/cr9500489.

34. Buer, B. C.; Paul, B.; Das, D.; Stuckey, J. A.; Marsh, E. N. G. Insights into Substrate and Metal Binding from the Crystal Structure of Cyanobacterial Aldehyde Deformylating Oxygenase with Substrate Bound. ACS Chem. Biol. 2014, 9 (11), 2584–2593. https://doi.org/10.1021/cb500343j.

35. Li, N.; Nørgaard, H.; Warui, D. M.; Booker, S. J.; Krebs, C.; Bollinger, J. M. Conversion of Fatty Aldehydes to Alka(e)nes and Formate by a Cyanobacterial Aldehyde Decarbonylase: Cryptic Redox by an Unusual Dimetal Oxygenase. J. Am. Chem. Soc. 2011, 133 (16), 6158–6161. https://doi.org/10.1021/ja2013517.

36. Paul, B.; Das, D.; Ellington, B.; Marsh, E. N. G. Probing the Mechanism of Cyanobacterial Aldehyde Decarbonylase Using a Cyclopropyl Aldehyde. J. Am. Chem. Soc. 2013, 135 (14), 5234–5237. https://doi.org/10.1021/ja3115949.

37. Aarts, M. G.; Keijzer, C. J.; Stiekema, W. J.; Pereira, A. Molecular Characterization of the CER1 Gene of Arabidopsis Involved in Epicuticular Wax Biosynthesis and Pollen Fertility. Plant Cell 1995, 7 (12), 2115 – 2127. https://doi.org/10.1105/tpc.7.12.2115.

38. Cheesbrough, T. M.; Kolattukudy, P. E. Alkane Biosynthesis by Decarbonylation of Aldehydes Catalyzed by a Particulate Preparation from Pisum Sativum. Proc. Natl. Acad. Sci. U. S. A. 1984, 81 (21), 6613–6617. https://doi.org/10.1073/pnas.81.21.6613.

39. Khara, B.; Menon, N.; Levy, C.; Mansell, D.; Das, D.; Marsh, E. N. G.; Leys, D.; Scrutton, N. S. Production of Propane and Other Short-Chain Alkanes by Structure-Based Engineering of Ligand Specificity in Aldehyde-Deformylating Oxygenase. ChemBioChem 2013, 14 (10), 1204–1208.

https://doi.org/https://doi.org/10.1002/cbic.201300307.

40. Suda, K.; Kikkawa, T.; Nakajima, S.; Takanami, T. Highly Regio- and Stereoselective Rearrangement of Epoxides to Aldehydes Catalyzed by High-Valent Metalloporphyrin Complex, Cr(TPP)OTf. J. Am. Chem. Soc. 2004, 126 (31), 9554–9555. https://doi.org/10.1021/ja047104k.
41. Akhtar, M. K.; Turner, N. J.; Jones, P. R. Carboxylic Acid Reductase Is a Versatile Enzyme for the Conversion of Fatty Acids into Fuels and Chemical Commodities. Proc. Natl. Acad. Sci. 2013, 110 (1), 87 – 92. https://doi.org/10.1073/pnas.1216516110.
42. Howard, T. P.; Middelhaufe, S.; Moore, K.; Edner, C.; Kolak, D. M.; Taylor, G. N.; Parker, D. A.; Lee, R.; Smirnoff, N.; Aves, S. J.; Love, J. Synthesis of Customized Petroleum-Replica Fuel Molecules by Targeted Modification of Free Fatty Acid Pools in Escherichia Coli. Proc. Natl. Acad. Sci. U. S. A. 2013, 110 (19), 7636–7641. https://doi.org/10.1073/pnas.1215966110.
43. Solomon, E. I.; Brunold, T. C.; Davis, M. I.; Kemsley, J. N.; Lee, S. K.; Lehnert, N.; Neese, F.; Skulan, A. J.; Yang, Y. S.; Zhou, J. Geometric and Electronic Structure/Function Correlations in Non-Heme Iron Enzymes. Chem. Rev. 2000, 100 (1), 235–349. https://doi.org/10.1021/cr9900275.
44. Kovaleva, E. G.; Lipscomb, J. D. Crystal Structures of Fe2+ Dioxygenase Superoxo, Alkylperoxo, and Bound Product Intermediates. Science 2007, 316 (5823), 453–457. https://doi.org/10.1126/science.1134697.

45. Park, M. J.; Lee, J.; Sun, Y.; Kim, J.; Nam, W. Reactivities of Mononuclear Non-Heme Iron Intermediates Including Evidence That Iron(III) Hydroperoxo Species Is a Sluggish Oxidant. Journal of the American Chemical Society. 2006, 2630–2634. https://doi.org/10.1021/ja055709q.

46. Kim, Y. M.; Cho, K. Bin; Cho, J.; Wang, B.; Li, C.; Shaik, S.; Nam, W. A Mononuclear Non-Heme High-Spin Iron(III)-Hydroperoxo Complex as an Active Oxidant in Sulfoxidation Reactions. J. Am. Chem. Soc. 2013, 135 (24), 8838–8841. https://doi.org/10.1021/ja404152q.

47. So, H.; Park, Y. J.; Cho, K. Bin; Lee, Y. M.; Seo, M. S.; Cho, J.; Sarangi, R.; Nam, W. Spectroscopic Characterization and Reactivity Studies of a Mononuclear Nonheme Mn(III)-Hydroperoxo Complex. J. Am. Chem. Soc. 2014, 136 (35), 12229–12232. https://doi.org/10.1021/ja506275q.

48. Cho, J.; Sarangi, R.; Annaraj, J.; Kim, S. Y.; Kubo, M.; Ogura, T.; Solomon, E. I.; Nam, W. Geometric and Electronic Structure and Reactivity of a Mononuclear Side-on Nickel(III)-Peroxo Complex. Nat. Chem. 2009, 1 (7), 568–572. https://doi.org/10.1038/nchem.366.

49. Geiger, R. A.; Leto, D. F.; Chattopadhyay, S.; Dorlet, P.; Anxolabéhère-Mallart, E.; Jackson, T. A. Geometric and Electronic Structures of Peroxomanganese(III) Complexes Supported by Pentadentate Amino-Pyridine and -Imidazole Ligands. Inorg. Chem. 2011, 50 (20), 10190–10203. https://doi.org/10.1021/ic201168j.

50. Goto, Y.; Wada, S.; Morishima, I.; Watanabe, Y. Reactivity of Peroxoiron(III) Porphyrin Complexes: Models for Deformylation

Reactions Catalyzed by Cytochrome P-450. J. Inorg. Biochem. 1998, 69 (4), 241–247. https://doi.org/10.1016/S0162-0134(97)10029-0.

51. Selke, M.; Valentine, J. S. Switching on the Nucleophilic Reactivity of a Ferric Porphyrin Peroxo Complex. J. Am. Chem. Soc. 1998, 120 (11), 2652–2653. https://doi.org/10.1021/ja9733301

52. Sisemore, M. F.; Burstyn, J. N.; Valentine, J. S. Epoxidation of Electron-Deficient Olefins by a Nucleophilic Iron(III) Peroxo Porphyrinato Complex, Peroxo(Tetramesitylporphyrina-to)Ferrate(1-). Angew. Chemie (International Ed. English) 1996, 35 (2), 206–208. https://doi.org/10.1002/anie.199602061.

53. Nam, W. High-Valent Iron(IV)-Oxo Complexes of Heme and Nonheme Ligands in Oxygenation Reactions. Acc. Chem. Res. 2007, 40 (7), 522–531. https://doi.org/10.1021/ar700027f.

54. Hazell, A.; McKenzie, C. J.; Nielsen, L. P.; Schindler, S.; Weitzer, M. Mononuclear Non-Heme Iron(III) Peroxide Complexes: Syntheses, Characterisation, Mass Spectrometric and Kinetic Studies. J. Chem. Soc. Dalt. Trans. 2002, 3, 310–317. https://doi.org/10.1039/b103844n.

55. Kripli, B.; Szávuly, M.; Csendes, F. V.; Kaizer, J. Functional Models of Nonheme Diiron Enzymes: Reactivity of the μ-Oxo-μ-1,2-Peroxo-Diiron(III) Intermediate in Electrophilic and Nucleophilic Reactions. Dalt. Trans. 2020, 49 (6), 1742–1746. https://doi.org/10.1039/c9dt04551a.

56. Shokri, A.; Que, L. Conversion of Aldehyde to Alkane by a Peroxoiron(III) Complex: A Functional Model for the Cyanobacterial

Aldehyde-Deformylating Oxygenase. J. Am. Chem. Soc. 2015, 137 (24), 7686–7691. https://doi.org/10.1021/jacs.5b01053.

57. Sankaralingam, M.; Jeon, S. H.; Lee, Y.-M.; Seo, M. S.; Ohkubo, K.; Fukuzumi, S.; Nam, W. An Amphoteric Reactivity of a Mixed-Valent Bis(μ-Oxo)Dimanganese(III, IV) Complex Acting as an Electrophile and a Nucleophile . Dalton Transactions. 2016, 376–383. https://doi.org/10.1039/C5DT04292E

58. Seo, M. S.; Kim, J. Y.; Annaraj, J.; Kim, Y.; Lee, Y. M.; Kim, S. J.; Kim, J.; Nam, W. $[Mn(Tmc)(O_2)]^+$: A Side-on Peroxido Manganese(III) Complex Bearing a Nonheme Ligand. Angew. Chemie - Int. Ed. 2007, 46 (3), 377–380. https://doi.org/10.1002/anie.200603414.

59. Colmer, H. E.; Howcroft, A. W.; Jackson, T. A. Formation, Characterization, and O-O Bond Activation of a Peroxomanganese(III) Complex Supported by a Cross-Clamped Cyclam Ligand. Inorg. Chem. 2016, 55 (5), 2055–2069. https://doi.org/10.1021/acs.inorgchem.5b02398.

60. Sankaralingam, M.; Lee, Y.-M.; Jeon, S. H.; Seo, M. S.; Cho, K.-B.; Nam, W. A Mononuclear Manganese(III)–Hydroperoxo Complex: Synthesis by Activating Dioxygen and Reactivity in Electrophilic and Nucleophilic Reactions. Chem. Commun. 2018, 54 (10), 1209–1212. https://doi.org/10.1039/C7CC09492B.

61. Geiger, R. A.; Chattopadhyay, S.; Day, V. W.; Jackson, T. A. Nucleophilic Reactivity of a Series of Peroxomanganese(III) Complexes Supported by Tetradentate Aminopyridyl Ligands. Dalt. Trans. 2011, 40 (8), 1707–1715. https://doi.org/10.1039/c0dt01570a.

62. Leto, D. F.; Chattopadhyay, S.; Day, V. W.; Jackson, T. A. Reaction Landscape of a Pentadentate N5-Ligated Mn^{II} Complex with O_2^- and H_2O_2 Includes Conversion of a Peroxomanganese(III) Adduct to a Bis(μ-Oxo)Dimanganese(III, IV) Species. J. Chem. Soc. Dalt. Trans. 2013, 42 (36), 13014–13025. https://doi.org/10.1039/c3dt51277k.

63. Annaraj, J.; Suh, Y.; Seo, M. S.; Kim, S. O.; Nam, W. Mononuclear Nonheme Ferric-Peroxo Complex in Aldehyde Deformylation. Chem. Commun. 2005, No. 36, 4529–4531. https://doi.org/10.1039/b505562h.

64. Cho, J.; Jeon, S.; Wilson, S. A.; Liu, L. V.; Kang, E. A.; Braymer, J. J.; Lim, M. H.; Hedman, B.; Hodgson, K. O.; Valentine, J. S.; Solomon, E. I.; Nam, W. Structure and Reactivity of a Mononuclear Non-Haem Iron(III)-Peroxo Complex. Nature 2011, 478 (7370), 502–505. https://doi.org/10.1038/nature10535.

65. Kitajima, N.; Komatsiizaki, H.; Hikichi, S.; Osawa, M.; Moro-oka, Y. A Monomeric Side-On Peroxo Manganese(III) Complex: $Mn(O_2)$(3,5-iPr_2pzH)(HB(3,5-iPr_2pz)$_3$). J. Am. Chem. Soc. 1994, 116 (25), 11596–11597. https://doi.org/10.1021/ja00104a061

66. Denler, M. C.; Wijeratne, G. B.; Rice, D. B.; Colmer, H. E.; Day, V. W.; Jackson, T. A. MnIII-Peroxo Adduct Supported by a New Tetradentate

Ligand Shows Acid-Sensitive Aldehyde Deformylation Reactivity. Dalt. Trans. 2018, 47 (38), 13442–13458. https://doi.org/10.1039/c8dt02300j.

67. Narulkar, D. D.; Ansari, A.; Vardhaman, A. K.; Harmalkar, S. S.; Lingamallu, G.; Dhavale, V. M.; Sankaralingam, M.; Das, S.; Kumar, P.; Dhuri, S. N. A Side-on Mn(III)–Peroxo Supported by a Nonheme Pentadentate N3Py2 Ligand: Synthesis, Characterization and Reactivity Studies . Dalt. Trans. 2021, 50 (8), 2824. https://doi.org/10.1039/d0dt03706k.
68. Magherusan, A. M.; Kal, S.; Nelis, D. N.; Doyle, L. M.; Farquhar, E. R.; Que, L.; McDonald, A. R. A Mn II Mn III -Peroxide Complex Capable of Aldehyde Deformylation. Angew. Chemie Int. Ed. 2019, 58 (17), 5718–5722. https://doi.org/10.1002/anie.201900717.
69. Annaraj, J.; Cho, J.; Lee, Y.-M.; Kim, S. Y.; Latifi, R.; de Visser, S. P.; Nam, W. Structural Characterization and Remarkable Axial Ligand Effect on the Nucleophilic Reactivity of a Nonheme Manganese(III)–Peroxo Complex. Angew. Chemie Int. Ed. 2009, 48 (23), 4150–4153. https://doi.org/https://doi.org/10.1002/anie.200900118.
70. Jo, Y.; Annaraj, J.; Seo, M. S.; Lee, Y. M.; Kim, S. Y.; Cho, J.; Nam, W. Reactivity of a Cobalt(III)-Peroxo Complex in Oxidative Nucleophilic Reactions. J. Inorg. Biochem. 2008, 102 (12), 2155–2159. https://doi.org/10.1016/j.jinorgbio.2008.08.008.
71. Pirovano, P.; Magherusan, A. M.; McGlynn, C.; Ure, A.; Lynes, A.; McDonald, A. R. Nucleophilic Reactivity of a Copper(II)-Superoxide

Complex. Angew. Chemie - Int. Ed. 2014, 53 (23), 5946–5950. https://doi.org/10.1002/anie.201311152.

72. Kim, J.; Shin, B.; Kim, H.; Lee, J.; Kang, J.; Yanagisawa, S.; Ogura, T.; Masuda, H.; Ozawa, T.; Cho, J. Steric Effect on the Nucleophilic Reactivity of Nickel(III) Peroxo Complexes. Inorg. Chem. 2015, 54 (13), 6176–6183. https://doi.org/10.1021/acs.inorgchem.5b00294.

73. Cho, J.; Kang, H. Y.; Liu, L. V.; Sarangi, R.; Solomon, E. I.; Nam, W. Mononuclear Nickel(II)-Superoxo and Nickel(III)-Peroxo Complexes Bearing a Common Macrocyclic TMC Ligand. Chem. Sci. 2013, 4 (4), 1502–1508. https://doi.org/10.1039/c3sc22173c.

74. Cho, J.; Sarangi, R.; Annaraj, J.; Kim, S. Y.; Kubo, M.; Ogura, T.; Solomon, E. I.; Nam, W. Geometric and Electronic Structure and Reactivity of a Mononuclear Side-on Nickel(III)-Peroxo Complex. Nat. Chem. 2009, 1 (7), 568–572. https://doi.org/10.1038/nchem.366.

75. Kim, B.; Jeong, D.; Cho, J. Nucleophilic Reactivity of Copper(II)-Alkylperoxo Complexes. Chem. Commun. 2017, 53 (67), 9328–9331. https://doi.org/10.1039/c7cc03965d.

76. Barman, P.; Upadhyay, P.; Faponle, A. S.; Kumar, J.; Nag, S. S.; Kumar, D.; Sastri, C. V.; de Visser, S. P. Deformylation Reaction by a Nonheme Manganese(III)–Peroxo Complex via Initial Hydrogen-Atom

Abstraction. Angew. Chemie - Int. Ed. 2016, 55 (37), 11091–11095. https://doi.org/10.1002/anie.201604412.

77. Cantú Reinhard, F. G.; Barman, P.; Mukherjee, G.; Kumar, J.; Kumar, D.; Kumar, D.; Sastri, C. V.; De Visser, S. P. Keto-Enol Tautomerization Triggers an Electrophilic Aldehyde Deformylation Reaction by a Nonheme Manganese(III)-Peroxo Complex. J. Am. Chem. Soc. 2017, 139 (50), 18328–18338. https://doi.org/10.1021/jacs.7b10033.

Chapter 2: Materials and methods

2.1 Introduction

Successful kinetic studies of enzyme catalysis or, for that matter, any reaction depend highly on the availability of the ultra-pure reagents. This chapter elucidates the purification of raw materials (if any), synthesis procedure of various ligands, metal complexes, characterization, general experimental and instrumental techniques—more specific experiments related to a particular work illustrated within that particular chapter.

2.2 Materials

2.2.1 Solvents

All solvents were dried according to the published procedure and distilled under argon before use.[1] Acetonitrile and methanol have been dried using CaH_2 powder; tetrahydrofuran and diethyl ether were dried over sodium in the presence of benzophenone. All the solvents were distilled for 10-12 hours in an argon atmosphere and collected using a cannula.

2.2.2 Substrates

All substrates are of the highest grade commercially available and were used without further purification unless mentioned otherwise. Benzaldehyde and its derivatives, 2-phenylpropionaldehyde (2-PPA), cyclohexanecarbaxaldehyde (CCA), valeraldehyde, 2-methyl-butyraldehyde, trimethylacetaldehyde, and triphenylphosphine were purchased from Sigma-Aldrich. Deuterated aldehydes like 2-d-2-phenylprpionaldehyde 90 atom % D (α-d-2-PPA), 2-d-

cyclclohexanecarbaxaldehyde 94 atom % D (α-d-CCA), and 1-d-cyclclohexanecarbaxaldehyde 92 atom% D (1-d-CCA) were purchased from RVL Scientific & Engineering Pvt. Ltd. Other substrates like 2-methyl-2-phenylpropionaldehyde and 2-methyl-cyclohexanecarbaxaldehyde were synthesized according to a previously reported procedure in the literature.[2,3]

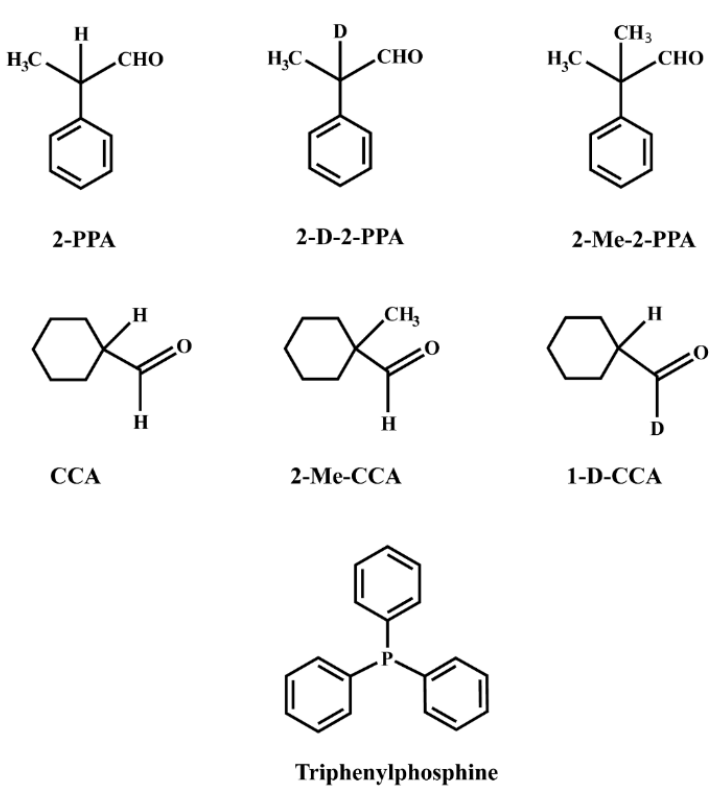

Figure 2.1 Structure of the model substrates used in the thesis.

2.2.2.1 Procedure for the synthesis of 2-Me-2-PPA

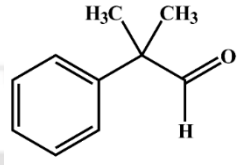

A solution of 2-phenylpropionaldehyde was added dropwise to a suspension of sodium hydride in THF for an hour and stirred for another 30 minutes. Then methyl iodide was added dropwise to the reaction mixture keeping the temperature below 15 °C. The reaction mixture was stirred for an hour at 15 °C then allowed to come to room temperature. The addition of 200 ml saturated aqueous $NaHCO_3$ solution quenched the reaction. The reaction mixture was extracted three times with 50 ml ether. Combined organic phases were dried over anhydrous magnesium sulfate, filtered, and concentrated by the rotatory evaporator. The pure compound was obtained as a colorless liquid after the vacuum distillation of the crude light-yellow liquid.

^{1}H NMR (600 MHz, $CDCl_3$): δ (ppm) 9.53 (s, 1H), 7.42 (t, J = 7.7 Hz, 2H), 7.32 (t, J = 8.6 Hz, 3H), 1.50 (s, 6H); ^{13}C NMR (151 MHz, $CDCl_3$): δ (ppm) 202.3 (s), 141.2 (s), 128.9 (s), 127.3 (s), 126.7 (s), 50.5 (s), 22.5 (s).

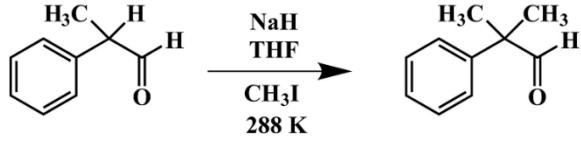

Scheme 2.1 Synthesis of 2-Me-2-PPA.

2.2.2.2 Procedure for the synthesis of 2-Me-CCA

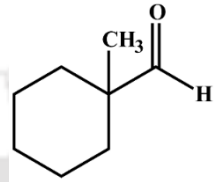

A solution of cyclohexanecarbaxaldehyde in anhydrous CH_2Cl_2 was cooled in ice, then KO^{t}Bu was slowly added to it. Methyl iodide was added to it dropwise for 30 minutes at 0°C. It was then allowed to stir overnight at room temperature. After stirring overnight, the organic phase was washed twice with 50 ml of water, brine, and dried over Na_2SO_4. The solvent was removed under reduced pressure. The crude product is then distilled under a vacuum to get the pure colorless liquid.

^{1}H NMR (600 MHz, $CDCl_3$): δ (ppm) 9.42 (s, 1H), 1.85 – 1.80 (m, 2H), 1.56 (dd, J = 13.3, 6.7 Hz, 2H), 1.46 (m, 1H), 1.37 – 1.32 (m, 2H), 1.30 (d, J = 9.6 Hz, 1H), 1.24 (dd, J = 13.3, 9.7 Hz, 2H), 0.99 (s, 3H); ^{13}C NMR (151 MHz, $CDCl_3$): δ (ppm) 206.9 (s), 46.3 (s), 32.4 (s), 25.6 (s), 22.4 (s), 21.8 (s).

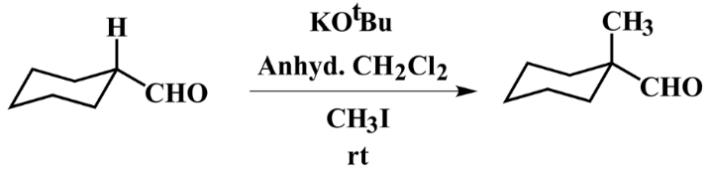

Scheme 2.2 Synthesis of 2-Me-CCA.

2.2.3 Ligands

The synthesis of highly pure ligands is an essential aspect of any synthetic model-based enzyme kinetics. The purity of ligands is a deciding factor in preparing ultrapure metal complexes for the kinetics study. All the ligands used in the thesis are depicted in figure 2.1.

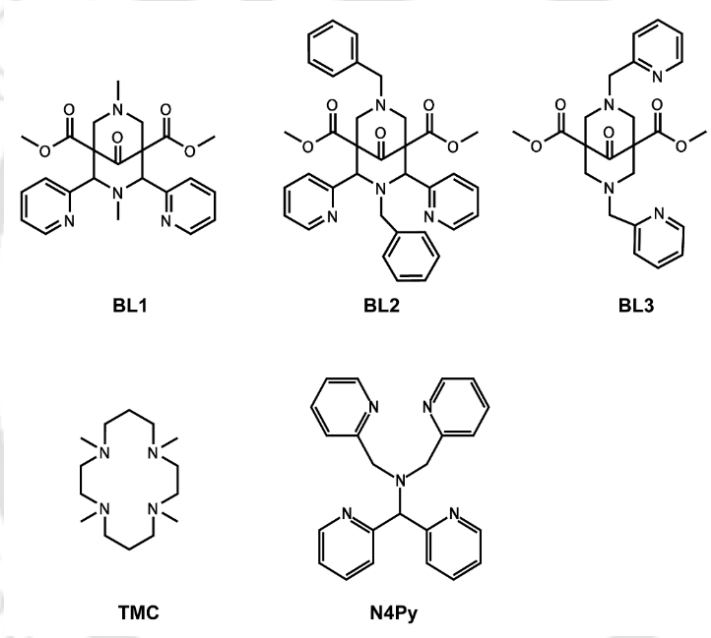

Figure 2.2 Structure of the ligands used in the thesis.

Their synthesis procedure is narrated in this section except for tetramethylcyclam (TMC); it is purchased from available commercial sources. BL1 and N4Py ligands are synthesized following the previously reported methods, and wherever any modification has been made is duly mentioned.[4-7]

2.2.3.1 Procedure for the synthesis of BL1

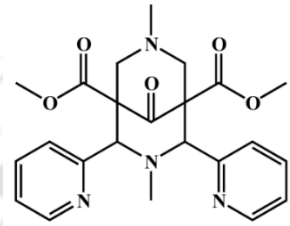

The bispidine ligand BL1 was synthesized according to the procedure reported in the literature. Dimethyl acetone dicarboxylate (7.2 mL, 50 mM) was taken in 20 mL of CH_3OH and was cooled to 0 °C. A solution of pyridine-2-carboxaldehyde (9.5 mL, 100 mM) and methylamine (4.5 mL, 50 mM) were added to it dropwise. After completion of the addition, the solution was allowed to stir at 0 ºC overnight. The white precipitate thus obtained was filtered and washed with cold ethanol and dried in a vacuum. The white solid was recrystallized from ethanol and used for the next step.

To a suspension of the white solid (13.6 g, 35.5 mM) in 200 mL ethanol, aqueous formaldehyde (37%, 6.9 mL, 85.1 mM), and methylamine (3.71 mL, 42.5 mM) were added dropwise. After refluxing for four hours, the dark brown reaction mixture was concentrated and kept inside a freezer. The formation of white precipitation occurs after several days. Recrystallization of the white solid from acetonitrile gives the pure crystalline product (yield: 30%).

^{1}H NMR (600 MHz, $CDCl_3$): δ (ppm) 8.46 (d, J = 4.8 Hz, 2H), 7.90 (d, J = 7.9 Hz, 2H), 7.49 (s, 2H), 7.16 – 7.14 (m, 2H), 4.71 (s, 2H), 3.84 (s, 6H), 3.38 (s,

3H), 3.07 (d, J = 12.6 Hz, 2H), 2.57 (d, J = 12.2 Hz, 2H), 1.99 (s, 3H); ^{13}C NMR (151 MHz, $CDCl_3$): δ (ppm) 203.7 (s), 168.6 (s), 158.4 (s), 149.1 (s), 136.9 (s), 136.2 (s), 130.4 (s), 128.4 (s), 127.6 (s), 123.4 (s), 122.9 (s), 73.8 (s), 62.5 (s), 62.1 (s), 59.0 (s), 52.5 (s), 43.3 (s); ESI-MS (m/z): Calculated for $C_{35}H_{35}N_4O_5^+$: 591.26, found: 591.32. Elemental Analysis: Measured C 70.87, H 5.29, N 9.79; Calculated for $C_{35}H_{34}N_4O_5$ C 71.17, H 5.80, N 9.49.

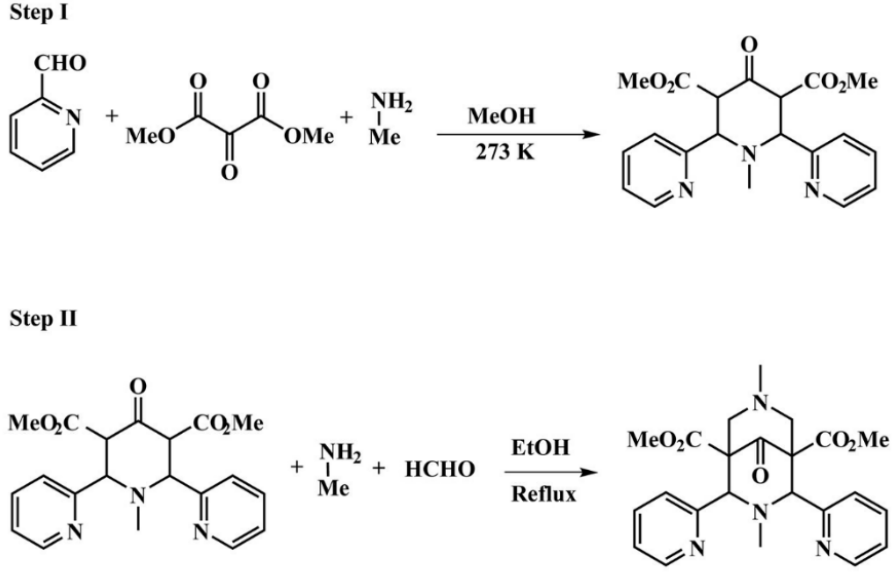

Scheme 2.3 Synthesis of BL1 ligand.

2.2.3.2 Procedure for the synthesis of BL2

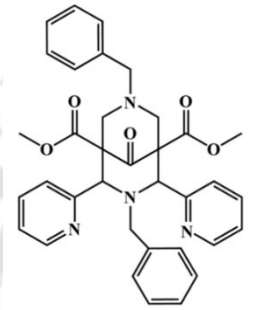

BL2 was synthesized with slight modification in the substrate, but the procedure is the same as used for BL1. Dimethyl acetone dicarboxylate (7.2 mL, 50 mM) was taken in 20 mL of CH_3OH and was cooled to 0 °C. A solution of pyridine-2-carboxaldehyde (9.53 mL, 100 mM) and benzylamine (5.46 mL, 50 mM) were added to it dropwise. After completion of the addition, the solution was allowed to stir at 0 ºC overnight. The white precipitate thus obtained was filtered and washed with cold ethanol and dried in a vacuum. The white solid was recrystallized from ethanol and used for the next step.

To a suspension of the white solid (16.7 g, 36.6 mM) in 200 mL ethanol, aqueous formaldehyde (37%, 7.05 mL, 87 mM), and benzylamine (4.75 mL, 43.5 mM) were added dropwise. After refluxing for four hours, the dark brown reaction mixture was concentrated and kept inside a freezer. The formation of white precipitation occurs after several days. Recrystallization of the white solid from acetonitrile gives the pure crystalline product (yield: 36%).

^{1}H NMR (600 MHz, $CDCl_3$): δ (ppm) 8.54 (s, 2H), 8.02 (d, J = 7.8 Hz, 2H), 7.48 – 7.43 (m, 7H), 7.25 – 7.21 (m, 3H), 7.18 – 7.15 (m, 2H), 6.89 (d, J = 7.0 Hz, 2H), 5.15 (s, 2H), 3.77 (s, 6H), 3.52 (s, 2H), 3.41 (s, 2H), 3.12 (d, J = 12.2 Hz, 2H), 2.54 (d, J = 12.2 Hz, 2H); ^{13}C NMR (151 MHz, $CDCl_3$): δ (ppm) 203.8 (s), 168.8 (s), 158.3 (s), 149.4 (s), 137.1 (s), 136.1 (s), 133.3 (s), 130.8 (d, J = 18.5 Hz), 128.7 (s), 128.3 (s), 127.9 (s), 127.6 (s), 124.7 (s), 123.1 (s), 69.2 (s), 62.8 (s), 62.3 (s), 59.7 (s), 55.0 (s), 52.78 (s); ESI-MS (*m/z*): Calculated for $C_{35}H_{35}N_4O_5^+$: 591.26, found: 591.32. Elemental Analysis: Measured C 70.72, H 5.36, N 9.72; Calculated for $C_{35}H_{34}N_4O_5$ C 71.17, H 5.80, N 9.49.

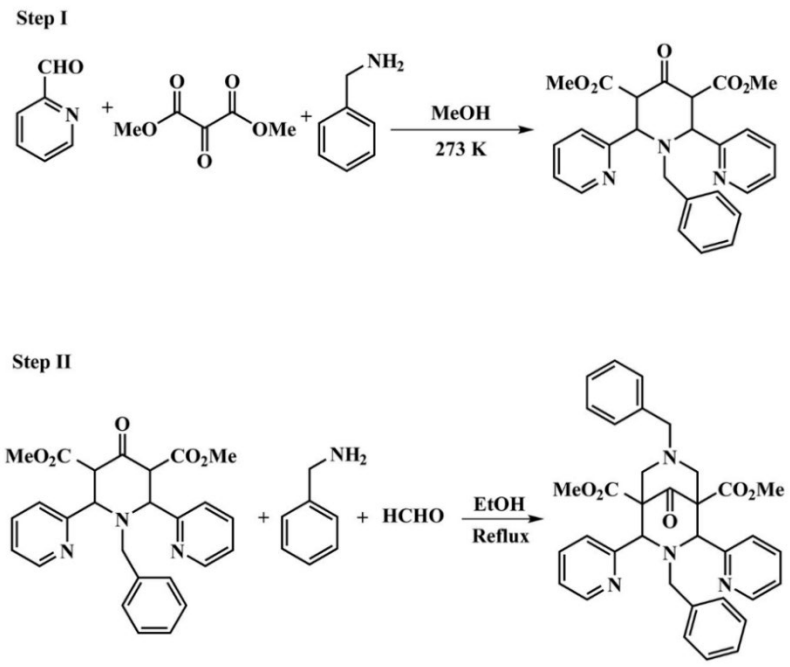

Scheme 2.4 Synthesis of BL2 ligand.

2.2.3.3 Procedure for the synthesis of BL3

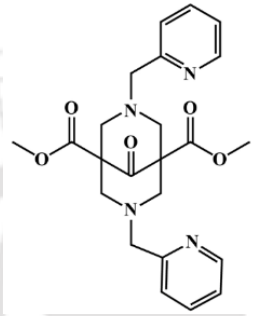

The bispidine ligand BL3 was synthesized according to the procedure reported in the literature.[8] Dimethyl acetone dicarboxylate (7.2 mL, 50 mM), formaldehyde (18 mL of 30% solution in water, 100 mM), and benzylamine (11 mL, 50 mM) was added dropwise to an ice-cooled CH_3OH (400 mL). After completion of the addition, the solution was allowed to stir at 0 ºC overnight. Then the reaction mixture was allowed to come to room temperature and stirred for another ten hours. The reaction mixture was concentrated to half its volume, and the precipitate was filtered off. The residue was washed twice with methanol and dried in a vacuum. The pure product was collected as a white powder (yield: 25%).

^{1}H NMR (600 MHz, $CDCl_3$): δ (ppm) 8.52 (d, J = 4.8 Hz, 2H), 7.67 (d, J = 7.6 Hz, 2H), 7.48 (d, J = 7.8 Hz, 2H), 7.21 – 7.18 (m, 2H), 3.85 (s, 4H), 3.72 (s, 6H), 3.39 (d, J = 11.3 Hz, 4H), 3.23 (d, J = 11.3 Hz, 4H); ^{13}C NMR (151 MHz, $CDCl_3$): δ (ppm) 203.6 (s), 170.4 (s), 157.8 (s), 149.1 (s), 136.6 (s), 123.2 (s),

122.4 (s), 62.6 (s), 60.2 (s), 59.1 (s), 52.6 (s); ESI-MS (*m/z*): Calculated for $C_{35}H_{35}N_4O_5^+$: 439.26, found: 439.32

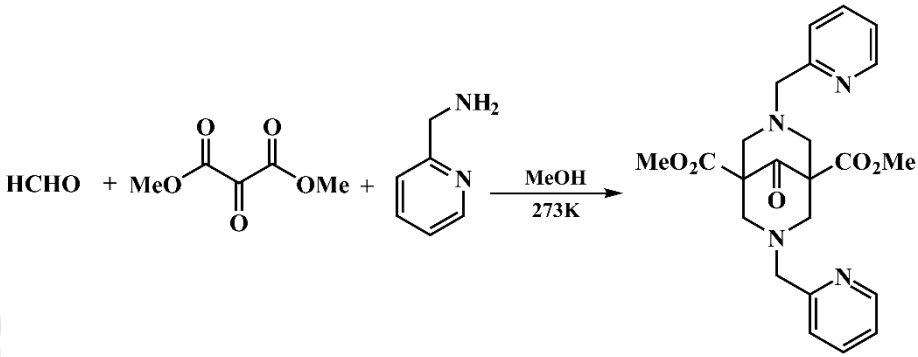

Scheme 2.5 Synthesis of BL3 ligand.

2.2.3.4 Procedure for synthesis of N4Py

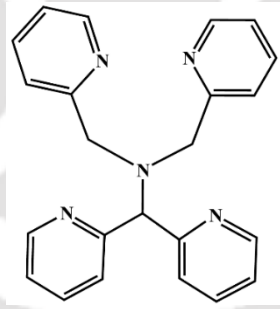

A solution of dipyridyl ketone (5 g, 27 mmol) in ethanol (10 mL) was added dropwise to a solution of hydroxylamine hydrochloride (4.17 g, 60 mmol) in 5 N (20 mL) aqueous NaOH. The reaction mixture was refluxed for two hours. Then ethanol was removed by evaporation. The solution was diluted to one liter

by water. The pH value of the solution was kept at seven by the dropwise addition of HCl. A pinkish-white precipitate dipyridyl ketoxime appeared. Then the precipitate was filtered off and dried for one day.

The dipyridyl ketoxime was added to 90 mL of ethanol and refluxed. Hydrazine hydrate (60 mL) and Zn powder (400 mg) were added in conjugative steps over six hours. Then the solution was kept refluxing overnight. The product obtained was dissolved with a 40 mL 5 N sodium hydroxide solution. Then 2.5 equivalent of 2-picolyl chloride hydrochloride was added to the solution and kept in reflux condition for two days. A brownish-black colored solution appeared, which was neutralized with $HClO_4$; the solid residue thus obtained was filtered and dried. This solid was dissolved in a sodium hydroxide solution of pH=14 and extracted with CH_2Cl_2. The solvent's evaporation gives the semi-solid brown mass as the final product (yield: 3 g).

^{1}H NMR (600 MHz, $CDCl_3$): δ (ppm) 8.60 (d, J = 4.1 Hz, 2H), 8.54 (d, J = 4.1 Hz, 2H), 7.61 (t, J = 6.8 Hz, 3H), 7.52 (t, J = 6.9 Hz, 3H), 7.40 (s, 2H), 7.22 (s, 2H), 7.13 (dd, J = 8.6, 3.6 Hz, 3H), 7.08 – 7.04 (m, 3H), 5.25 (s, 1H), 3.87 (s, 4H); ^{13}C NMR (151 MHz, $CDCl_3$): δ (ppm) 158.78 (s), 158.59 (s), 149.82 (s), 149.69 (s), 136.76 (s), 136.68 (s), 124.34 (s), 123.14 (s), 122.68 (s), 122.23 (s), 72.35 (s), 68.78 (s), 57.34 (s).

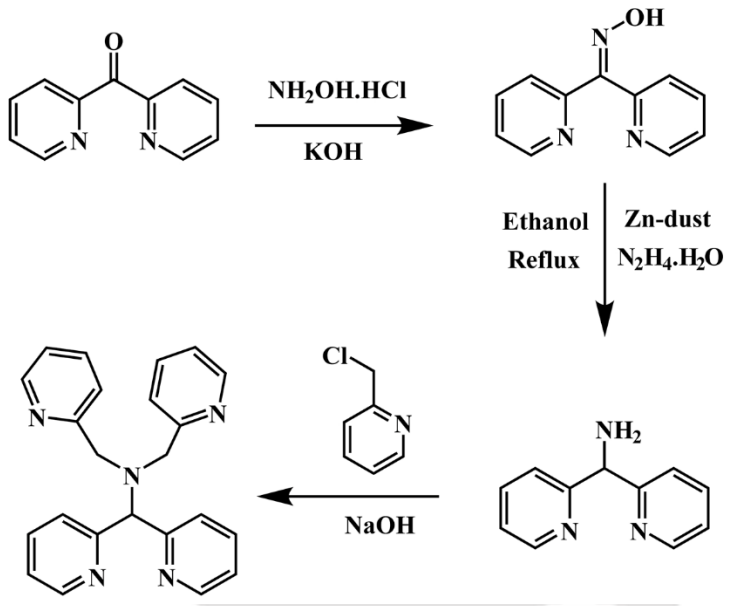

Scheme 2.6 Synthesis of N4Py ligand.

2.2.4 Metal Complexes

Mn, Fe, and Cu complexes are used in this thesis for the kinetics study. Different metal salts like manganese(II) trifluoromethane-sulfonate, iron(II) trifluoromethane-sulfonate, and copper(II) trifluoromethane-sulfonate are used as the precursor to prepare these metal complexes. All the metal complexes except $Fe(TMC)(OTf)_2$ are made using the procedure described below. $Fe(TMC)(OTf)_2$ is prepared according to the literature procedure. $Fe(N4Py)(OTf)_2$ and $Fe(TMC)(OTf)_2$ are characterized using literature procedure.[9,10]

2.2.4.1 General procedure for the synthesis of metal complexes[11]

An acetonitrile solution of metal salt (0.5 mmol) was added dropwise to a ligand (0.5 mmol) solution in the same solvent and stir at room temperature inside a glovebox. After stirring overnight, the reaction mixture was filtered, and the filtrate was layered with diethyl ether. The double-layer solution was kept inside a freezer at 233 K to grow a good quality crystal. The crystals were dried using a vacuum and stored inside the glovebox for further use.

2.2.4.2 Characterization of metal complexes

2.2.4.2.1 $[Cu(BL1)(CH_3CN)](OTf)_2$ (1a)

Physical State: Crystalline; Color: Light blue; Elemental Analysis: Measured C 38.15, H 3.01, N 8.53, Calculated for $C_{27}H_{29}N_5S_2O_{11}F_6Cu$ C 38.55, H 3.47, N 8.33; ESI-MS (m/z): Calculated for $C_{24}H_{26}N_4SO_8F_3Cu^+$ 650.07, found: 650.09; Calculated for $C_{23}H_{26}N_4O_5Cu^{2+}$: 250.56, found: 250.54; Calculated for $C_{25}H_{29}N_5O_5Cu^{2+}$: 271.06, found: 271.06 ; EPR: $g_\perp = 2.082$, $g_\parallel = 2.360$; $A_\parallel = 207$ G.

2.2.4.2.2 $[Cu(BL2)(CH_3CN)](OTf)_2$ (2a)

Physical State: Crystalline; Color: Dark blue; Elemental Analysis: Measured C 46.65, H 3.35, N 7.30, Calculated for $C_{39}H_{37}N_5S_2O_{11}F_6Cu$ C 47.15, H 3.75, N 7.05; ESI-MS (m/z): Calculated for $C_{36}H_{36}N_4SO_9F_3Cu^+$: 820.14, found: 820.24; Calculated for $C_{35}H_{36}N_4O_6Cu^{2+}$: 335.60, found 335.61; EPR: $g_\perp = 2.073$, $g_\parallel = 2.385$; $A_\parallel = 190$ G.

2.2.4.2.3 $[Mn(BL3)](OTf)_2$ (3a)

Physical State: Crystalline; Color: Off white; Elemental Analysis: Measured C 36.65, H 3.02, N 7.26, Calculated for $C_{25}H_{26}F_6MnN_4O_{11}S_2$, C 37.94, H 3.31, N 7.08; ESI-MS (m/z): Calculated for $C_{24}H_{26}F_3MnN_4O_8S^+$: 642.08, found: 642.11.

2.3 Methods

2.3.1 NMR Spectroscopy

^1H and ^{13}C spectra were recorded at room temperature with a Bruker 600/150 MHz spectrometer. ^1H NMR chemical shifts were internally referenced to TMS via residual $CHCl_3$ (δ = 7.26), CH_3OH (δ = 3.31), and DMSO (δ = 2.5). 1D spectra were recorded using a standard pulse technique. All the data were acquired using a 5 mm NMR tube at room temperature. The samples were prepared by dissolving 10-15 mg of an ultra-dried compound in 1 ml of an appropriate deuterated solvent.

2.3.2 EPR Spectroscopy

The X-band electron paramagnetic resonance was measured on a JES-FA200 ESR spectrometer. The measurements were performed at 77 K in an acetonitrile solution. A sample amount of 1 ml of concentration 5 mM was prepared inside a glovebox and filled into the sample tube of diameter 4 mm. The instrumental parameters were kept the same for all the experiments involving a particular metal complex.

2.3.3 ESI-MS spectrometry

ESI-MS spectra were recorded on a Waters (Micromass MS technologies) Q-TOF premier mass spectrometer. The samples were infused directly into the source at a speed of 10 μL/min using a syringe pump. The source voltage was maintained at 2 kV, and the capillary temperature was set to 353 K. Samples were prepared by dissolving pure solids either in HPLC grade or dry acetonitrile/methanol. The concentration of the solution was kept between 0.1 – 1.0 mM. For a room temperature unstable intermediate, measurements were performed by generating the intermediate in a liquid N_2 bath of the appropriate temperature and then immediately transferring the sample into the precooled syringe.

2.3.4 UV-Vis Spectroscopy

UV-Vis absorption spectra were recorded on a Hewlett-Packard 8453 spectrometer equipped with either a constant temperature circulating water bath or a liquid nitrogen cryostat (Unisoku) with a temperature controller. All the kinetics experiments were done using UV-Vis spectroscopy. The measurement of the decrease in absorbance for a substrate with time gives the reaction rate. In general, a 1 mM solution of a substrate was used for kinetics measurement. Test solutions were prepared in a dry or HPLC grade solvent depending upon the sensitivity of the reaction.

2.3.5 Kinetic studies

The reactivity of metal-peroxo complexes is a second-order reaction. Representation of the general reaction is as follows

$$Substrate + Peroxo \rightarrow Product$$

The second-order rate for the reaction is as follows –

$$Rate = k_2[Substrate][Peroxo]$$

When we add substrate in significant excess, the substrate consumed becomes negligible compared with the peroxo intermediate. The reaction, therefore, appears to follow first-order kinetics and is known as a pseudo-first-order reaction. Thus, we can express the rate as

$$Rate = k_{obs}[Peroxo]$$

Where $k_{obs} = k_2[Substrate]$

The second-order rate constant (k_2) was determined from the slope of the plot of pseudo-first-order (k_{obs}) rate constants against different substrate concentrations.

2.3.6 Product Analysis

All experiments were done at least in triplicate. Product analysis for 2-PPA and CCA deformylation was performed on WATERS ACQUITY UPLC equipped with a variable wavelength UV-200 detector. Products were separated on

Waters Symmetry C18 reverse-phase column (4.6 x 250 mm), and detection was made at 215 and 254 nm. Product yields were determined by comparison with standard curves of known authentic samples.

2.3.7 DFT Analysis

All DFT calculations were executed in the PARAM-ISHAN facility of IIT Guwahati using Gausian09 software.[12] The structure optimization calculations were done using the UB3LYP/BS1 method and solvent correction.

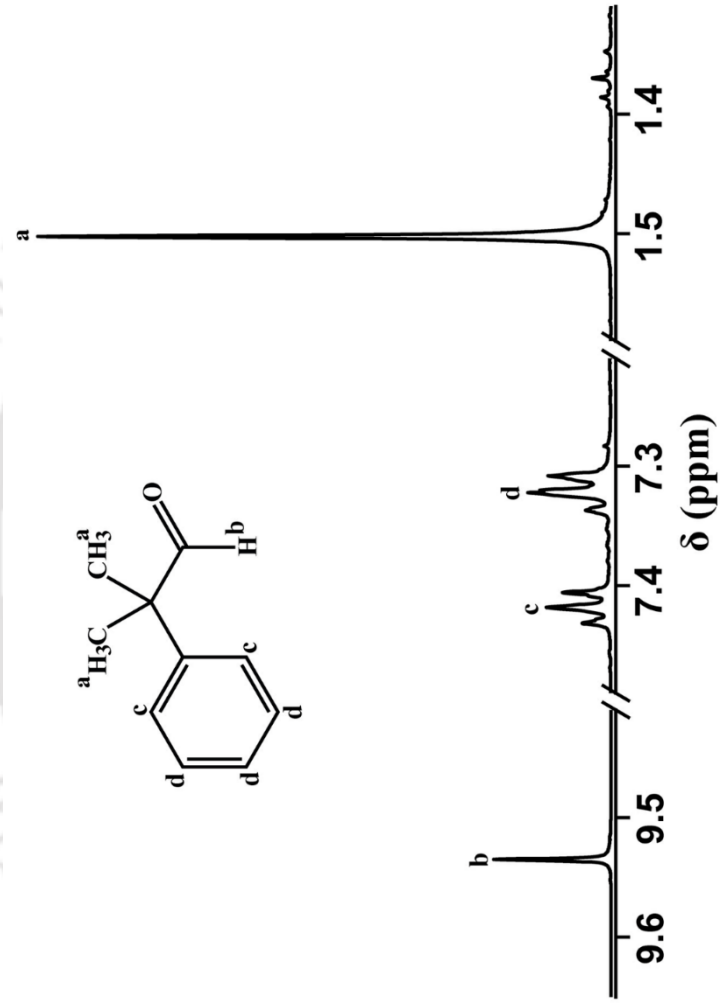

Figure 2.3 ^{1}H NMR spectra of 2-Me-2-PPA (at 600 MHz in $CDCl_3$).

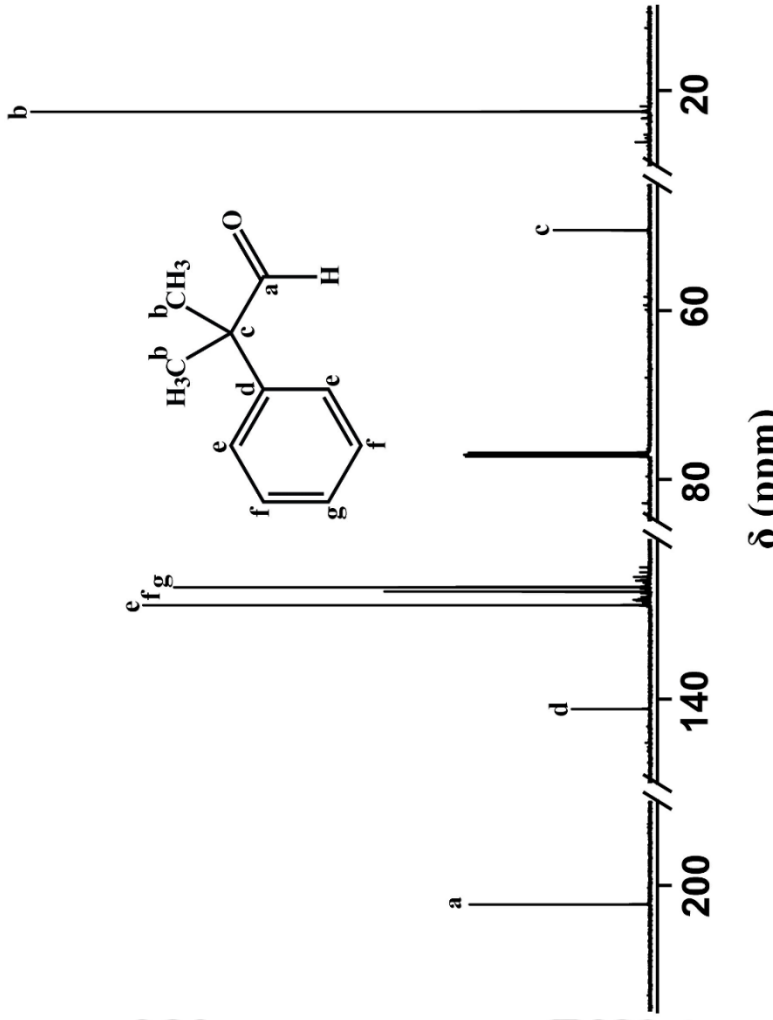

Figure 2.4 ^{13}C NMR spectra of 2-Me-2-PPA (at 150 MHz in $CDCl_3$).

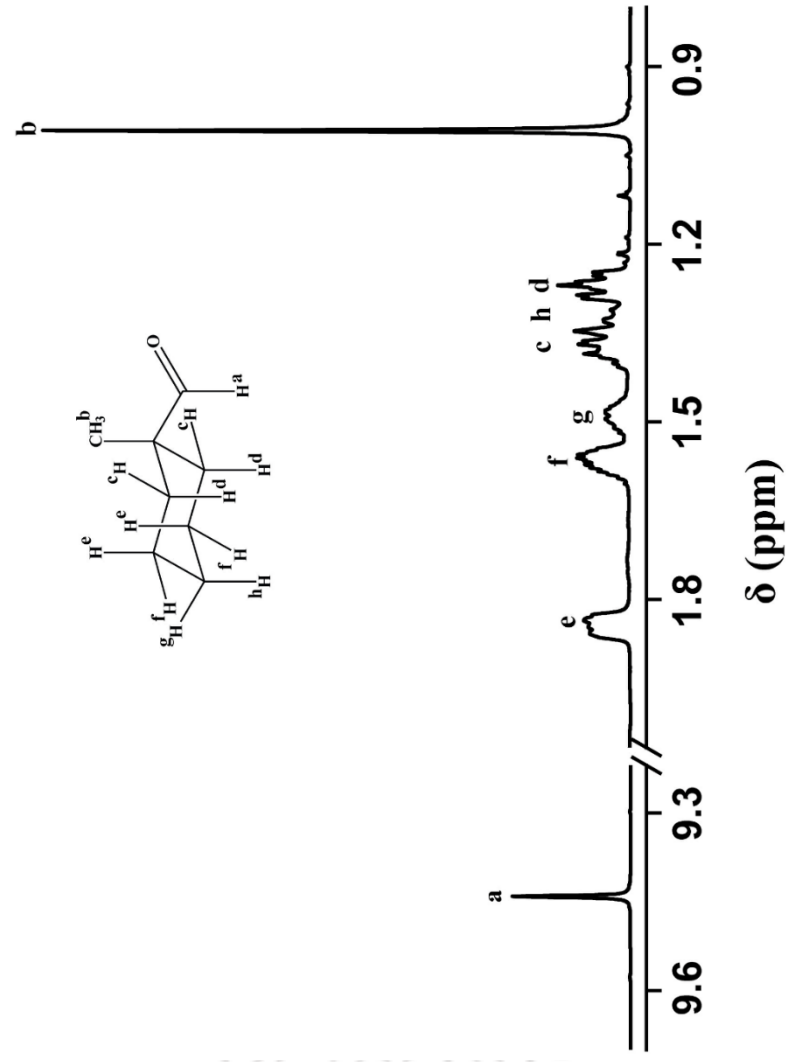

Figure 2.5 ^1H NMR spectra of 2-Me-CCA (at 600 MHz in $CDCl_3$).

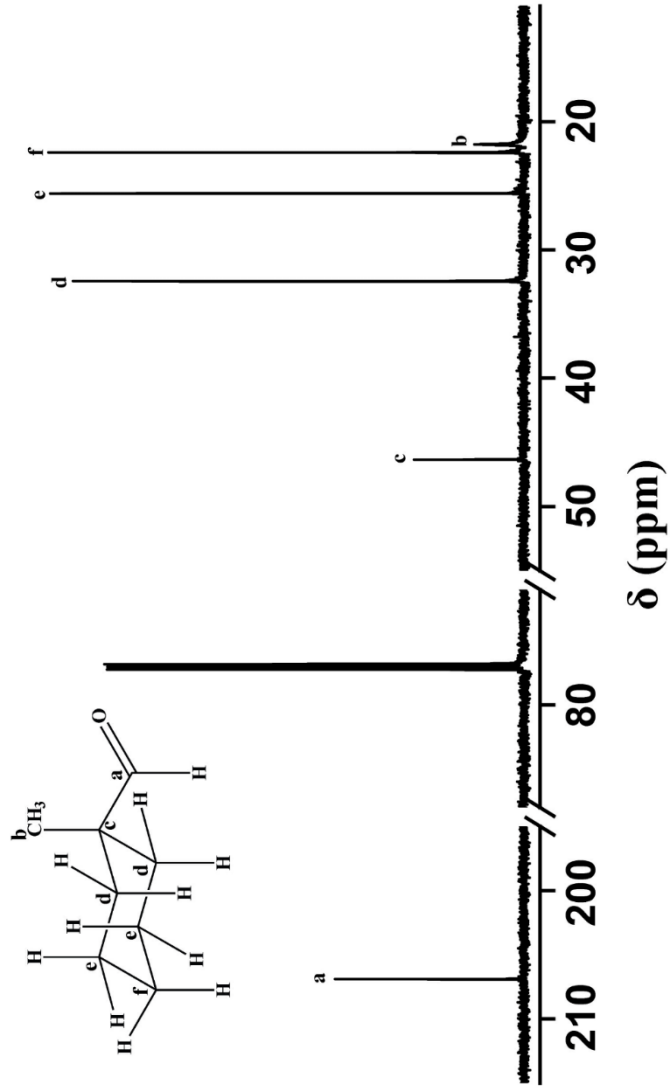

Figure 2.6 ^{13}C NMR spectra of 2-Me-CCA (at 150 MHz in $CDCl_3$).

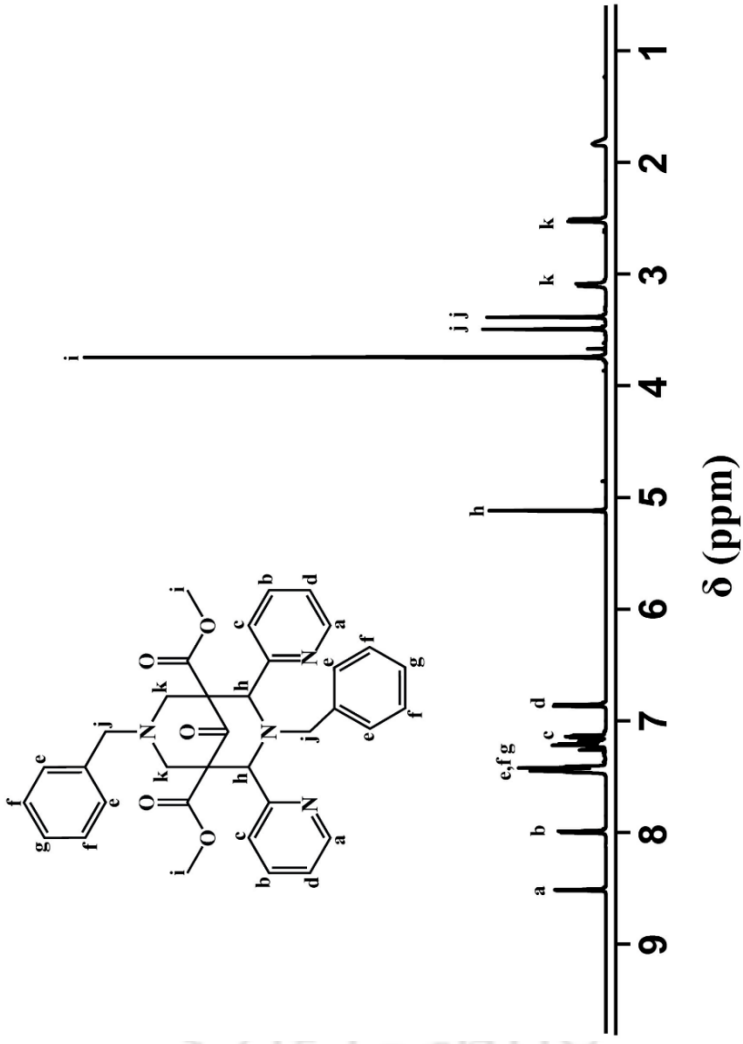

Figure 2.7 ^{1}H NMR spectra of BL2 (at 600 MHz in $CDCl_3$).

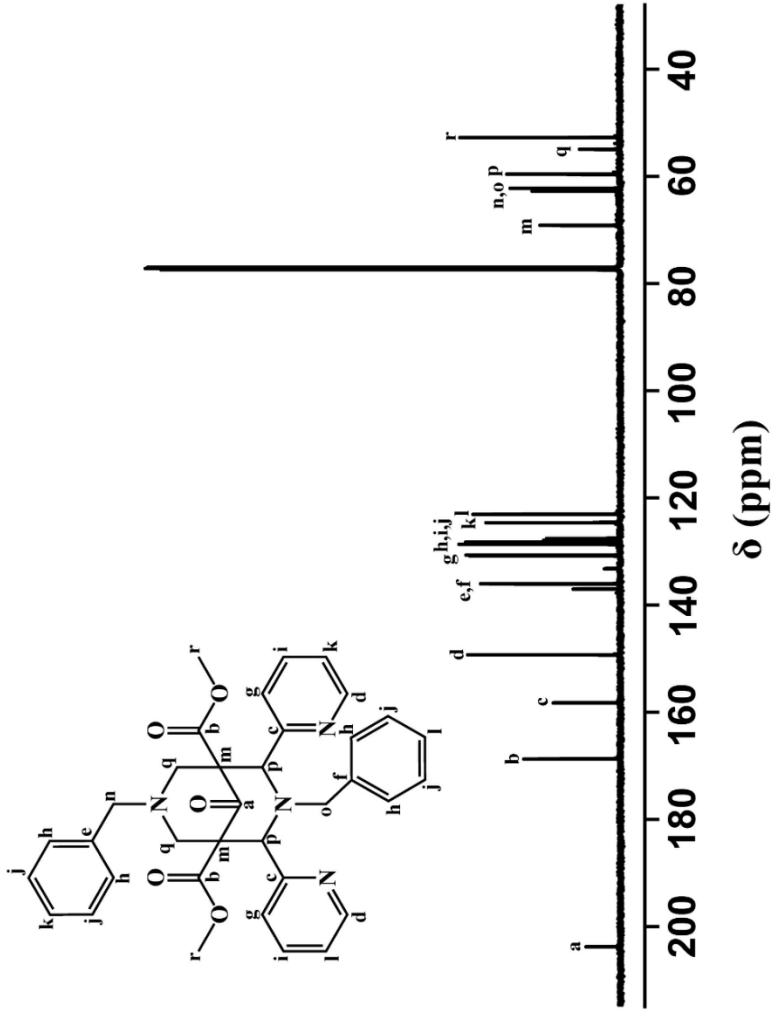

Figure 2.8 ^{13}C NMR spectra of BL2 (at 150 MHz in $CDCl_3$).

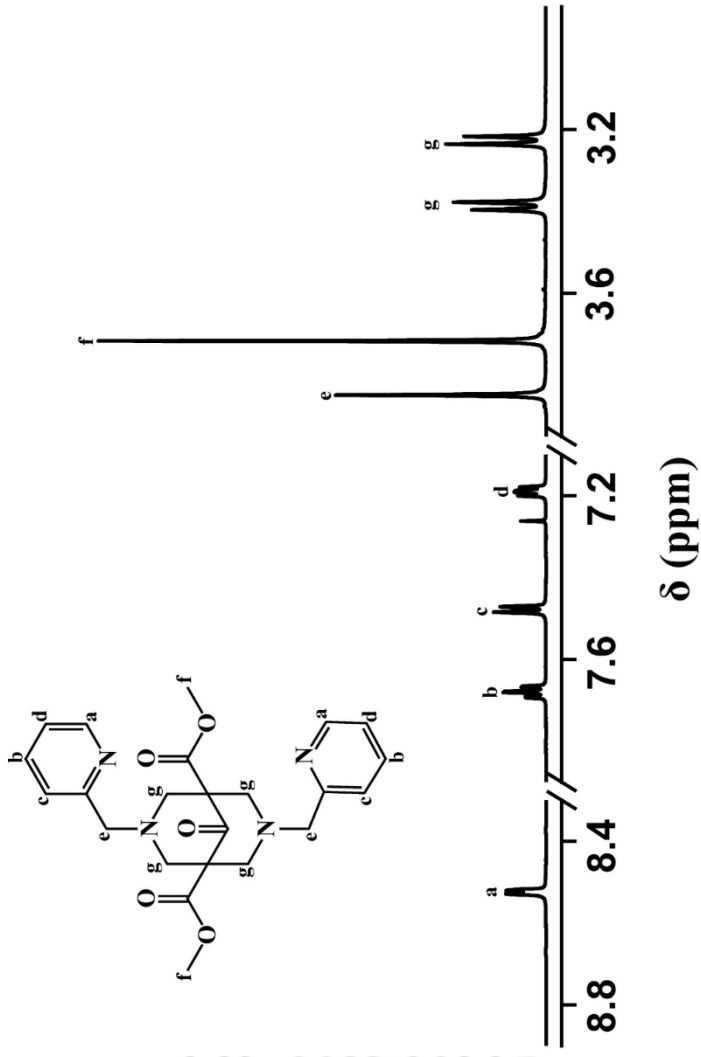

Figure 2.9 ^{1}H NMR spectra of BL3 (at 600 MHz in $CDCl_3$).

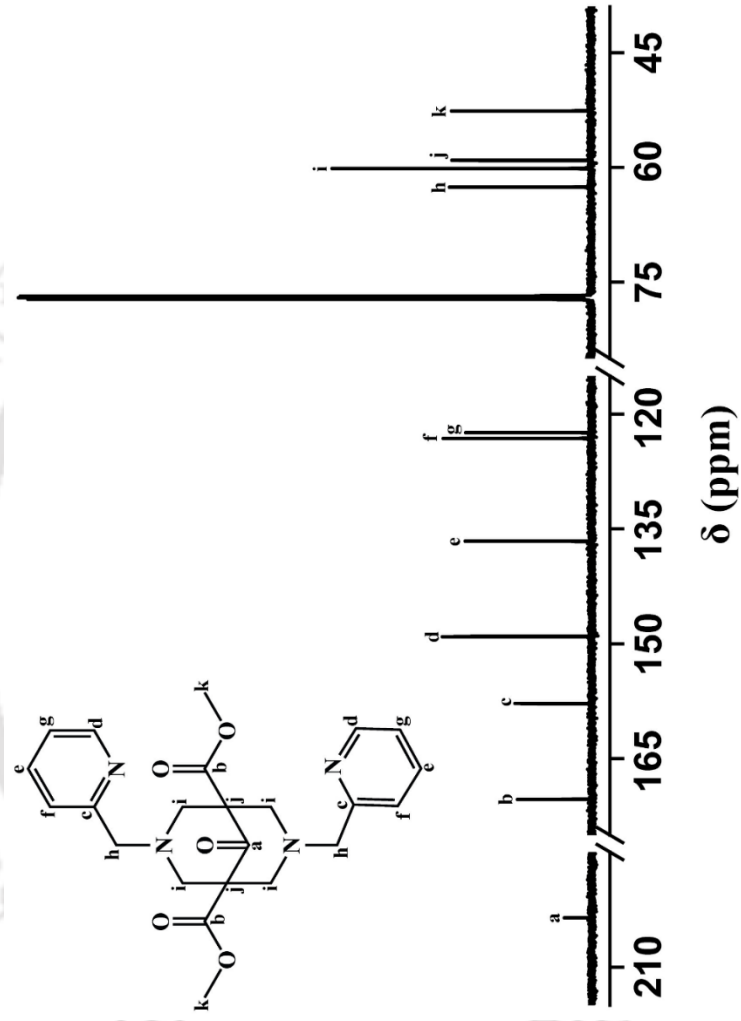

Figure 2.10 ^{13}C NMR spectra of BL3 (at 150 MHz in $CDCl_3$).

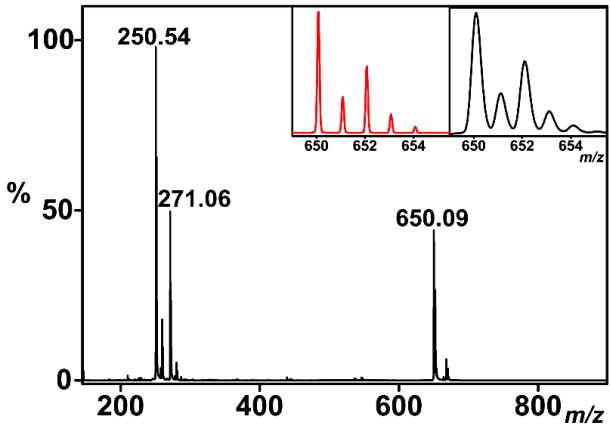

Figure 2.11 ESI-MS spectra of [Cu(BL1)(CH₃CN)](OTf) [inset red and black line shows simulated and experimental isotope distribution pattern respectively].

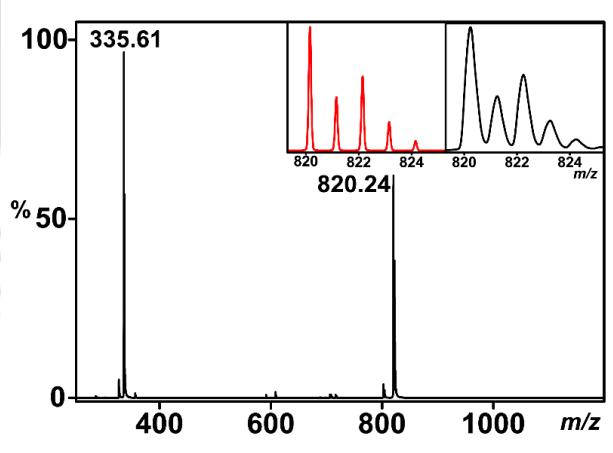

Figure 2.12 ESI-MS spectra of [Cu(BL2)(CH₃CN)](OTf)₂ [inset red and black line shows simulated and experimental isotope distribution pattern, respectively].

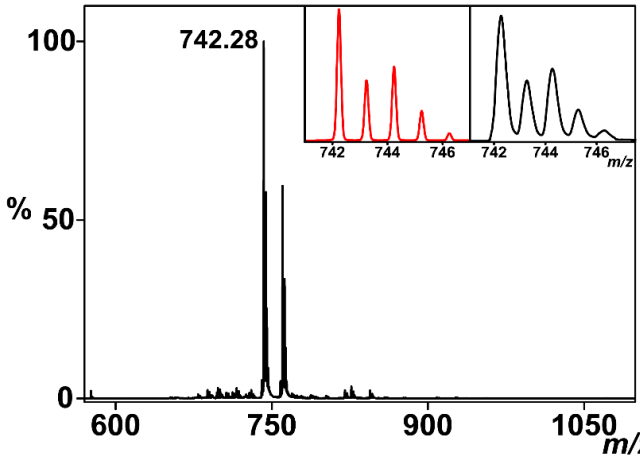

*Figure 2.13 ESI-MS spectra of [Cu(BL2)(OO^{t}Bu)]$^+$ (**2**) [inset red and black line shows simulated and experimental isotope distribution pattern, respectively].*

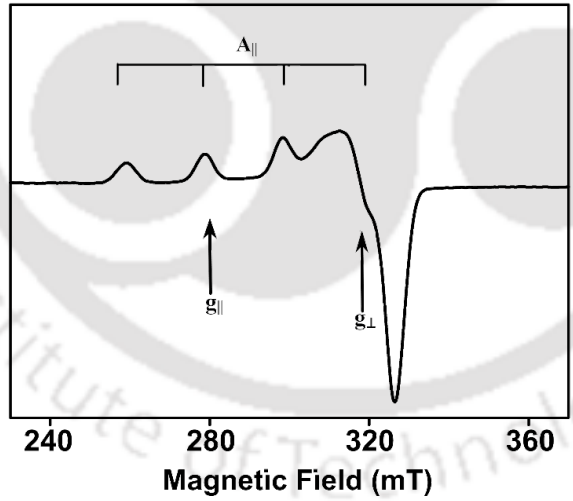

*Figure 2.14 EPR spectrum for [Cu(BL2)(OO^{t}Bu)]$^+$ (**2**) at 77 K in CH_3CN.*

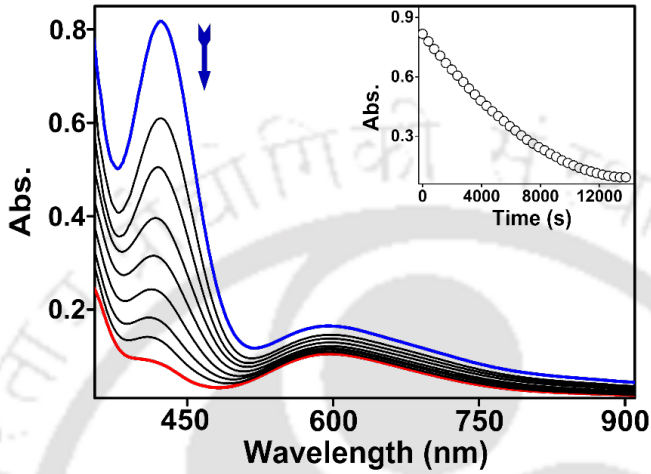

*Figure 2.15 Decay of **2** upon addition of 2-PPA (15 mM) in CH_3CN at 298 K [inset shows the time trace for the peak at 423 nm].*

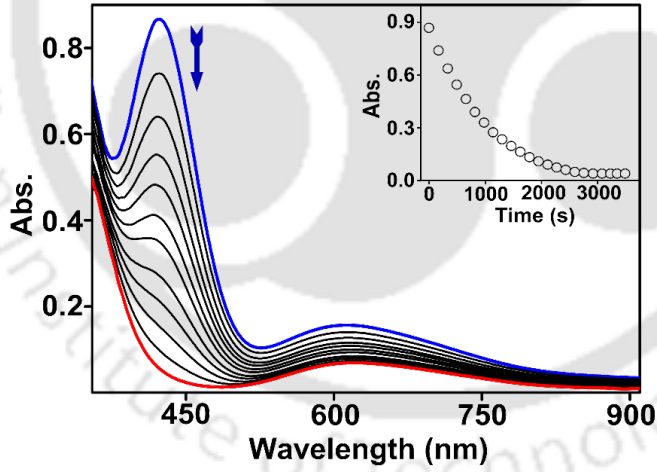

*Figure 2.16 Decay of $[Cu(BL1)(OO^tBu)]^+$ (**1**) upon addition of PPh_3 (80 mM) in CH_3CN at 298 K [inset shows the time trace for the peak at 423 nm].*

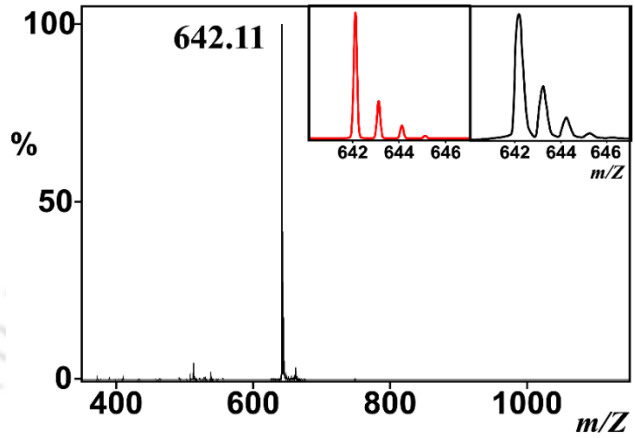

Figure 2.17 ESI-MS spectra of [Mn(BL3)](OTf)$_2$ [inset red and the black line shows simulated and experimental isotope distribution pattern, respectively].

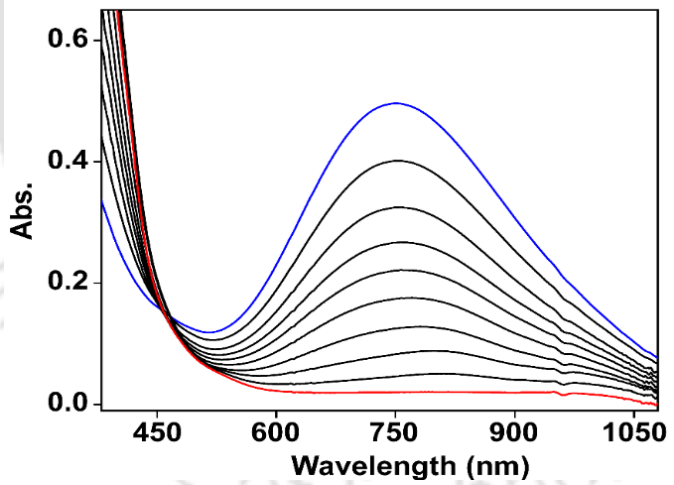

*Figure 2.18 Decay of [Fe(TMC)(O$_2$)]$^+$ (**4**) upon addition of CCA (100 mM) in TFE at 258 K.*

DFT optimized structure of 1

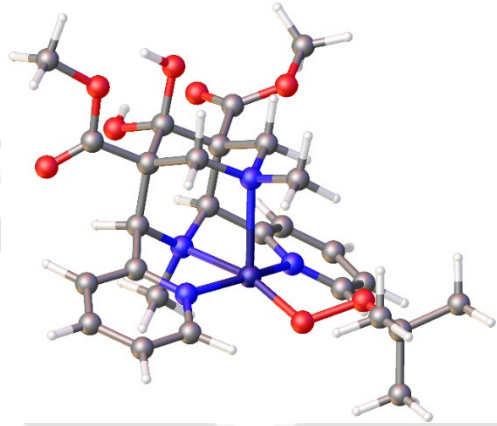

Figure 2.19 Optimized geometry of [Cu(BL1)(OO^{t}Bu)]$^+$ complex. Geometries optimized in Gaussian 09 at UB3LYP/BS1 with solvent included.

Cartesian Coordinate

Cu	1.233371000	-0.412577000	-0.492222000
N	1.491411000	1.596230000	-0.951544000
N	0.616484000	-2.351476000	-0.750362000
N	-0.093726000	-0.116576000	1.421871000
N	-0.549637000	-0.072257000	-1.500123000
C	-0.678777000	-2.466480000	-1.110716000

C	2.702067000	3.583698000	-1.502251000
C	0.344625000	2.182888000	-1.355752000
C	1.413001000	-3.429450000	-0.718673000
C	0.324023000	3.481518000	-1.855873000
C	2.646701000	2.276527000	-1.022727000
C	-1.208651000	-3.699564000	-1.486966000
C	1.523533000	4.193594000	-1.927494000
C	0.946840000	-4.694729000	-1.063567000
C	-0.300267000	-0.198079000	-2.965500000
C	-0.382825000	-4.825538000	-1.461312000
C	0.806762000	-0.313329000	2.572193000
C	-1.547492000	1.524807000	0.219715000
C	-0.915866000	1.342063000	-1.198179000
C	-0.581928000	1.273896000	1.399114000
C	-2.751766000	0.542688000	0.330295000

O	-1.534637000	3.744861000	1.139615000
O	-3.050288000	3.301637000	-0.463450000
C	-2.131102000	2.949324000	0.262853000
C	-1.488974000	-1.164430000	-1.083369000
C	-2.173322000	-0.911061000	0.302730000
C	-1.214051000	-1.073082000	1.502959000
O	-3.791190000	-2.581319000	-0.481387000
C	-3.370102000	-1.879103000	0.411760000
O	-3.937658000	-1.822001000	1.631890000
O	-3.369274000	0.870893000	1.547543000
O	-3.640920000	0.634457000	-0.748924000
C	-5.088903000	-2.680196000	1.842302000
C	-2.041636000	5.099695000	1.235909000
H	0.061954000	-1.201575000	-3.190509000
H	-1.222330000	-0.010658000	-3.529201000

H	1.166531000	-1.344867000	2.570380000
H	1.670994000	0.345432000	2.471631000
H	-1.665940000	1.681208000	-1.919740000
H	0.283738000	1.934491000	1.327906000
H	-1.107609000	1.518227000	2.331060000
H	-2.297639000	-1.236111000	-1.814038000
H	-0.797832000	-2.083402000	1.519954000
H	-1.778198000	-0.931560000	2.433316000
H	-4.002931000	0.165138000	1.774996000
H	-3.865019000	1.585252000	-0.841213000
H	-4.800761000	-3.722524000	1.697568000
H	-5.392855000	-2.499834000	2.871679000
H	-5.885593000	-2.412345000	1.146283000
H	-1.430752000	5.577612000	1.999356000
H	-1.932676000	5.606181000	0.275328000

H	-3.092071000	5.081269000	1.531282000
O	2.979959000	-0.970991000	0.000546000
O	3.638162000	0.056769000	0.812640000
C	4.879072000	-0.466761000	1.333417000
C	4.617643000	-1.676777000	2.239914000
H	3.935366000	-1.405246000	3.052879000
H	4.169415000	-2.494894000	1.670760000
H	5.554887000	-2.033705000	2.681642000
C	5.830557000	-0.825883000	0.183886000
H	6.005847000	0.048272000	-0.453751000
H	6.796368000	-1.164761000	0.575419000
H	5.406651000	-1.623685000	-0.431331000
C	5.428970000	0.712894000	2.146072000
H	6.386691000	0.439545000	2.601488000
H	5.590698000	1.586421000	1.505117000

H	4.734821000	0.991956000	2.946198000
H	0.293609000	-0.113052000	3.525849000
H	0.463217000	0.517451000	-3.271957000
H	1.533242000	5.206566000	-2.317006000
H	3.653460000	4.102108000	-1.544473000
H	3.520502000	1.744897000	-0.663787000
H	-0.609040000	3.923165000	-2.189806000
H	2.437358000	-3.242243000	-0.414130000
H	1.615958000	-5.547296000	-1.031273000
H	-0.777655000	-5.792947000	-1.755554000
H	-2.245633000	-3.771026000	-1.786230000

DFT optimized structure of 2

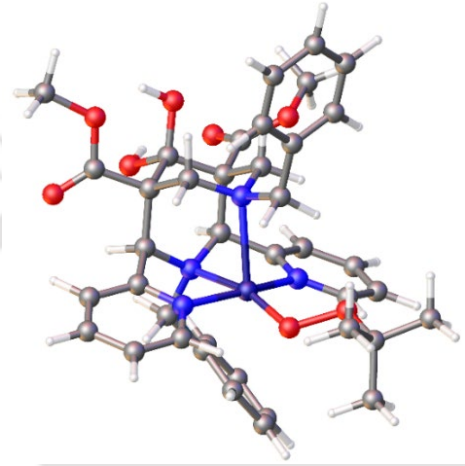

Figure 2.20 Optimized geometry of [Cu(BL2)(OO^{t}Bu)]$^+$ complex. Geometries optimized in Gaussian 09 at UB3LYP/BS1 with solvent included.

Cartesian Coordinates

Cu	1.092900000	0.444092000	0.532086000
N	1.807351000	-0.035532000	-1.336175000
N	0.536079000	0.278155000	2.496492000
N	-1.200811000	0.651093000	-0.136472000
N	0.647287000	-1.596131000	0.576574000
C	-0.095736000	-0.878100000	2.785896000

C	3.186460000	0.145926000	-3.280580000
C	1.403983000	-1.258439000	-1.734665000
C	0.864183000	1.138199000	3.471739000
C	1.864370000	-1.830057000	-2.917963000
C	2.684109000	0.652947000	-2.084446000
C	-0.384134000	-1.221981000	4.106049000
C	2.768345000	-1.114206000	-3.704334000
C	0.588828000	0.868955000	4.809132000
C	3.200985000	-2.037724000	0.726048000
C	1.794548000	-2.454631000	1.095960000
C	3.823336000	-0.988517000	1.420106000
C	-0.034461000	-0.336463000	5.127671000
C	5.254775000	-2.378361000	-0.527721000
C	3.936596000	-2.739075000	-0.237396000
C	5.856171000	-1.315886000	0.150332000

C	5.138894000	-0.624105000	1.130772000
C	-1.330533000	2.136101000	-0.236313000
C	-2.667287000	2.672097000	-0.718152000
C	-3.685504000	2.994453000	0.192339000
C	-4.915818000	3.485503000	-0.250218000
C	-4.136578000	3.366000000	-2.533709000
C	-2.907996000	2.875549000	-2.086054000
C	-5.145773000	3.668853000	-1.616076000
C	-1.076019000	-1.531994000	-1.329977000
C	0.362110000	-1.934215000	-0.855019000
C	-1.328207000	-0.011438000	-1.443597000
C	-2.099948000	-2.144715000	-0.331757000
O	-1.485214000	-1.410361000	-3.697423000
O	-1.319995000	-3.459421000	-2.782842000
C	-1.308997000	-2.240384000	-2.679009000

C	-0.468494000	-1.750661000	1.581804000
C	-1.898666000	-1.421600000	1.038304000
C	-2.150344000	0.089480000	0.838616000
O	-2.655929000	-2.769746000	2.946750000
C	-2.919763000	-2.029517000	2.024358000
O	-4.178790000	-1.671932000	1.706523000
O	-3.354943000	-1.900403000	-0.911699000
O	-1.890906000	-3.510027000	-0.092596000
C	-5.229065000	-2.204387000	2.554846000
C	-1.731671000	-2.014085000	-4.992335000
H	1.715194000	-2.430084000	2.184045000
H	1.602078000	-3.487121000	0.781867000
H	-1.102038000	2.523618000	0.760537000
H	-0.524241000	2.475819000	-0.891105000
H	0.431690000	-3.017905000	-0.983978000

H	-0.607201000	0.440870000	-2.126746000
H	-2.324415000	0.133485000	-1.874618000
H	-0.507953000	-2.793862000	1.900200000
H	-2.018261000	0.618407000	1.786156000
H	-3.187571000	0.236833000	0.520020000
H	-4.045667000	-2.068239000	-0.243918000
H	-1.840807000	-3.941057000	-0.972249000
H	-5.075818000	-1.869990000	3.581984000
H	-6.154017000	-1.800358000	2.147738000
H	-5.226179000	-3.294814000	2.512099000
H	-1.879336000	-1.176925000	-5.671919000
H	-0.869931000	-2.612543000	-5.293404000
H	-2.623472000	-2.641121000	-4.944805000
O	1.753346000	2.199656000	0.856864000
O	1.846346000	2.989104000	-0.373949000

C	2.266128000	4.333071000	-0.052139000
C	1.233446000	5.018688000	0.852305000
H	0.248954000	5.026299000	0.371582000
H	1.148638000	4.494435000	1.807461000
H	1.527481000	6.055596000	1.050867000
C	3.656312000	4.319873000	0.597530000
H	4.375629000	3.807320000	-0.051421000
H	4.011797000	5.343023000	0.764124000
H	3.628686000	3.802803000	1.560058000
C	2.314955000	5.008826000	-1.428791000
H	2.614892000	6.056547000	-1.320767000
H	3.038311000	4.510611000	-2.083476000
H	1.331519000	4.980434000	-1.910335000
H	3.481438000	-3.576045000	-0.760418000
H	5.811718000	-2.931911000	-1.278362000

H	6.882083000	-1.037086000	-0.073097000
H	5.606685000	0.188257000	1.679644000
H	3.283597000	-0.472629000	2.209664000
H	1.359449000	2.045614000	3.142926000
H	0.869652000	1.582864000	5.575316000
H	-0.247055000	-0.591330000	6.161174000
H	-0.879565000	-2.159116000	4.321423000
H	2.950560000	1.631639000	-1.702614000
H	3.891652000	0.731796000	-3.859446000
H	3.144693000	-1.541403000	-4.628413000
H	1.531093000	-2.820123000	-3.210818000
H	-2.121796000	2.660743000	-2.806005000
H	-4.302252000	3.518507000	-3.596773000
H	-6.101010000	4.053964000	-1.962224000
H	-5.690263000	3.731559000	0.471237000

H -3.509188000 2.872850000 1.258600000

DFT optimized structure of 3

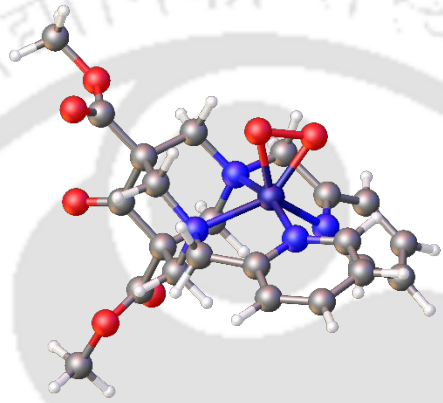

Figure 2.21 Optimized geometry of [Mn(BL3)(OO)]$^{+}$ complex. Geometries optimized in Gaussian 09 at UB3LYP/BS1 with solvent included.

Cartesian Coordinates

N -2.809261000 -1.334337000 0.797160000

N 0.030339000 -1.012471000 0.915992000

O 3.525872000 -1.343168000 -2.578152000

C 2.755214000 -0.172187000 0.143161000

O 2.896309000 -3.175475000 -1.361858000

C	0.840570000	-0.041944000	1.747951000
H	1.384130000	-0.597977000	2.518253000
H	0.136869000	0.633328000	2.242295000
C	1.914663000	-0.989759000	-0.839795000
C	-0.702088000	-1.913061000	1.895857000
H	-0.119131000	-2.823802000	2.067757000
H	-0.743646000	-1.378891000	2.851335000
C	-4.122352000	-1.538372000	0.522893000
H	-4.614280000	-0.779642000	-0.071937000
C	-4.797762000	-2.673393000	0.965356000
H	-5.847722000	-2.802870000	0.735533000
C	-2.733892000	-3.428186000	1.967438000
H	-2.160603000	-4.158432000	2.526009000
C	-4.088617000	-3.637475000	1.692119000
H	-4.581348000	-4.539632000	2.035278000

C	-2.121348000	-2.256019000	1.514764000
C	4.477870000	-2.162304000	-3.363669000
H	5.236265000	-2.577267000	-2.698549000
H	4.914463000	-1.466136000	-4.074670000
H	3.940431000	-2.963830000	-3.871732000
C	0.920003000	-1.840358000	0.014248000
H	0.285363000	-2.436737000	-0.641804000
H	1.515126000	-2.530093000	0.624676000
C	2.813204000	-1.965789000	-1.606066000
N	-2.054193000	1.938669000	-0.390618000
N	0.419211000	1.020863000	-1.108164000
O	3.102669000	0.907037000	2.993458000
O	3.074429000	2.789500000	1.692901000
C	1.256656000	0.021459000	-1.838022000
H	2.054024000	0.516782000	-2.404202000

H	0.611381000	-0.523602000	-2.528986000
C	1.871193000	0.790807000	0.939952000
C	-0.242214000	2.004280000	-2.025966000
H	0.476849000	2.734094000	-2.418624000
H	-0.659335000	1.441069000	-2.866795000
C	-3.075388000	2.477420000	0.318659000
H	-3.581627000	1.820982000	1.014615000
C	-3.453974000	3.808541000	0.155093000
H	-4.274274000	4.211185000	0.735005000
C	-1.691459000	4.043071000	-1.482301000
H	-1.123104000	4.638341000	-2.186329000
C	-2.753898000	4.600634000	-0.761550000
H	-3.023634000	5.639922000	-0.907229000
C	-1.360402000	2.703338000	-1.282041000
C	3.983852000	1.570023000	3.982760000

H	4.929883000	1.833400000	3.508373000
H	4.126300000	0.826609000	4.762381000
H	3.492981000	2.463260000	4.370919000
C	1.200521000	1.755195000	-0.068901000
H	0.525944000	2.422016000	0.472526000
H	1.974617000	2.374157000	-0.541500000
C	2.736000000	1.618237000	1.897921000
Mn	-1.493634000	-0.101918000	-0.457013000
O	-2.332271000	-0.323506000	-2.131239000
O	-1.421912000	-1.483008000	-1.761626000
O	3.979664000	-0.268226000	0.274446000

2.4 Reference

1. W. L. F. Armarego, in Purification of Laboratory Chemicals, (Ed: D. D.Perrin), Pergamon Press, Oxford, 1997
2. Dudnik, A. S.; Schwier, T.; Gevorgyan, V. Gold-Catalyzed Double Migration-Benzannulation Cascade toward Naphthalenes. Org. Lett. 2008, 10 (7), 1465–1468. https://doi.org/10.1021/ol800229h.
3. Ponath, S.; Menger, M.; Grothues, L.; Weber, M.; Lentz, D.; Strohmann, C.; Christmann, M. Mechanistic Studies on the Organocatalytic α-Chlorination of Aldehydes: The Role and Nature of Off-Cycle Intermediates. Angew. Chemie - Int. Ed. 2018, 57 (36), 11683–11687. https://doi.org/10.1002/anie.201806261.
4. Börzel, H.; Comba, P.; Hagen, K. S.; Lampeka, Y. D.; Lienke, A.; Linti, G.; Merz, M.; Pritzkow, H.; Tsymbal, L. V. Iron Coordination Chemistry with Tetra-, Penta- and Hexadentate Bispidine-Type Ligands. Inorganica Chim. Acta 2002, 337, 407–419. https://doi.org/10.1016/S0020-1693(02)01100-3.
5. Comba, P.; Kuwata, S.; Linti, G.; Pritzkow, H.; Tarnai, M.; Wadepohl, H. Oxidative N-Dealkylation in Cobalt-Bispidine-H2O2 Systems. Chem. Commun. 2006, 19, 2074–2076. https://doi.org/10.1039/b602571d.
6. Lubben, M.; Meetsma, A.; Wilkinson, E. C.; Feringa, B.; Que, L. Nonheme Iron Centers in Oxygen Activation: Characterization of an

Iron(III) Hydroperoxide Intermediate. Angew. Chemie Int. Ed. 1995, 34 (13–14), 1512–1514. https://doi.org/10.1002/anie.199515121.

7. Vardhaman, A. K.; Sastri, C. V.; Kumar, D.; De Visser, S. P. Nonheme Ferric Hydroperoxo Intermediates Are Efficient Oxidants of Bromide Oxidation. Chem. Commun. 2011, 47 (39), 11044–11046. https://doi.org/10.1039/c1cc13775a.
8. Gogoll, A.; Grennberg, H.; Axén, A. (π-Allyl)palladium Complexes with N,N'-Diphenylbispidinone Derivatives as a New Type of Chelating Nitrogen Ligand: Complexation Studies, Spectroscopic Properties, and an X-ray Structure of (3,7-Diphenyl-1,5-dimethylbispidinone)[(1,3-η^3-propenyl)- palladium] Trifluoromethanesulfonate Organometallics 1997, 16 (6), 1167–1178. https://doi.org/10.1021/om9609527.
9. Annaraj, J.; Suh, Y.; Seo, M. S.; Kim, S. O.; Nam, W. Mononuclear Nonheme Ferric-Peroxo Complex in Aldehyde Deformylation. Chem. Commun. 2005, 36, 4529–4531. https://doi.org/10.1039/b505562h.
10. Ho, R. Y. N.; Roelfes, G.; Hermant, R.; Hage, R.; Feringa, B. L.; Que, L. Resonance Raman Evidence for the Interconversion between an $[Fe^{III}$-η^1-$OOH]^{2+}$ and $[Fe^{III}$-η^2-$O_2]^+$ Species and Mechanistic Implications Thereof. Chem. Commun. 1999, 21, 2161–2162. https://doi.org/10.1039/A905535E.
11. Comba, P.; Kanellakopulos, B.; Katsichtis, C.; Lienke, A.; Pritzkow, H.; Rominger, F. Synthesis and Characterisation of Manganese(II)

Compounds with Tetradentate Ligands Based on the Bispidine Backbone. J. Chem. Soc. Dalt. Trans. 1998, 23, 3997–4002. https://doi.org/10.1039/A805944F.

12. M.J. Frisch, G.W. Trucks, H.B. Schlegel, G.E. Scuseria, M.A. Robb, J.R. Cheeseman, G. Scalmani, V. Barone, B. Mennucci, G.A. Petersson, H. Nakatsuji, M. Caricato, X. Li, H.P. Hratchian, A.F. Izmaylov, J. Bloino, G. Zheng, J.L. Sonnenberg, M. Hada, M. Ehara, K. Toyota, R. Fukuda, J. Hasegawa, M. Ishida, T. Nakajima, Y. Honda, O. Kitao, H. Nakai, T. Vreven, J.A. Montgomery Jr, J.E. Peralta, F. Ogliaro, M. Bearpark, J.J. Heyd, E. Brothers, K.N. Kudin, V.N. Staroverov, T. Keith, R. Kobayashi, J. Normand, K. Raghavachari, A. Rendell, J.C. Burant, S.S. Iyengar, J. Tomasi, M. Cossi, N. Rega, J.M. Millam, M. Klene, J.E. Knox, J.B. Cross, V. Bakken, C. Adamo, J. Jaramillo, R. Gomperts, R.E. Stratmann, O. Yazyev, A.J. Austin, R. Cammi, C. Pomelli, J.W. Ochterski, R.L. Martin, K. Morokuma, V.G. Zakrzewski, G.A. Voth, P. Salvador, J.J. Dannenberg, S. Dapprich, A.D. Daniels, O. Farkas, J.B. Foresman, J.V. Ortiz, J. Cioslowski, D.J. Fox, Gaussian 09, Revision D.01, Gaussian Inc., Wallingford, CT, 2013.

Chapter 3: Influence of induced steric on the deformylation of aldehyde by Cu(II)-alkylperoxo intermediates

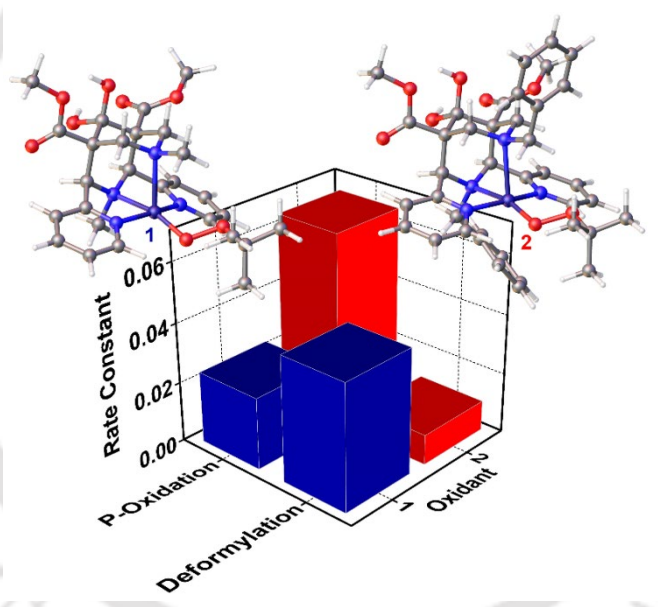

3.1 Introduction

In the past few years, various Cu(II)–oxygen intermediates have been characterized and served as models for a different biological reaction type.[1-10] Mononuclear transition metal alkylperoxo complexes are imperative in an assorted biological and catalytic oxidation reaction.[11-13] Mononuclear Cu(II)-OOR intermediates have been used as a model system to understand the reactivity of non-coupled binuclear copper enzymes, Dopamine β-monooxygenase (DβM), and Peptidyglycine α-hydroxylating monooxygenase (PHM).[14-17] DβM performs dopamine's conversion to norepinephrine by an oxygen insertion mechanism. In contrast, PHM catalyzes the stereospecific hydroxylation of the glycine α-carbon of peptidyl glycine substrate by a mechanism similar to DβM. The DβM reaction is supposed to proceed via an H-atom abstraction from the substrate by Cu(II)-hydroperoxo species. Several reports are available on the deformylation of aldehydes by Cu(II)-alkylperoxo intermediate,[18-25,] but detail mechanistic studies have been performed in very few cases. Although Cu(II)-alkylperoxo species are generally known to be electrophilic, some reports suggest otherwise for aldehyde deformylation.[26] Recent developments in the deformylation reaction mechanism of Mn(III)-peroxo systems suggest an initial H-atom abstraction mechanism. These studies make us think about the possibility of a similar pathway for the deformylation reaction for the Cu(II)-alkylperoxo system, which inspires us to perform isotope labeling experiments for the deformylation by Cu(II)-alkylperoxo species to get more details about the mechanism. Bispidine ligands have been

extensively used in biomimetic chemistry to understand the reactivity of various metal-oxygen intermediates.[27-35] Due to their very rigid adamantane type backbone, these ligands enforce the metal center to adapt a square-pyramidal geometry.[36] It is a known fact that substituents at N3 and N7 positions of bispidine ligands play an essential role in the intermediates' reactivity for Fe and Mn-based systems. This chapter has studied the mechanism of aldehyde deformylation by two Cu(II)-alkylperoxo species and the effect of ligand architecture on the reactivity (Figure 3.1).

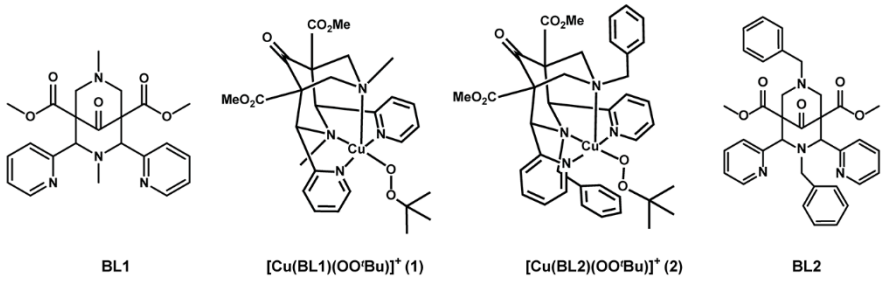

Figure 3.1 Molecular structure of the ligands and Cu(II)-alkylperoxo complexes studied in this work.

3.2 Experimental Section

Alkylperoxo complexes [Cu(BL1)(OO^{t}Bu)]$^+$ (**1**) and [Cu(BL2)(OO^{t}Bu)]$^+$ (**2**) were generated from their Cu(II) precursors (1a and 2a respectively, Sec 2.2.4.2), using tert-Butyl hydroperoxide (^{t}BuOOH) and triethylamine (TEA) in acetonitrile at 298 K. The addition of 10 equivalents of ^{t}BuOOH to an acetonitrile solution (1 mM) of the Cu(II)-triflate in the presence of 2.5

equivalents of TEA resulted in the formation of a green color solution of the alkylperoxo complexes.

3.3 Result and Discussion

Various spectroscopic techniques characterized intermediates **1** and **2**. Both the intermediates persisted for ten days at ambient temperature.

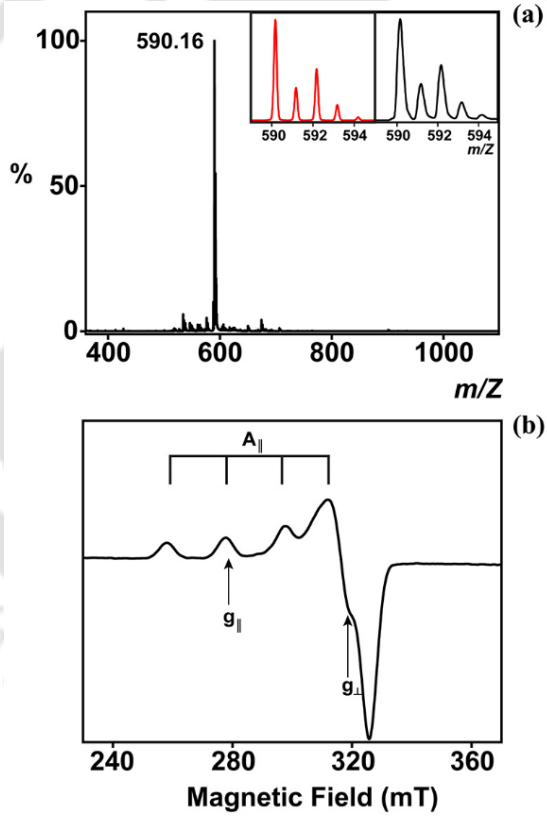

*Figure 3.2 (a) ESI-MS spectrum of **1** [inset red and the black line shows simulated and experimental isotopic distribution]. (b) EPR spectrum for **1** at 77 K in CH_3CN.*

Complex **1** exhibits absorption spectra with an intense charge transfer band (LMCT) at 423 nm ($\varepsilon \approx 860\ M^{-1}\ cm^{-1}$), with a weak band at 610 nm ($\varepsilon \approx 150\ M^{-1}\ cm^{-1}$) for d-d absorption. Similarly, complex **2** has electronic transitions at 423 nm ($\varepsilon \approx 810\ M^{-1}\ cm^{-1}$) and 595 nm ($\varepsilon \approx 155\ M^{-1}\ cm^{-1}$). The UV-Vis features observed for **1** and **2** are similar to previously reported Cu(II)-alkylperoxo complexes. A blue shift of 15 nm was observed in d-d transitions replacing methyl with the benzyl group at the N3 and N7 positions. However, no such shift has been observed in the charge transfer band. These results demonstrate that introduction of the steric bulk results in perturbation around the metal center. The electrospray ionisation mass spectra (ESI-MS) of **1** and **2** exhibit prominent peaks for $[Cu(BL1)(OO^tBu)]^+$ and $[Cu(BL2)(OO^tBu)]^+$ at *m/z* = 590.16 (calcd. 590.18) (Figure 3.2) and 742.28 (calcd. 742.24) (Figure 2.13) respectively. The X-band EPR spectrum of a frozen CH_3CN solution of **1** and **2** measured at 77 K shows an axial signal with $g_\perp$ = 2.065 and $g_\parallel$ = 2.360 ($A_\parallel$ = 199 G) (Figure 3.2) and $g_\perp$ = 2.055 and $g_\parallel$ = 2.351 ($A_\parallel$ = 196 G) (Figure 2.14), respectively.

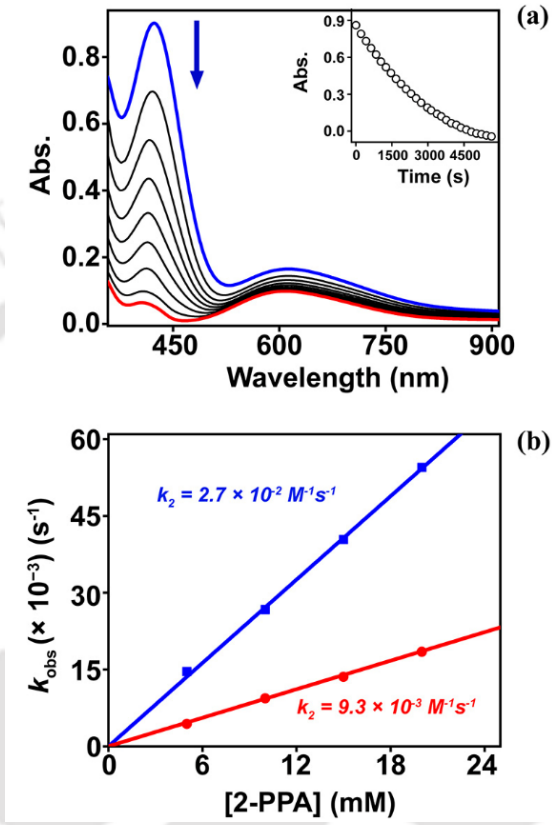

*Figure 3.3 [a] Decay of 1 upon addition of 2-PPA (15 mM) in CH_3CN at 298 K [inset shows the time trace for the peak at 423 nm]. [b] Plot of k_{obs} against the concentration of 2-PPA and the second-order rate constant for the reaction of 2-PPA with **1** (■) and **2** (●).*

These values suggest a square pyramidal geometry for the Cu(II) ion as per previously reported results. We have used 2-Phenylpropionaldehyde (2-PPA) as a model substrate for the aldehyde deformylation reaction. To an acetonitrile (1 mM) solution of intermediate, 10 Equiv. of 2-PPA has been added at 298 K. The electronic absorption band for the

intermediates started to decay immediately after the addition of the substrate (Figure 3.3).

The decrement in absorbance with time gives a pseudo-first-order (k_{obs}) rate for the reaction. The k_{obs} values increased proportionally with an increase of the 2-PPA concentration, allowing us to measure the second-order rate constant with **1** and **2** of 2.7×10^{-2} M^{-1} s^{-1} and 9.3×10^{-3} M^{-1} s^{-1}, respectively. The deformylation of aldehydes by Cu(II)-alkylperoxo complexes have been reported to proceed via the nucleophilic pathway by the attack at the carbonyl center[75]. However, recently it has been demonstrated that the deformylation reaction continues via an initial hydrogen atom abstraction followed by keto-enol tautomerism in the case of Mn(III)-peroxo intermediates.[37,38]

Thus to investigate the plausible pathway for the deformylation of 2-PPA to acetophenone, we have employed α-[D1]-2-phenylpropionaldehyde (α-[D1]-PPA) as a mechanical probe. Thus, upon adding α-[D1]-PPA to **1** and **2** in CH_3CN at 298 K, we have observed a second-order rate constant of 2.2×10^{-3} M^{-1} s^{-1} and 1.2×10^{-3} M^{-1} s^{-1} respectively (Figure 3.4).

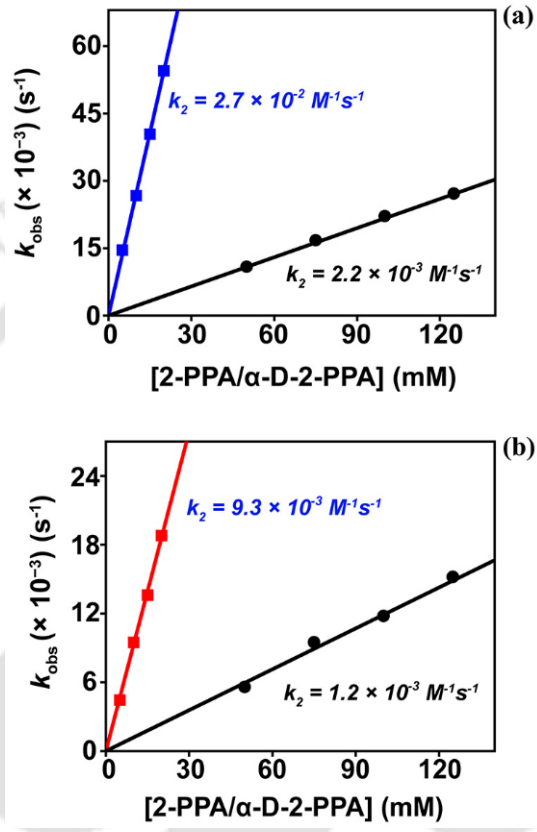

Figure 3.4 The plot of kobs against the concentration of α-[D]-2-PPA (●) *and 2-PPA with **1*** (■) *(a) and 2* (■) *(b).*

Therefore, our kinetics studies establish that the Cu(II)-alkylperoxo complex **1** and **2** also react with 2-PPA via an initial hydrogen atom abstraction reaction from the α-position of the aldehyde, with a KIE of 12 and 8, respectively. The experimental results are suggestive of the fact that intermediate **1** reacts at a faster rate than **2**.

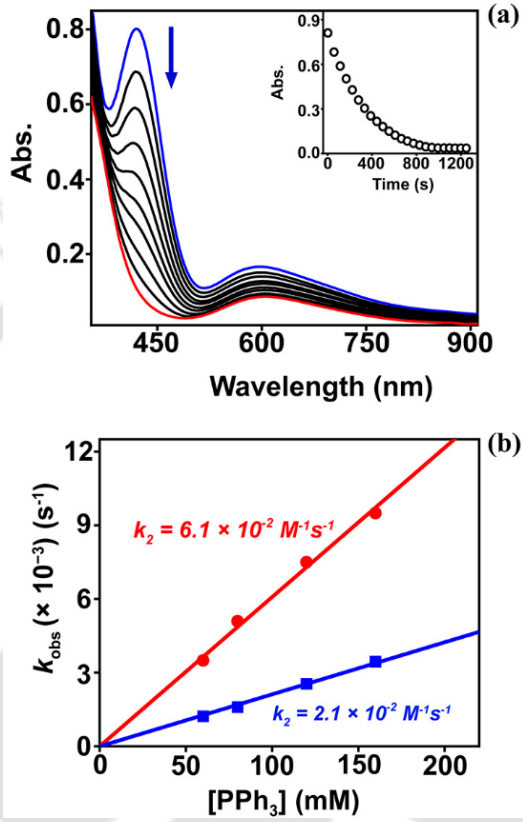

*Figure 3.5 [a] Decay of **2** upon addition of PPh_3 (80 mM) in CH_3CN at 298 K [inset shows the time trace for the peak at 423 nm]. [b] Plot of k_{obs} against the different concentrations of PPh_3 and for the reaction of PPh_3 with **1** (■) and **2** (●).*

To investigate the ligand architecture effect, we have decided to check the reactivity with other known electrophilic reactions like oxygen atom transfer to a heteroatom. Upon adding 80 Equiv. PPh_3 to an acetonitrile solution (1 mM) of intermediate at 298 K, the LMCT absorption band at 423 nm decayed immediately (Figure 3.5). The k_{obs} values increased

linearly with increasing PPh_3 concentration, giving a k_2 value of 2.1 × 10^{-2} M^{-1} s^{-1} and 6.1 × 10^{-2} M^{-1} s^{-1} with **1** and **2**, respectively. Therefore, it appears that **2** reacts with PPh_3 about three times faster than **1**. The above experimental results suggest a switchover of the reactivity order for the oxygen atom transfer reaction.

3.4 Conclusions

We have demonstrated the synthesis, characterization, and reactivity of two bispidine Cu(II)-alkylperoxo complexes. Unlike the previously reported nucleophilic reactivity for aldehyde deformylation, the Cu-alkylperoxo species reacts via C-H abstraction from the α-position. This inference has been extracted from the KIE values above the classical limit of 7, imperative of rate-determining C-H bond cleavage. These complexes have also exhibited oxygen atom transfer to heteroatoms. It was also observed that these two complexes show an inverse trend in reactivity for the two different types of electrophilic reactions. The introduction of two benzyl groups instead of methyl groups at the N3 and N7 positions increases the steric bulk around the metal center, accelerating atom transfer to heteroatoms. At the same time, the same phenomenon decreases reaction rates for aldehyde deformylation reactions.

3.5 References

1. Jasniewski, A. J.; Que, L. Dioxygen Activation by Nonheme Diiron Enzymes: Diverse Dioxygen Adducts, High-Valent Intermediates, and Related Model Complexes. Chem. Rev. 2018, 118 (5), 2554–2592. https://doi.org/10.1021/acs.chemrev.7b00457.
2. Karlin, K. D.; Kaderli, S.; Zuberbühler, A. D. Kinetics and Thermodynamics of Copper(I)/Dioxygen Interaction. Acc. Chem. Res. 1997, 30 (3), 139–147. https://doi.org/10.1021/ar950257f.
3. Himes, R. A.; Karlin, K. D. Copper-Dioxygen Complex Mediated C-H Bond Oxygenation: Relevance for Particulate Methane Monooxygenase (PMMO). Curr. Opin. Chem. Biol. 2009, 13 (1), 119–131. https://doi.org/10.1016/j.cbpa.2009.02.025.
4. Kamachi, T.; Lee, Y. M.; Nishimi, T.; Cho, J.; Yoshizawa, K.; Nam, W. Combined Experimental and Theoretical Approach to Understand the Reactivity of a Mononuclear Cu(II)-Hydroperoxo Complex in Oxygenation Reactions. Journal of Physical Chemistry A. 2008, pp 13102–13108. https://doi.org/10.1021/jp804804j.
5. Solomon, E. I.; Chen, P.; Metz, M.; Lee, S. K.; Palmer, A. E. Oxygen Binding, Activation, and Reduction to Water by Copper Proteins. Angew. Chemie - Int. Ed. 2001, 40 (24), 4570–4590.

https://doi.org/10.1002/1521-3773(20011217)40:24<4570::AID-ANIE4570>3.0.CO;2-4.

6. Tano, T.; Mieda, K.; Sugimoto, H.; Ogura, T.; Itoh, S. A Copper Complex Supported by an N2S-Tridentate Ligand Inducing Efficient Heterolytic O-O Bond Cleavage of Alkylhydroperoxide. Dalt. Trans. 2014, 43 (12), 4871–4877. https://doi.org/10.1039/c3dt52952e.
7. Suzuki, M. Ligand Effects on Dioxygen Activation by Copper and Nickel Complexes: Reactivity and Intermediates. Acc. Chem. Res. 2007, 40 (7), 609–617. https://doi.org/10.1021/ar600048g.
8. Itoh, S. Developing Mononuclear Copper-Active-Oxygen Complexes Relevant to Reactive Intermediates of Biological Oxidation Reactions. Acc. Chem. Res. 2015, 48 (7), 2066–2074. https://doi.org/10.1021/acs.accounts.5b00140.
9. Liu, J. J.; Diaz, D. E.; Quist, D. A.; Karlin, K. D. Copper(I)-Dioxygen Adducts and Copper Enzyme Mechanisms. Israel Journal of Chemistry. 2016, pp 738–755. https://doi.org/10.1002/ijch.201600025.
10. Lee, J. Y.; Karlin, K. D. Elaboration of Copper-Oxygen Mediated CH Activation Chemistry in Consideration of Future Fuel and Feedstock Generation. Curr. Opin. Chem. Biol. 2015, 25, 184–193. https://doi.org/10.1016/j.cbpa.2015.02.014.

11. Kovaleva, E. G.; Lipscomb, J. D. Crystal Structures of Fe^{2+} Dioxygenase Superoxo, Alkylperoxo, and Bound Product Intermediates. Science . 2007, 316 (5823), 453–457. https://doi.org/10.1126/science.1134697.

12. Chavez, F. A.; Mascharak, P. K. Co(III) - Alkylperoxo Complexes: Syntheses, Structure - Reactivity Correlations, and Use in the Oxidation of Hydrocarbons. Acc. Chem. Res. 2000, 33 (8), 539–545. https://doi.org/10.1021/ar990089h.

13. Yokoyama, K.; Uhlin, U.; Stubbe, J. A Hot Oxidant, 3-NO_2Y_{122} Radical, Unmasks Conformational Gating in Ribonucleotide Reductase. J. Am. Chem. Soc. 2010, 132 (43), 15368–15379. https://doi.org/10.1021/ja1069344.

14. Lehnert, N.; Ho, R. Y. N.; Que, L.; Solomon, E. I. Spectroscopic Properties and Electronic Structure of Low-Spin FE(III)-Alkylperoxo Complexes: Homolytic Cleavage of the O-O Bond. J. Am. Chem. Soc. 2001, 123 (34), 8271–8290. https://doi.org/10.1021/ja010165n.

15. Prigge, S. T.; Kolhekar, A. S.; Eipper, B. A.; Mains, R. E.; Amzel, L. M. Amidation of Bioactive Peptides: The Structure of Peptidylglycine α-Hydroxylating Monooxygenase. Science. 1997, 278 (5341), 1300 – 1305. https://doi.org/10.1126/science.278.5341.1300.

16. Klinman, J. P. The Copper-Enzyme Family of Dopamine β-Monooxygenase and Peptidylglycine α-Hydroxylating Monooxygenase:

Resolving the Chemical Pathway for Substrate Hydroxylation. J. Biol. Chem. 2006, 281 (6), 3013–3016. https://doi.org/10.1074/jbc.R500011200.

17. Kitajima, N.; Katayama, T.; Fujisawa, K.; Iwata, Y.; Moro-oka, Y. Synthesis, Molecular Structure, and Reactivity of (Aikylperoxo)Copper(II) Complex. J. Am. Chem. Soc. 1993, 115 (17), 7872–7873. https://doi.org/10.1021/ja00070a041.
18. Elwell, C. E.; Gagnon, N. L.; Neisen, B. D.; Dhar, D.; Spaeth, A. D.; Yee, G. M.; Tolman, W. B. Copper-Oxygen Complexes Revisited: Structures, Spectroscopy, and Reactivity. Chem. Rev. 2017, 117 (3), 2059–2107. https://doi.org/10.1021/acs.chemrev.6b00636.
19. Kunishita, A.; Teraoka, J.; Scanlon, J. D.; Matsumoto, T.; Suzuki, M.; Cramer, C. J.; Itoh, S. Aromatic Hydroxylation Reactivity of a Mononuclear Cu(II)-Alkylperoxo Complex. Journal of the American Chemical Society. 2007, 7248–7249. https://doi.org/10.1021/ja071623g.
20. Kunishita, A.; Ishimaru, H.; Nakashima, S.; Ogura, T.; Itoh, S. Reactivity of Mononuclear Alkylperoxo Copper(II) Complex. O-O Bond Cleavage and C-H Bond Activation. Journal of the American Chemical Society. 2008, 4244–4245. https://doi.org/10.1021/ja800443s.
21. Choi, Y. J.; Cho, K. Bin; Kubo, M.; Ogura, T.; Karlin, K. D.; Cho, J.; Nam, W. Spectroscopic and Computational Characterization of Cu^{II}-OOR (R = H or Cumyl) Complexes Bearing a Me6-Tren Ligand. Dalt. Trans. 2011, 40 (10), 2234–2241. https://doi.org/10.1039/c0dt01036g.

22. Paria, S.; Ohta, T.; Morimoto, Y.; Ogura, T.; Sugimoto, H.; Fujieda, N.; Goto, K.; Asano, K.; Suzuki, T.; Itoh, S. Generation, Characterization, and Reactivity of a CuII-Alkylperoxide/Anilino Radical Complex: Insight into the O-O Bond Cleavage Mechanism. J. Am. Chem. Soc. 2015, 137 (34), 10870–10873. https://doi.org/10.1021/jacs.5b04104.

23. Tano, T.; Ertem, M. Z.; Yamaguchi, S.; Kunishita, A.; Sugimoto, H.; Fujieda, N.; Ogura, T.; Cramer, C. J.; Itoh, S. Reactivity of Copper(II)-Alkylperoxo Complexes. Dalt. Trans. 2011, 40 (40), 10326-10336. https://doi.org/10.1039/c1dt10656b.

24. Abe, T.; Morimoto, Y.; Mieda, K.; Sugimoto, H.; Fujieda, N.; Ogura, T.; Itoh, S. Geometric effects on O-O bond scission of copper(II)-alkylperoxide complexes. 2017, 177, 375–383. https://doi.org/10.1016/j.jinorgbio.2017.08.016

25. Pella, B. J.; Niklas, J.; Poluektov, O. G.; Mukherjee, A. Effects of Denticity and Ligand Rigidity on Reactivity of Copper Complexes with Cumyl Hydroperoxide. Inorganica Chim. Acta 2018, 483, 71–78. https://doi.org/10.1016/j.ica.2018.07.035.

26. Kim, B.; Jeong, D.; Cho, J. Nucleophilic Reactivity of Copper(II)-Alkylperoxo Complexes. Chem. Commun. 2017, 53 (67), 9328–9331. https://doi.org/10.1039/c7cc03965d.

27. Börzel, H.; Comba, P.; Hagen, K. S.; Lampeka, Y. D.; Lienke, A.; Linti, G.; Merz, M.; Pritzkow, H.; Tsymbal, L. V. Iron Coordination Chemistry with Tetra-, Penta- and Hexadentate Bispidine-Type Ligands. Inorganica

Chim. Acta 2002, 337, 407–419. https://doi.org/10.1016/S0020-1693(02)01100-3.

28. Comba, P.; Kanellakopulos, B.; Katsichtis, C.; Lienke, A.; Pritzkow, H.; Rominger, F. Synthesis and Characterisation of Manganese(II) Compounds with Tetradentate Ligands Based on the Bispidine Backbone. J. Chem. Soc. Dalt. Trans. 1998, No. 23, 3997–4002. https://doi.org/10.1039/A805944F.
29. Wang, D.; Ray, K.; Collins, M. J.; Farquhar, E. R.; Frisch, J. R.; Gómez, L.; Jackson, T. A.; Kerscher, M.; Waleska, A.; Comba, P.; Costas, M.; Que, L. Nonheme Oxoiron(IV) Complexes of Pentadentate N5 Ligands: Spectroscopy, Electrochemistry, and Oxidative Reactivity. Chem. Sci. 2013, 4 (1), 282–291. https://doi.org/10.1039/c2sc21318d.
30. Barman, P.; Vardhaman, A. K.; Martin, B.; Wörner, S. J.; Sastri, C. V.; Comba, P. Influence of Ligand Architecture on Oxidation Reactions by High-Valent Nonheme Manganese Oxo Complexes Using Water as a Source of Oxygen. Angew. Chemie - Int. Ed. 2015, 54 (7), 2095–2099. https://doi.org/10.1002/anie.201409476.
31. Barman, P.; Faponle, A. S.; Vardhaman, A. K.; Angelone, D.; Löhr, A. M.; Browne, W. R.; Comba, P.; Sastri, C. V.; De Visser, S. P. Influence of Ligand Architecture in Tuning Reaction Bifurcation Pathways for Chlorite Oxidation by Non-Heme Iron Complexes. Inorg. Chem. 2016, 55 (20), 10170–10181. https://doi.org/10.1021/acs.inorgchem.6b01384.
32. Bukowski, M. R.; Comba, P.; Limberg, C.; Merz, M.; Que, L.; Wistuba, T. Bispidine Ligand Effects on Iron/Hydrogen Peroxide Chemistry.

Angew. Chemie - Int. Ed. 2004, 43 (10), 1283–1287. https://doi.org/10.1002/anie.200352523.

33. Comba, P.; Jakob, M.; Rück, K.; Wadepohl, H. Tuning of the Properties of a Picolinic Acid-Based Bispidine Ligand for Stable Copper(II) Complexation. Inorganica Chim. Acta 2018, 481, 98–105. https://doi.org/10.1016/j.ica.2017.08.022.
34. Comba, P.; Lienke, A. Bispidine Copper(II) Compounds: Effects of the Rigid Ligand Backbone. Inorg. Chem. 2001, 40 (20), 5206–5209. https://doi.org/10.1021/ic010200r.
35. Anastasi, A. E.; Comba, P.; McGrady, J.; Lienke, A.; Rohwer, H. Electronic Structure of Bispidine Iron(IV) Oxo Complexes. Inorg. Chem. 2007, 46 (16), 6420–6426. https://doi.org/10.1021/ic700429x.
36. Börzel, H.; Comba, P.; Hagen, K. S.; Kerscher, M.; Pritzkow, H.; Schatz, M.; Schindler, S.; Walter, O. Copper-Bispidine Coordination Chemistry: Syntheses, Structures, Solution Properties, and Oxygenation Reactivity. Inorg. Chem. 2002, 41 (21), 5440–5452. https://doi.org/10.1021/ic011114u.
37. Barman, P.; Upadhyay, P.; Faponle, A. S.; Kumar, J.; Nag, S. S.; Kumar, D.; Sastri, C. V.; de Visser, S. P. Deformylation Reaction by a Nonheme Manganese(III)–Peroxo Complex via Initial Hydrogen-Atom Abstraction. Angew. Chemie - Int. Ed. 2016, 55 (37), 11091–11095. https://doi.org/10.1002/anie.201604412.

38. Cantú Reinhard, F. G.; Barman, P.; Mukherjee, G.; Kumar, J.; Kumar, D.; Kumar, D.; Sastri, C. V.; De Visser, S. P. Keto-Enol Tautomerization Triggers an Electrophilic Aldehyde Deformylation Reaction by a Nonheme Manganese(III)-Peroxo Complex. J. Am. Chem. Soc. 2017, 139 (50), 18328–18338. https://doi.org/10.1021/jacs.7b10033.

Chapter 4: Substrate triggered conversion of η^2 to η^1-Fe(III)-peroxo for deformylation of cyclohexanecarbaxaldehyde

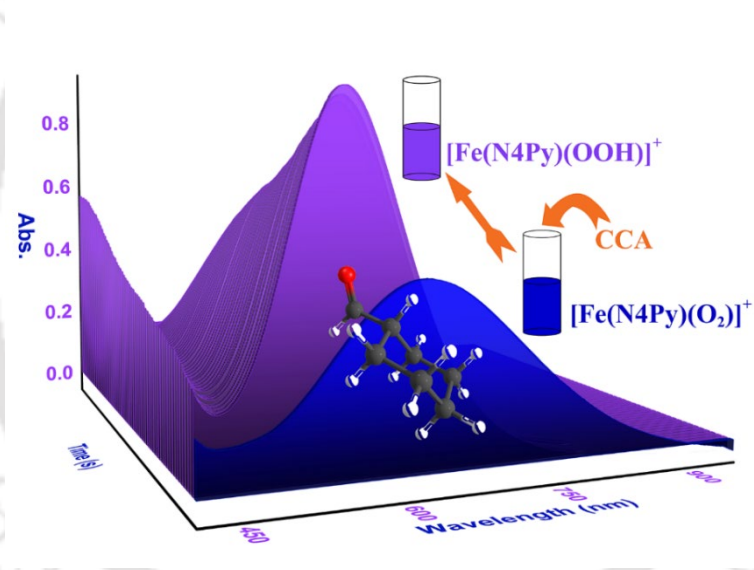

4.1 Introduction

The central metal atom's similarity with the natural AD enzyme, like cADO, P450, makes Fe(III)-peroxo complexes more interesting for deformylation.[1-7] Though cADO utilizes a diiron-based ferritin-like active site; the mononuclear counterpart becomes more critical because of their less structural complexity and ease in handling. The mechanism for aldehyde deformylation by Fe(III)-peroxo species has been considered a nucleophilic attack at the aldehyde's carbonyl carbon.[8-17] Earlier developments, in our lab, on the deformylation by Mn(III)-peroxo and Cu(II)-alkylperoxo species suggest otherwise; and we have been very curious to know the details for Fe(III)-peroxo system. For this purpose, we use 2-phenylpropionaldehyde (2-PPA), cyclohexanecarboxaldehyde, and their isotopic derivative as the model substrate in this work.

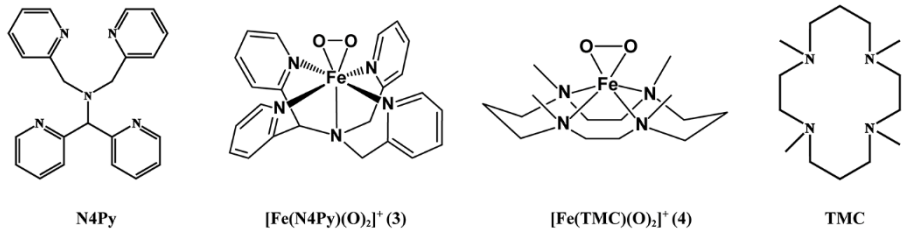

Figure 4.1 Molecular structure of the ligands and Fe(III)-peroxo complexes studied in this work.

The H-atom abstraction mechanism has been postulated based on isotope labeling experiments.[18-20] The hydrogen atom's replacement, by its isotope D, at the α-position of 2-PPA, decreases the rate. We have searched the literature at our best but unable to find out any isotope labeling experiment at α-position for the deformylation Fe(III)-peroxo system. To get more insight into the deformylation mechanism for Fe(III)-peroxo intermediate, we have used α-D-2-PPA and α-D-CCA as mechanical probes. In this chapter, we report generation, characterization and reactivity towards deformylation reaction of aldehydes by two well known Fe(III)-peroxo system namely, $[Fe(N4Py)(O_2)]^+$ (**3**) (N4Py = N,N-bis(2-pyridylmethyl)-N-bis(2-pyridyl)methylamine) and $[Fe(TMC)(O_2)]^+$ (**4**) (TMC = 1,4,8,11-tetramethyl-1,4,8,11-tetraazacyclotetradecane) (Figure 4.1). These two peroxo species are known for years and well-characterized by various research groups.

4.2 Experimanetal Section

The intermediates (**3**) and (**4**), generated in trifluoroethanol (TFE) using H_2O_2 as an oxidizing agent in the presence of triethylamine (TEA), according to the reported procedure in the literature.[14,15]

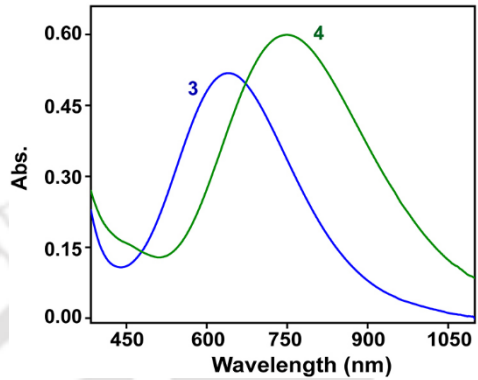

*Figure 4.2 UV-Vis absorption spectra for **3** and **4**.*

Addition of 10 equivalents of H_2O_2 to a 1 mM yellow color solution containing [Fe(N4Py)(OTf)](OTf) and 5 equivalents of triethylamine in TFE at 258K afforded blue intermediate **3** with an utmost absorption wavelength λ_{max} at 685 nm ($\varepsilon = 520\ M^{-1}\ cm^{-1}$).[21] Intermediate **4** has been generated by a similar method, and green coloration of the solution indicates the formation of $[Fe(TMC)(O_2)]^+$ with an intense band at 750 nm ($\varepsilon = 600\ M^{-1}\ cm^{-1}$) TFE at 288 K.

4.3 Result and Discussion

The electrospray ionization mass spectrum (ESI-MS) of **3** shows a prominent feature at m/z 455.21, whose isotopic distribution pattern corresponds to $[Fe(N4Py)(O_2)]^+$ (calculated m/z of 455.10). We have observed a prominent mass ion peak at m/z 344.07 (calculated m/z of 344.19) in the ESI-MS for intermediate **4** (Figure 4.3).

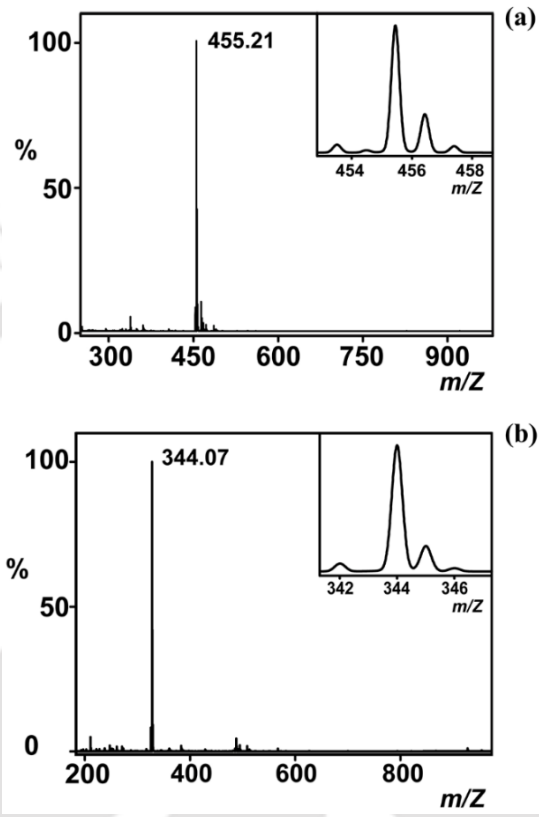

*Figure 4.3 ESI-MS spectrum of **3** (a) and **4** (b) [inset shows the isotopic distribution of the prominent peak].*

We then investigated the reactivity of both the intermediate in aldehyde deformylation reaction. Upon adding 100 equivalent of 2-phenylpropionaldehyde (2-PPA) to a **3** (1 mM) solution at 258 K in TFE, the intermediates decay down (Figure 4.4), allowing us to measure the second-order rate constant.

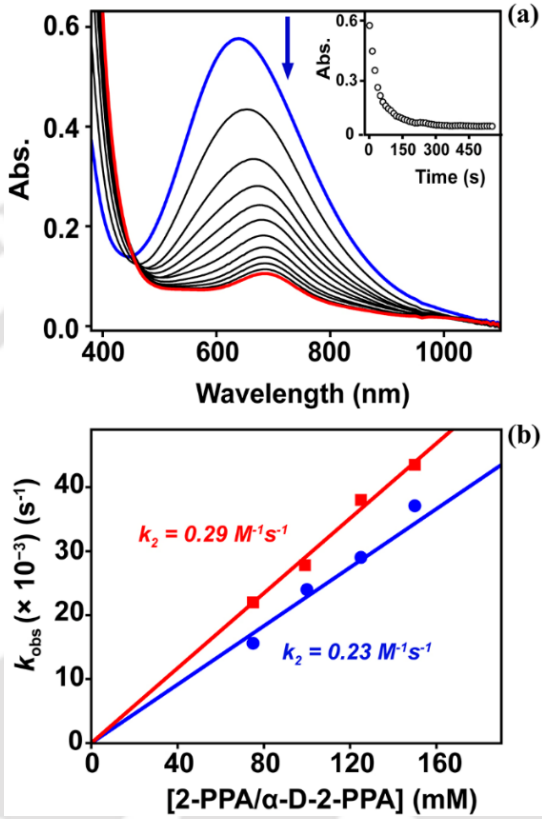

*Figure 4.4 (a) UV-Vis absorption spectra for the reaction of **3** with 2-PPA. (b) The plot of pseudo-first-order rate constant (k_{obs}) against the different concentrations of 2-PPA (■) and α-D-2-PPA (●).*

The measurement of the decay in the UV-Vis absorption band corresponding to **3** with time gives a pseudo-first-order (k_{obs}) rate constant. The k_{obs} value increases linearly with an increase in the substrate concentration. A plot of k_{obs} against the substrate concentration provides a second-order rate constant of 0.29 $M^{-1}s^{-1}$.

The recent development of a mechanism for deformylation reaction suggesting an initial alpha H atom abstraction from 2-PPA by Mn(III)-peroxo based complex tempted us to reinvestigate the mechanism of aldehyde deformylation reaction of Fe(III) based peroxo intermediates. Fe(III)-peroxo is known to proceed via a nucleophilic carbonyl attack for aldehyde deformylation reaction. To get more impending into this matter, we have decided to study the reaction of **3** using 2-PPA, cyclohexanecarboxaldehyde (CCA), and their deuterated derivatives.

The intention is to check whether **3** reacts via either traditional carbonyl attack for deformylation of an aldehyde or initial hydrogen atom abstraction. After the addition of the α-D-2-PPA, the intermediate started to decay down. The pseudo-first-order rate constants of the reaction increased proportionally with the increasing substrate concentration, which allowed us to measure a second-order rate constant (k_2) of 0.23 $M^{-1}s^{-1}$ (the slight deviation from the original one due to the presence of water in the medium).[22,23] The result indicates that there is no kinetic isotope effect (KIE) for the H atom at α-position. So, the initial H atom abstraction from the α-position of 2-PPA is not a possibility for $[Fe(N4Py)(O_2)]^+$.

Another widely used model substrate to determine the deformylation mechanistic pathway for synthetic peroxo systems is CCA. When we add 100 equivalent of CCA to 1 mM TFE solution of intermediate **3** at 243 K, the electronic absorption spectra of **3** give an immediate blue shift of 140 nm from 685 nm to 540 nm. Surprisingly, the solution changes from blue to purple, with

a new absorption maximum at 540 nm. The purple solution's electronic absorption feature suggests a similarity with the previously reported Fe(III)-hydroperoxo species. Earlier reports suggested the conversion between blue η^2 to purple η^1 species is pH controlled.[21,24] We have also repeated the experiments for **3** and observed the same result (Figure 4.5).

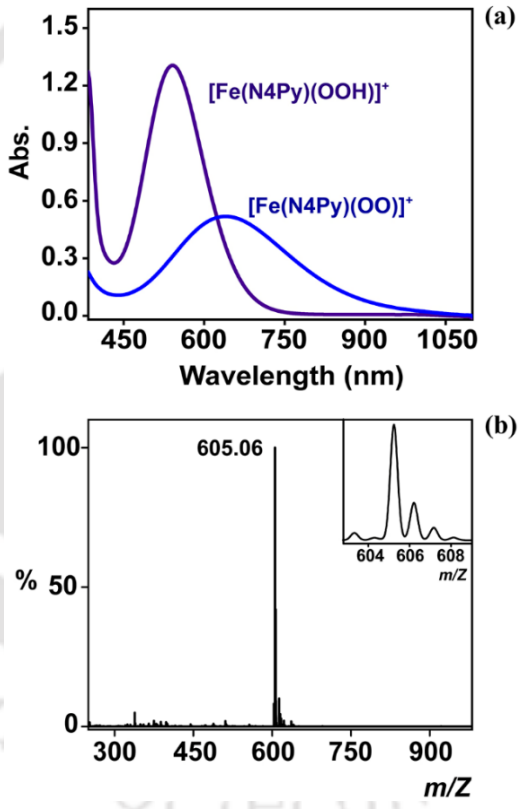

Figure 4.5 (a). UV-Vis absorption spectra for the conversion between η^2 to η^1 Fe(III)peroxo in the presence of acid at 288K (b) ESI-MS spectra of the species having electronic absorption at 540 nm.

We have performed an ESI-MS experiment for further confirmation and found a prominent feature at m/*Z* 605.06 corresponding to $\{[(N4Py)Fe(OOH)](OTf)\}^{+}$. The interconversion without altering the pH of the medium has come as a surprise to us.

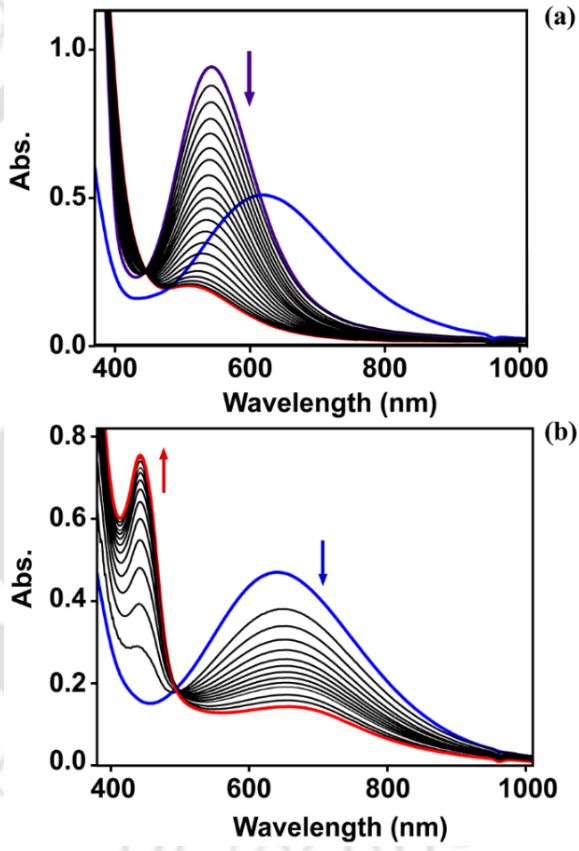

*Figure 4.6 (a) UV-Vis absorption spectra for the reaction of **3** and CCA with a blue shift. (b) UV-Vis absorption spectra for the reaction of 1-D-CCA and **3** at 238K.*

To check whether this Fe(III)-OOH formation results from the H-atom abstraction from the α-positions, we add 100 equivalent α-D-CCA to the solution of **3** at 238 K. The intermediate shows a similar spectral pattern to that of reaction with CCA with a color change from blue to purple.

To confirm our hypothesis, when we add 100 equivalents of 1-D-CCA to a 1 mM solution of intermediate **3**, the absorption band decayed immediately with no blue shift, and the intermediate reverted to the iron(II) complex with an isosbestic point at 450 nm (Figure 4.6). This result supported the role of the aldehyde's H atom in the reaction of Fe-N4Py-peroxo with CCA and suggested that the Fe-N4Py-peroxo complex is not following a nucleophilic carbonyl attack mechanism for deformylation of CCA.

The deformylation of CCA has been studied previously with intermediate **4**, and there was no report for such an anomaly. So, we have decided to explore the effect of isotopic substitution with **4**. The addition of 100 equivalent CCA to a 1 mM TFE solution of **4** at 258 K started the absorption band's decay without any shift (Figure 2.18). When we investigated the reaction of **4** with α-D-CCA, there was no significant change in rate. To further explore the mechanism, we have decided to check the reactivity of **4** with 1-D-CCA. To a TFE solution of **4** at 258 K, the addition of 100 equivalents 1-D-CCA makes the reaction slower, and the intermediate decays with its natural decay rate. The absence of KIE for α-position in both substrates implicates that α-H atom abstraction is impossible for **3** and **4**. Compared to CCA, the slower decay rate with 1-D-CCA suggests the aldehyde's H-atom's involvement in the reaction.

4.4 Conclusions

This chapter discussed the mechanism for the aldehyde deformylation reaction of Fe(III)-peroxo species with different commonly used model substrates. This study's target has been reinvestigating the ideal mechanism for the aldehyde deformylation by Fe(III)-peroxo by isotope labeling and kinetics measurement. The careful research and analysis of the data prove that the most feasible mechanism is a nucleophilic carbonyl attack for the Fe(III)-peroxo species. Still, the reaction pathway can differ from substrate to substrate, and it proceeds via an initial H atom abstraction, especially for CCA. This mechanism involves an in situ conversion between two different forms of Fe(III)-peroxo systems but the further steps involved in the reactions is yet to be discovered. In our lab, we are continuously working on unfolding that knot. Future studies will center on understanding the detailed mechanisms of the aldehyde deformylation reaction of Fe-N4Py-peroxo intermediate.

4.5 References

1. Dennis, M. W.; Kolattukudy, P. E. Alkane Biosynthesis by Decarbonylation of Aldehyde Catalyzed by a Microsomal Preparation from Botryococcus Braunii. Arch. Biochem. Biophys. 1991, 287 (2), 268–275. https://doi.org/10.1016/0003-9861(91)90478-2.
2. Qiu, Y.; Tittiger, C.; Wicker-Thomas, C.; Le Goff, G.; Young, S.; Wajnberg, E.; Fricaux, T.; Taquet, N.; Blomquist, G. J.; Feyereisen, R. An Insect-Specific P450 Oxidative Decarbonylase for Cuticular Hydrocarbon Biosynthesis. Proc. Natl. Acad. Sci. U. S. A. 2012, 109 (37), 14858–14863. https://doi.org/10.1073/pnas.1208650109.
3. Reed, J. R.; Vanderwel, D.; Choi, S.; George Pomonis, J.; Reitz, R. C.; Blomquist, G. J. Unusual Mechanism of Hydrocarbon Formation in the Housefly: Cytochrome P450 Converts Aldehyde to the Sex Pheromone Component (Z)-9-Tricosene and CO_2. Proc. Natl. Acad. Sci. U. S. A. 1994, 91 (21), 10000–10004. https://doi.org/10.1073/pnas.91.21.10000.
4. Warui, D. M.; Li, N.; Nørgaard, H.; Krebs, C.; Bollinger, J. M.; Booker, S. J. Detection of Formate, Rather than Carbon Monoxide, As the Stoichiometric Coproduct in Conversion of Fatty Aldehydes to Alkanes by a Cyanobacterial Aldehyde Decarbonylase. J. Am. Chem. Soc. 2011, 133 (10), 3316–3319. https://doi.org/10.1021/ja111607x.
5. Aarts, M. G.; Keijzer, C. J.; Stiekema, W. J.; Pereira, A. Molecular Characterization of the CER1 Gene of Arabidopsis Involved in

Epicuticular Wax Biosynthesis and Pollen Fertility. Plant Cell 1995, 7 (12), 2115 – 2127. https://doi.org/10.1105/tpc.7.12.2115.

6. Cheesbrough, T. M.; Kolattukudy, P. E. Alkane Biosynthesis by Decarbonylation of Aldehydes Catalyzed by a Particulate Preparation from Pisum Sativum. Proc. Natl. Acad. Sci. U. S. A. 1984, 81 (21), 6613–6617. https://doi.org/10.1073/pnas.81.21.6613.
7. Yoder, J. A.; Denlinger, D. L.; Dennis, M. W.; Kolattukudy, P. E. Enhancement of Diapausing Flesh Fly Puparia with Additional Hydrocarbons and Evidence for Alkane Biosynthesis by a Decarbonylation Mechanism. Insect Biochem. Mol. Biol. 1992, 22 (3), 237–243. https://doi.org/10.1016/0965-1748(92)90060-R.
8. Meunier, B.; de Visser, S. P.; Shaik, S. Mechanism of Oxidation Reactions Catalyzed by Cytochrome P450 Enzymes. Chem. Rev. 2004, 104 (9), 3947–3980. https://doi.org/10.1021/cr020443g.
9. Buer, B. C.; Paul, B.; Das, D.; Stuckey, J. A.; Marsh, E. N. G. Insights into Substrate and Metal Binding from the Crystal Structure of Cyanobacterial Aldehyde Deformylating Oxygenase with Substrate Bound. ACS Chem. Biol. 2014, 9 (11), 2584–2593. https://doi.org/10.1021/cb500343j.
10. Li, N.; Nørgaard, H.; Warui, D. M.; Booker, S. J.; Krebs, C.; Bollinger, J. M. Conversion of Fatty Aldehydes to Alka(e)Nes and Formate by a

Cyanobacterial Aldehyde Decarbonylase: Cryptic Redox by an Unusual Dimetal Oxygenase. J. Am. Chem. Soc. 2011, 133 (16), 6158–6161. https://doi.org/10.1021/ja2013517.

11. Paul, B.; Das, D.; Ellington, B.; Marsh, E. N. G. Probing the Mechanism of Cyanobacterial Aldehyde Decarbonylase Using a Cyclopropyl Aldehyde. J. Am. Chem. Soc. 2013, 135 (14), 5234–5237. https://doi.org/10.1021/ja3115949.
12. Suda, K.; Kikkawa, T.; Nakajima, S.; Takanami, T. Highly Regio- and Stereoselective Rearrangement of Epoxides to Aldehydes Catalyzed by High-Valent Metalloporphyrin Complex, Cr(TPP)OTf. J. Am. Chem. Soc. 2004, 126 (31), 9554–9555. https://doi.org/10.1021/ja047104k.
13. Shokri, A.; Que, L. Conversion of Aldehyde to Alkane by a Peroxoiron(III) Complex: A Functional Model for the Cyanobacterial Aldehyde-Deformylating Oxygenase. J. Am. Chem. Soc. 2015, 137 (24), 7686–7691. https://doi.org/10.1021/jacs.5b01053.
14. Annaraj, J.; Suh, Y.; Seo, M. S.; Kim, S. O.; Nam, W. Mononuclear Nonheme Ferric-Peroxo Complex in Aldehyde Deformylation. Chem. Commun. 2005, No. 36, 4529–4531. https://doi.org/10.1039/b505562h.
15. Cho, J.; Jeon, S.; Wilson, S. A.; Liu, L. V.; Kang, E. A.; Braymer, J. J.; Lim, M. H.; Hedman, B.; Hodgson, K. O.; Valentine, J. S.; Solomon, E. I.; Nam, W. Structure and Reactivity of a Mononuclear Non-Haem Iron(III)-Peroxo Complex. Nature 2011, 478 (7370), 502–505. https://doi.org/10.1038/nature10535.

16. Itzel, H.; Fischer, H. Electron Spin Resonance of Oxiranyl Radicals in Solution: Configurational Stabilities and Rearrangement Reactions. Helv. Chim. Acta 1976, 59 (3), 880–901. https://doi.org/https://doi.org/10.1002/hlca.19760590318.
17. Das, D.; Ellington, B.; Paul, B.; Marsh, E. N. G. Mechanistic Insights from Reaction of α-Oxiranyl-Aldehydes with Cyanobacterial Aldehyde Deformylating Oxygenase. ACS Chem. Biol. 2014, 9 (2), 570–577. https://doi.org/10.1021/cb400772q.
18. Barman, P.; Upadhyay, P.; Faponle, A. S.; Kumar, J.; Nag, S. S.; Kumar, D.; Sastri, C. V.; de Visser, S. P. Deformylation Reaction by a Nonheme Manganese(III)–Peroxo Complex via Initial Hydrogen-Atom Abstraction. Angew. Chemie - Int. Ed. 2016, 55 (37), 11091–11095. https://doi.org/10.1002/anie.201604412.
19. Cantú Reinhard, F. G.; Barman, P.; Mukherjee, G.; Kumar, J.; Kumar, D.; Kumar, D.; Sastri, C. V.; De Visser, S. P. Keto-Enol Tautomerization Triggers an Electrophilic Aldehyde Deformylation Reaction by a Nonheme Manganese(III)-Peroxo Complex. J. Am. Chem. Soc. 2017, 139 (50), 18328–18338. https://doi.org/10.1021/jacs.7b10033.
20. Nag, S. S.; Mukherjee, G.; Barman, P.; Sastri, C. V. Influence of Induced Steric on the Switchover Reactivity of Mononuclear Cu(II)-Alkylperoxo Complexes. Inorganica Chim. Acta 2019, 485, 80–85. https://doi.org/10.1016/j.ica.2018.09.087.
21. Ho, R. Y. N.; Roelfes, G.; Hermant, R.; Hage, R.; Feringa, B. L.; Que, L. Resonance Raman Evidence for the Interconversion between an [Fe^{III}-

η^1-OOH]$^{2+}$ and [Fe^{III}-η^2-O_2]$^+$ Species and Mechanistic Implications Thereof. Chem. Commun. 1999, 21, 2161–2162. https://doi.org/10.1039/a905535e.

22. Bailey, W. D.; Gagnon, N. L.; Elwell, C. E.; Cramblitt, A. C.; Bouchey, C. J.; Tolman, W. B. Revisiting the Synthesis and Nucleophilic Reactivity of an Anionic Copper Superoxide Complex. Inorg. Chem. 2019, 58 (8), 4706–4711. https://doi.org/10.1021/acs.inorgchem.9b00090.
23. Narulkar, D. D.; Ansari, A.; Vardhaman, A. K.; Harmalkar, S. S.; Lingamallu, G.; Dhavale, V. M.; Sankaralingam, M.; Das, S.; Kumar, P.; Dhuri, S. N. A Side-on Mn(III)–Peroxo Supported by a Non-Heme Pentadentate N3Py2 Ligand: Synthesis, Characterization and Reactivity Studies. Dalt. Trans. 2021, 50 (8), 2824. https://doi.org/10.1039/d0dt03706k.
24. Hazell, A.; McKenzie, C. J.; Nielsen, L. P.; Schindler, S.; Weitzer, M. Mononuclear Non-Heme Iron(III) Peroxide Complexes: Syntheses, Characterisation, Mass Spectrometric and Kinetic Studies. J. Chem. Soc. Dalt. Trans. 2002, 3, 310–317. https://doi.org/10.1039/b103844n.

Chapter 5: Establishment of a pristine mechanistic pathway for aldehyde deformylation by Mn(III)-peroxo intermediates

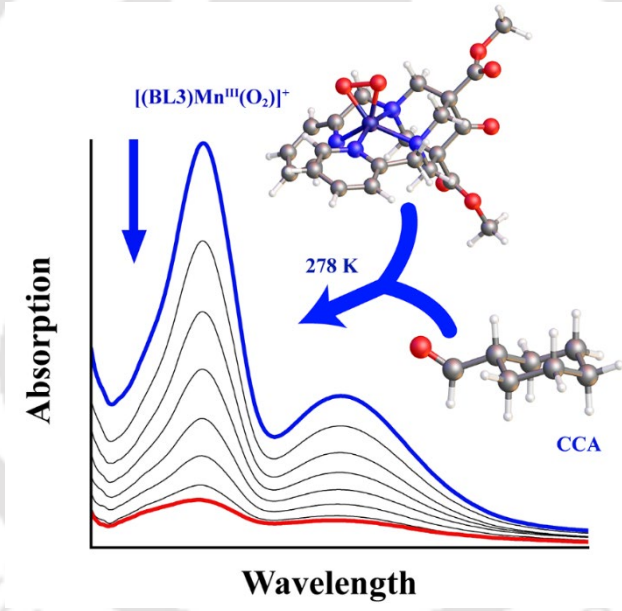

5.1 Introduction

Various enzymes in biological systems supplicated Mn-peroxo intermediate in their catalytic cycles. During the last two decades, many new Mn-oxygen intermediates have been generated, and multiple groups studied their reactivity in different kinds of essential reactions, including aldehyde deformylation.[1-13] Aldehyde deformylation often studied using 2-phenylpropionaldehyde (2-PPA) and cyclohexancaroboxaldehyde (CCA) as model substrates.[14-22] The mechanistic resemblance among most of them is that they proceed via the nucleophilic attack to aldehyde's carbonyl carbon. During the earlier studies by our group, we have found an alternative reaction pathway from the conventional nucleophilic attack at carbonyl carbon for 2-PPA. The reactivity of Fe(III)-peroxo system with 2-PPA and CCA has proved the possibility of a different kind of mechanism for the later one. This experimental result inspires us to investigate the facts further to convey a more accurate reaction mechanism for aldehyde deformylation by Mn(III)-peroxo species. In this study, we have synthesized a new tetradentate N-donor-based Mn(II)-complex (Figure 5.1). We were able to generate Mn(III)-peroxo adduct from the Mn(II) precursor and characterized by various spectroscopic techniques. The aldehyde deformylation reaction was studied using CCA and their derivatives as the model substrates.

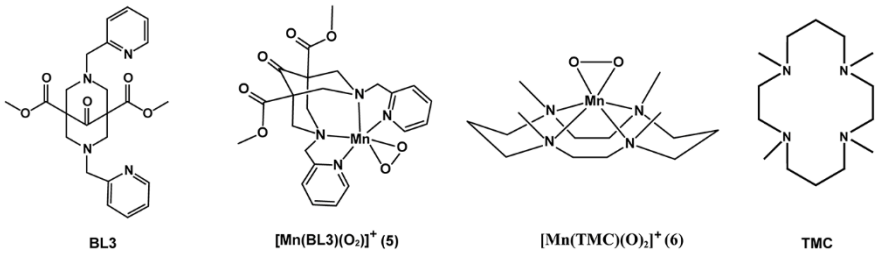

*Figure 5.1 Molecular structure of the ligand and Mn(III)-peroxo intermediate **5** and **6** studied in this work.*

5.2 Experimental Section

Mn(III)-peroxo intermediates were generated in situ. Intermediate $[Mn(L1)(O_2)]^+$ (**5**) was generated by the addition of 10 equivalent of H_2O_2 and 1.5 equivalent of TEA at 278 K to an acetonitrile solution of the Mn(II) precursor (3a, Sec. 2.2.4.2). Intermediate $[Mn(TMC)(O_2)]^+$ (**6**) was generated in an acetonitrile solution at 298 K using an earlier reported procedure.[3]

5.3 Result and Discussions

The Mn(III)-peroxo species has an intense electronic absorption band at 458 nm (ε = 230 L mol^{-1} cm^{-1}) and weak absorption band on the d-d region at 585 nm (ε = 78 L mol^{-1} cm^{-1}) (Figure 5.2). The electrospray ionization mass spectrum (ESI-MS) of the green intermediate gives a dominant ion peak at *m/z* 525.13 (calcd. 525.12) corresponds to $[Mn(L1)(O_2)]^+$ (**5**), and the isotope distribution pattern also corresponds to the presence of the same species in the

solution. The electronic absorption spectrum is very similar to other well-characterized tetradentate N4 ligand-based Mn(III)-peroxo intermediates.

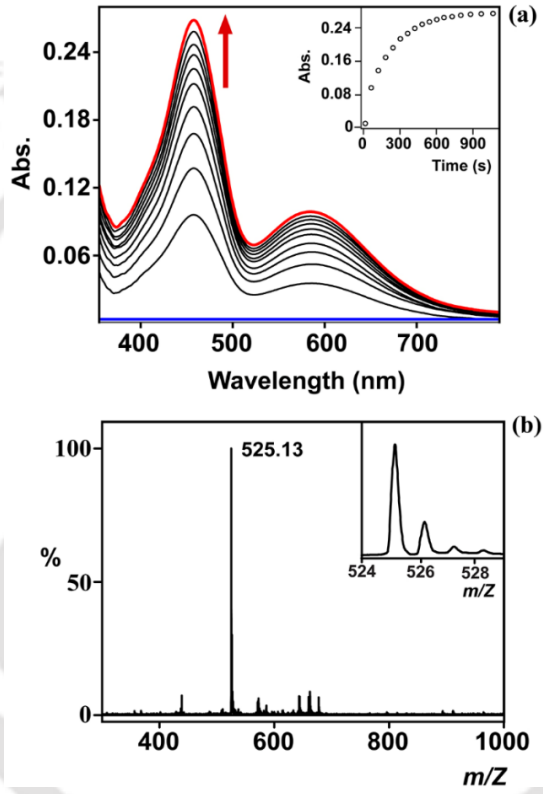

*Figure 5.2 (a) UV-Vis spectra for the formation of **5** at 278 K. (b) ESI-MS spectrum of **5** [inset shows the isotopic distribution of the prominent peak].*

We could not get Resonance-Raman spectra for this complex because of its similarity in properties with previously reported bispidine containing Mn(III)-peroxo complex.[23] The electronic absorption spectral similarities with other

crystallographically characterized Mn(III)-peroxo systems along with the ESI-MS spectra guide us to conclude that the green intermediate is also a side-on Mn(III)-peroxo complex. Cyclohexanecarboxaldehyde(CCA) is a classical substrate to determine the reactivity of various metal-oxygen complexes in the deformylation reaction and classify as nucleophilic oxidants. Upon adding CCA to 1 mM acetonitrile solution at 278 K, the intermediate decayed down (Figure 5.3), which allows us to measure the second-order rate constant for the reaction. The reaction rate increases proportionally with increasing substrate concentration. The plot of pseudo-first-order (k_{obs}) rate constant against substrate concentration gives a second-order (k_2) rate constant of 0.85 M^{-1} s^{-1}. One of the recently evolved mechanisms for aldehyde deformylation by Mn(III)-peroxo intermediates is an initial H-atom abstraction from the α-position of aldehyde. To understand the possibility of aldehyde's α-H atom abstraction, we use 2-Me-CCA as a substrate. The addition of 2-Me-CCA to an acetonitrile solution of **5** at 278 K causes a fast decay of the absorption band, giving a second-order rate constant of 0.97 $M^{-1}s^{-1}$.

The higher reactivity with 2-Me-CCA comes as a surprise considering the previously reported α-H abstraction by Mn(III)-peroxo intermediate. To find out the meticulous mechanism, inspired by the reactivity of Fe(III)-peroxo, we add 1-D-CCA as a mechanical probe. The reaction rate slows down upon the addition of 1-D-CCA to **5** at 278 K, giving a k_2 value of 0.009 M^{-1} s^{-1}.

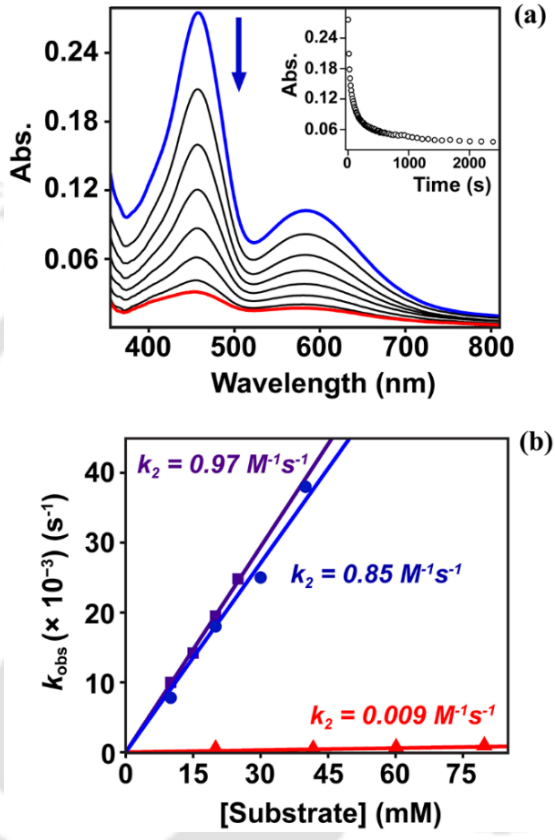

Figure 5.3 (a) UV-Vis spectra for the decay of ***5*** *upon adding 20 mM CCA to an acetonitrile solution (1 mM) of* ***5*** *at 278K. (b) A plot of pseudo-first-order rate constant (k_{obs}) against the different concentrations of CCA (●), 2-Me-CCA (■), and 1-d-CCA (▲).*

This result indicates the involvement of aldehyde C-H bond dissociation in the rate-determining step (RDS). To explore whether the initial aldehyde H atom abstraction is only applicable for bispidine based Mn(III)-peroxo intermediates or not, we have used Mn(III)-peroxo intermediate bearing TMC ligand,

$[Mn(TMC)(O)_2]^+$ (**6**). The reason behind selecting the TMC based Mn(III)-peroxo intermediate is that it is well characterized and has a similar electronic absorption pattern to that of the bispidine based system.[3,22] According to previous reports, it reacts with CCA via a nucleophilic attack at carbonyl carbon. Still, we were unable to find out any isotope labeling experiment in literature for the same. Upon adding CCA to an acetonitrile solution of **6** at 273K, we have observed a second-order rate constant of 0.31 $M^{-1}s^{-1}$, similar to the previously reported value.

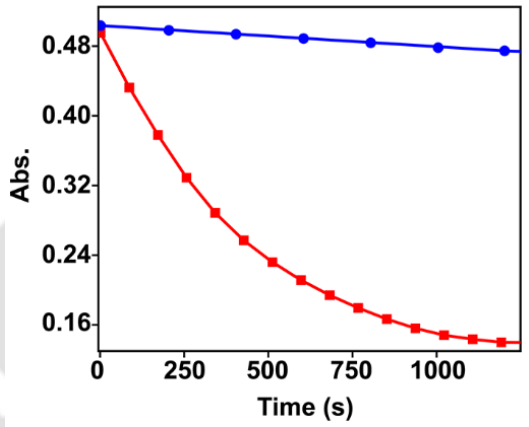

*Figure 5.4 Change in absorption with time upon addition of 150 mM of CCA (■) and 1-d-CCA (●) to an acetonitrile solution (1 mM) of **6**.*

To investigate the mechanism in more detail, we use 1-D-CCA as a substrate. Upon the deuterated substrate's addition, the reaction becomes very slow, and the intermediate decays with its natural decay rate (Figure 5.4). This result suggests that TMC based Mn(III)-peroxo also reacts with CCA via aldehyde's

H-atom abstraction. The ligand architecture around the metal ion has no significant impact on the mechanistic pathway. We have proposed a probable mechanism for the reaction (Figure 5.5).

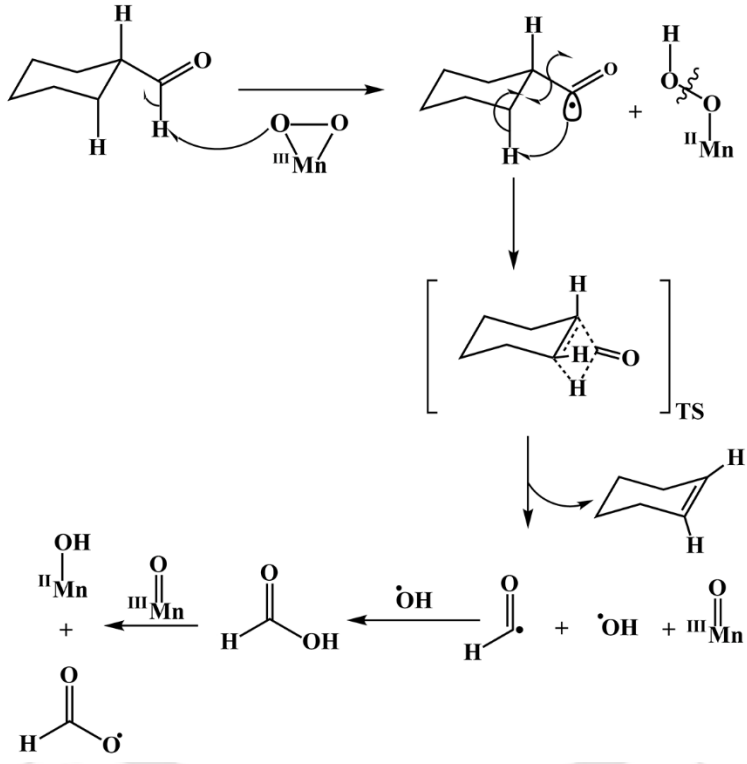

Figure 5.5 Proposed mechanism for deformylation of CCA by ***5****.*

5.4 Conclusions

As a consequence of our kinetics and reactivity study, we can confirm that the Mn(III)-peroxo intermediates react with CCA via an initial aldehyde H-atom abstraction from aldehyde. From the results obtained for the reaction, we can conclude that the alpha H atom of CCA is not involved in the RDS for CCA's deformylation. The slight rate increment in the case of 2-Me-CCA could result from the TS's stability through hyperconjugation from the methyl group, further support this mechanism. However, a detailed DFT study is in progress for getting thermodynamic aspects of the reaction mechanism.

5.5 References

1. Cho, J.; Sarangi, R.; Annaraj, J.; Kim, S. Y.; Kubo, M.; Ogura, T.; Solomon, E. I.; Nam, W. Geometric and Electronic Structure and Reactivity of a Mononuclear Side-on Nickel(III)-Peroxo Complex. Nat. Chem. 2009, 1 (7), 568–572. https://doi.org/10.1038/nchem.366.
2. Goto, Y.; Wada, S.; Morishima, I.; Watanabe, Y. Reactivity of Peroxoiron(III) Porphyrin Complexes: Models for Deformylation Reactions Catalyzed by Cytochrome P-450. J. Inorg. Biochem. 1998, 69 (4), 241–247. https://doi.org/10.1016/S0162-0134(97)10029-0.
3. Seo, M. S.; Kim, J. Y.; Annaraj, J.; Kim, Y.; Lee, Y. M.; Kim, S. J.; Kim, J.; Nam, W. $[Mn(Tmc)(O_2)]^+$: A Side-on Peroxido Manganese(III) Complex Bearing a Non-Heme Ligand. Angew. Chemie - Int. Ed. 2007, 46 (3), 377–380. https://doi.org/10.1002/anie.200603414.
4. Colmer, H. E.; Howcroft, A. W.; Jackson, T. A. Formation, Characterization, and O-O Bond Activation of a Peroxomanganese(III) Complex Supported by a Cross-Clamped Cyclam Ligand. Inorg. Chem. 2016, 55 (5), 2055–2069. https://doi.org/10.1021/acs.inorgchem.5b02398.
5. Shook, R. L.; Gunderson, W. A.; Greaves, J.; Ziller, J. W.; Hendrich, M. P.; Borovik, A. S. A Monomeric MnIII-Peroxo Complex Derived Directly from Dioxygen. Journal of the American Chemical Society. 2008, 8888–8889. https://doi.org/10.1021/ja802775e.

6. Cho, J.; Sarangi, R.; Kang, H. Y.; Lee, J. Y.; Kubo, M.; Ogura, T.; Solomon, E. I.; Nam, W. Synthesis, Structural, and Spectroscopic Characterization and Reactivities of Mononuclear Cobalt(III)-Peroxo Complexes. J. Am. Chem. Soc. 2010, 132 (47), 16977–16986. https://doi.org/10.1021/ja107177m.
7. Kovacs, J. A. Tuning the Relative Stability and Reactivity of Manganese Dioxygen and Peroxo Intermediates via Systematic Ligand Modification. Acc. Chem. Res. 2015, 48 (10), 2744–2753. https://doi.org/10.1021/acs.accounts.5b00260.
8. Lee, C. M.; Chuo, C. H.; Chen, C. H.; Hu, C. C.; Chiang, M. H.; Tseng, Y. J.; Hu, C. H.; Lee, G. H. Structural and Spectroscopic Characterization of a Monomeric Side-on Manganese(IV) Peroxo Complex. Angew. Chemie - Int. Ed. 2012, 51 (22), 5427–5430. https://doi.org/10.1002/anie.201201735.
9. Wallen, C. M.; Bacsa, J.; Scarborough, C. C. Coordination of Hydrogen Peroxide with Late-Transition-Metal Sulfonamido Complexes. Inorg. Chem. 2018, 57 (9), 4841–4848. https://doi.org/10.1021/acs.inorgchem.7b02514.
10. Guo, M.; Lee, Y. M.; Gupta, R.; Seo, M. S.; Ohta, T.; Wang, H. H.; Liu, H. Y.; Dhuri, S. N.; Sarangi, R.; Fukuzumi, S.; Nam, W. Dioxygen Activation and O-O Bond Formation Reactions by Manganese Corroles. J. Am. Chem. Soc. 2017, 139 (44), 15858–15867. https://doi.org/10.1021/jacs.7b08678.

11. So, H.; Park, Y. J.; Cho, K. Bin; Lee, Y. M.; Seo, M. S.; Cho, J.; Sarangi, R.; Nam, W. Spectroscopic Characterization and Reactivity Studies of a Mononuclear Nonheme Mn(III)-Hydroperoxo Complex. Journal of the American Chemical Society. 2014, 12229–12232. https://doi.org/10.1021/ja506275q.
12. Leto, D. F.; Jackson, T. A. Peroxomanganese Complexes as an Aid to Understanding Redox-Active Manganese Enzymes. J. Biol. Inorg. Chem. 2014, 19 (1), 1–15. https://doi.org/10.1007/s00775-013-1067-4.
13. Shook, R. L.; Peterson, S. M.; Greaves, J.; Moore, C.; Rheingold, A. L.; Borovik, A. S. Catalytic Reduction of Dioxygen to Water with a Monomeric Manganese Complex at Room Temperature. J. Am. Chem. Soc. 2011, 133 (15), 5810–5817. https://doi.org/10.1021/ja106564a.
14. Sankaralingam, M.; Jeon, S. H.; Lee, Y.-M.; Seo, M. S.; Ohkubo, K.; Fukuzumi, S.; Nam, W. An Amphoteric Reactivity of a Mixed-Valent Bis(μ-Oxo)Dimanganese(III,IV) Complex Acting as an Electrophile and a Nucleophile . Dalton Transactions. 2016, 376–383. https://doi.org/10.1039/c5dt04292e.
15. Geiger, R. A.; Chattopadhyay, S.; Day, V. W.; Jackson, T. A. Nucleophilic Reactivity of a Series of Peroxomanganese(III) Complexes Supported by Tetradentate Aminopyridyl Ligands. Dalt. Trans. 2011, 40 (8), 1707–1715. https://doi.org/10.1039/c0dt01570a.

16. Denler, M. C.; Wijeratne, G. B.; Rice, D. B.; Colmer, H. E.; Day, V. W.; Jackson, T. A. MnIII-Peroxo Adduct Supported by a New Tetradentate Ligand Shows Acid-Sensitive Aldehyde Deformylation Reactivity. Dalt. Trans. 2018, 47 (38), 13442–13458. https://doi.org/10.1039/c8dt02300j.
17. Narulkar, D. D.; Ansari, A.; Vardhaman, A. K.; Harmalkar, S. S.; Lingamallu, G.; Dhavale, V. M.; Sankaralingam, M.; Das, S.; Kumar, P.; Dhuri, S. N. A Side-on Mn(III)–Peroxo Supported by a Non-Heme Pentadentate N3Py2 Ligand: Synthesis, Characterization and Reactivity Studies . Dalt. Trans. 2021, 50 (8), 2824. https://doi.org/10.1039/d0dt03706k.
18. Magherusan, A. M.; Kal, S.; Nelis, D. N.; Doyle, L. M.; Farquhar, E. R.; Que, L.; McDonald, A. R. A $Mn^{II}Mn^{III}$ -Peroxide Complex Capable of Aldehyde Deformylation. Angew. Chemie Int. Ed. 2019, 58 (17), 5718–5722. https://doi.org/10.1002/anie.201900717.
19. Sankaralingam, M.; Lee, Y. M.; Jeon, S. H.; Seo, M. S.; Cho, K. Bin; Nam, W. A Mononuclear Manganese(III)-Hydroperoxo Complex: Synthesis by Activating Dioxygen and Reactivity in Electrophilic and Nucleophilic Reactions. Chem. Commun. 2018, 54 (10), 1209–1212. https://doi.org/10.1039/c7cc09492b.
20. Du, J.; Xu, D.; Zhang, C.; Xia, C.; Wang, Y.; Sun, W. Synthesis, Characterization, and Reactivity of a Side-on Manganese(III)-Peroxo Complex Bearing a Pentadentate Aminopyridine Ligand. Dalt. Trans. 2016, 45 (25), 10131–10135. https://doi.org/10.1039/c6dt00508j.

21. Saravanan, N.; Sankaralingam, M.; Palaniandavar, M. Manganese(II) Complexes of Tetradentate 4N Ligands with Diazepane Backbones for Catalytic Olefin Epoxidation: Effect of Nucleophilicity of Peroxo Complexes on Reactivity. RSC Adv. 2014, 4 (23), 12000–12011. https://doi.org/10.1039/c3ra44729d.

22. Annaraj, J.; Cho, J.; Lee, Y. M.; Kim, S. Y.; Latifi, R.; De Visser, S. P.; Nam, W. Structural Characterization and Remarkable Axial Ligand Effect on the Nucleophilic Reactivity of a Nonheme Manganese(III)-Peroxo Complex. Angew. Chemie - Int. Ed. 2009, 48 (23), 4150–4153. https://doi.org/10.1002/anie.200900118.

23. Cantú Reinhard, F. G.; Barman, P.; Mukherjee, G.; Kumar, J.; Kumar, D.; Kumar, D.; Sastri, C. V.; De Visser, S. P. Keto-Enol Tautomerization Triggers an Electrophilic Aldehyde Deformylation Reaction by a Nonheme Manganese(III)-Peroxo Complex. J. Am. Chem. Soc. 2017, 139 (50), 18328–18338. https://doi.org/10.1021/jacs.7b10033.

Chapter 6: Conclusions and Future Scope

6.1 Overview

Two types of mechanisms could achieve aldehyde biotransformation – one is the oxidation of the aldehyde to the carboxylic acid. The other is oxidative deformylation followed by conversion into one carbon reduced (n-1) product. The later process received much attention because of its similarity in reaction pathways with cholesterol and steroidogenesis's biosynthesis. The species responsible for the transformation of the carboxylic acid is considered to be an electrophilic metal-oxo. In contrast, the deformylation reaction proceeds via a nucleophilic attack of metal-bound peroxide to the aldehyde group's electrophilic carbon. Concomitant β-scission gives formate and less stable alkyl radical with one less carbon than the parent compound as the product. The alkyl radical afterward transformed either into alkene/alcohol or both. The physical and chemical properties of this alkyl radical control the nature of the product formed in the reaction. In our lab's earlier research, we observed a completely different type of mechanism is also a possibility. The earlier study was focused on the reactivity of a nonheme pentadentate Mn(III)-peroxo system in the deformylation of 2-PPA. This research has explored the mechanism of aldehyde deformylation by different nonheme transition metal-peroxo intermediates and the effect of ligand structure on their reactivity.

We have synthesized two highly stable Cu(II)-alkylperoxo systems at ambient conditions. The deformylation of 2-PPA was monitored using Cu(II)-alkylperoxo complexes as the catalysts. We have found that the Cu(II)-alkylperoxo complexes react with 2-PPA via an α-H abstraction mechanism

similar to the earlier reported Mn(III)-peroxo system. We also found out that the increasing bulk in the ligand architecture makes the deformylation slower.

The deformylation reactivity of 2-PPA and CCA is also studied using Fe(III)-N4Py peroxo intermediate. This study suggests that for Fe(III)-peroxo, the old conventional mechanism is applicable along with the possibility of a new H-atom abstraction approach. According to the results, the mechanism is different for both substrates. For Fe(III)-peroxo intermediates, details mechanistic investigation is yet to be needed to find out more about the ligand architecture effect.

Earlier studies from our lab show a possibility of aldehyde's H atom abstraction in CCA by Fe(III) peroxo intermediates. Still, the reaction mechanism was not very clear. We decided to check the reactivity of a tetradentate Mn(III)-peroxo complex with CCA in detail. We have studied the deformylation of CCA by two tetradentate Mn(III)-peroxo systems. We have found an enormous rate difference for deformylation between CCA and 1-D-CCA for both intermediates. This result indicates a C-H bond dissociation in RDS contrary to the previously reported nucleophilic carbonyl attack mechanism. It is independent of the ligand architecture around the metal center.

In summary, our study discovered a new mechanical way for the deformylation of 2-PPA by a Cu(II)-alkylperoxo complex and steric bulk's role on different electrophilic reactions. Aldehyde deformylation by Fe(III)-peroxo systems are known to proceed via a nucleophilic carbonyl attack mechanism. Our research

has observed that the reaction pathway for deformylation by Fe(III)-peroxo complex can differ depending on the substrates. We have also observed a new reactivity pattern and deformylation mechanism for the Mn(III)-peroxo complexes with substrates for which the mechanism was known otherwise. These results enlightened the vision about metal-peroxo reactivity with aldehydes with a different methodological viewpoint.

6.2 Future Possibilities

As discussed earlier, aldehyde's transformation to hydrocarbon in a single step by a biochemical process will help reduce greenhouse gases and be a very efficient conversion step in synthesizing larger molecules essential for pharmaceutical application. The information obtained from this research will help manipulate the catalyst's efficiency, selectivity, and substrate and product formation. The successful replacement for fossil fuel might not be possible at the moment on a large scale. Still, those catalysts can replace the use of fossil feedstock to generate other commodity products, and the findings from this research will lead to an essential step towards that direction. The mechanism of deformylation is still an enigma for the researcher. Although we have tried to establish the mechanism with a Cu, Mn, Fe-based system, there are still some loopholes in the mechanism part. A more precise understanding of the mechanism will help design the catalyst for efficacious biotransformation of aldehyde to hydrocarbon on an industrial scale.

List of publication

1. **Influence of induced steric on the switchover reactivity of mononuclear Cu(II)-alkylperoxo complexes**, *Inorg. Chim. Acta 2019, 485, 80.* **Sayanta Sekhar Nag**, Gourab Mukherjee, Prasenjit Barman, Chivukula V Sastri* https://doi.org/10.1016/j.ica.2018.09.087.

2. **Dramatic rate-enhancement of oxygen atom transfer by an iron(IV)-oxo species by equatorial ligand field perturbations**, Gourab Mukherjee, Calvin WZ Lee, **Sayanta Sekhar Nag**, Aligulu Alili, Fabián G Cantú Reinhard, Devesh Kumar*, Chivukula V Sastri*, Sam P de Visser*. *Dalton Trans., 2018, 47, 14945. https://doi.org/10.1039/C8DT02142B*

3. **Deformylation Reaction by a Nonheme Manganese(III)–Peroxo Complex via Initial Hydrogen-Atom Abstraction**, Prasenjit Barman, Pranav Upadhyay, Abayomi S. Faponle, Jitendra Kumar, **Sayanta Sekhar Nag**, Devesh Kumar*, Chivukula V. Sastri*, Sam P. de Visser*. *Angew. Chem. Int. Ed. 55, 2016, 11091. https://doi.org/10.1002/anie.201604412*.

Authors Introduction

Sayanta Sekhar Nag has found his interest in chemistry from Udang High School (H.S), where he spent his school days. He has completed his graduation from Bagnan College. His chemistry laboratory enthusiasm developed during the college days, and the interest received a high wind from the excellent instructors. In 2011 after qualified for JAM (Joint Admission Test for M.Sc.), he joined the Indian Institute of Technology Guwahati for his masters. In this period, he has come across several great teachers and developed a knack for research. In 2013 he qualified for JRF-NET (National Eligibility Test), and later in 2014, he joined the CVS group to fulfill the aspiration of research on bioinorganic chemistry.